Thin-Walled Composite Deployable Booms with Tape-Spring Hinges

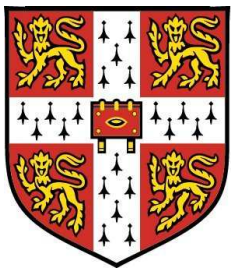

Harankahathanne Mallikarachchilage Yasitha Chinthaka MALLIKARACHCHI

Department of Engineering

University of Cambridge

Dissertation submitted for the degree of

Doctor of Philosophy

Wolfson College

May 2011

Acknowledgements

First and foremost, I extend my special thanks to my supervisor Prof Sergio Pellegrino for his advice, guidance and encouragement throughout the research. This deep appreciation also goes out to him for providing more than adequate facilities and resources both at the Deployable Structures Laboratory (DSL), Cambridge and the Space Structures Laboratory (SSL), Caltech. I am also grateful to Dr. Michael Sutcliffe for his advice during the course of this research and my college tutor Dr. Christina Skott for her help with all administration related issues.

I would like to thank Dr. Arul Britto for his help with finite element simulations and Prof. Guruswami Ravichandran and Prof. Chiara Daraio for allowing to use their laboratory facilities at Caltech. I am grateful to John Ellis (Hexcel Composites, UK) for providing materials for my research.

I am thankful to Roger Denston, Peter Knott, Len Howlett, Paul Bayford and Paul Long at Cambridge and Petros Arakelian and John Van Deusen at Caltech for their technical expertise. To Drs. Alessandro Spadoni, Laurence Bodelot and Jinkyu Yang for their help with experiments.

I would also like to thank all my colleagues both at DSL and SSL with whom I have had many interesting and helpful conversations. In particular I would like to thank Ahmad Kueh, Markus Pagitz, Quan Long, Tobias Gerngross, Peter Winslow and Xiaowei Deng.

The financial support of the Cambridge Commonwealth Trust and California Institute of Technology is greatly appreciated and it is their generosity that made this dissertation possible.

Last but not least, I would like to express my earnest gratitude to my parents for their moral support, and two brothers for always believing in me.

Declaration

The author declares that, except for commonly understood and accepted ideas, or where specific reference is made to the work of other authors, the contents of this dissertation are his own work and contain nothing that is the outcome of work done in collaboration. This dissertation contains nothing that has previously been submitted for any degree, diploma or other qualification. This dissertation is presented in 181 pages, and contains 103 figures, 31 tables and approximately 33,000 words, including the references and appendices.

H.M.Yasitha Chinthaka Mallikarachchi

Abstract

Deployable structures made from ultra-thin composite materials can be folded elastically and are able to self-deploy by releasing the stored strain energy. Their lightness, low cost due to smaller number of components, and friction insensitive behaviour are key attractions for space applications.

This dissertation presents a design methodology for lightweight composite booms with multiple tape-spring hinges. The whole process of folding and deployment of the tape-spring hinges under both quasi-static and dynamic loading has been captured in detail through finite element simulations, starting from a micro-mechanical model of the laminate based on the measured geometry and elastic properties of the woven tows. A stress-resultant based six-dimensional failure criterion has been developed for checking if the structure would be damaged.

A detailed study of the quasi-static folding and deployment of a tape-spring hinge made from a two-ply plain-weave laminate of carbon-fibre reinforced plastic has been carried out. A particular version of this hinge was constructed and its moment-rotation profile during quasi-static deployment was measured. Folding and deployment simulations of the tape-spring hinge were carried out with the commercial finite element package Abaqus/Explicit, starting from the as-built, unstrained structure. The folding simulation includes the effects of pinching the hinge in the middle to reduce the peak moment required to fold it. The deployment simulation fully captures both the steady-state moment part of the deployment and the final snap back to the deployed configuration. An alternative simulation without pinching the hinge provides an estimate of the maximum moment that could be carried by the hinge during operation. This moment is about double the snap-back moment for the particular hinge design that was considered.

The dynamic deployment of a tape-spring hinge boom has been studied both experimentally and by means of detailed finite-element simulations. It has been shown that the deployment of the boom can be divided into three phases: deployment; latching, which may involves buckling of the tape springs and large rotations of the boom; and vibration of the boom in the latched configuration. The second phase is the most critical as the boom can fold backwards and hence interfere with other spacecraft components.

A geometric optimisation study was carried out by parameterising the slot geometry in terms of slot length, width and end circle diameter. The stress-resultant

based failure criterion was then used to analyse the safety of the structure. The optimisation study was focused on finding a hinge design that can be folded 180° with the shortest possible slot length. Simulations have shown that the strains can be significantly reduced by allowing the end cross-sections to deform freely. Based on the simulations a failure-critical design and a failure-safe design were selected and experimentally verified. The failure-safe optimised design is six times stiffer in torsion, twice stiffer axially and stores two and a half times more strain energy than the previously considered design.

Finally, an example of designing a 1 m long self-deployable boom that could be folded around a spacecraft has been presented. The safety of this two-hinge boom has been evaluated during both stowage and dynamic deployment. A safe design that latches without any overshoot was selected and validated by a dynamic deployment experiment.

Keywords: thin woven CFRP, micro-mechanical modelling, composite failure, tape springs, self-deployable structures, deployment dynamics, design optimisation.

Contents

List of Figures

List of Tables

List of Symbols

Roman Symbols

A	cross-sectional area, mm^2
a	maximum tow thickness, mm
A_{ij}	coefficients of upper-left 3×3 submatrix of ABD, N/mm
ABD	constitutive matrix in coordinate system x and y
a_{ij}	coefficients of in-plane compliance matrix, mm/N
b	width, mm
B_{ij}	coefficients of upper-right 3×3 submatrix of ABD, N
D_{ij}	coefficients of lower-right 3×3 submatrix of ABD, N·mm
c_d	dilatational wave speed, mm/s
c_v	viscous pressure coefficient, Ns/mm^3
D	diameter of the end circles of the slot, mm
E	elastic modulus, N/mm^2
E_b	energy balance, mJ
E_i	internal energy, mJ
EI	bending stiffness of the plate, Nmm^2
E_k	kinetic energy, mJ
E_v	viscous dissipation, mJ
E_w	work done by external forces, mJ
F_i	uniaxial failure strengths in tow directions (x and y)

$\hat{f}_i$	linear failure coefficient, components of 6×1 vector
$\hat{f}_{ij}$	quadratic failure coefficient, components of 6×6 symmetric matrix
f_i, f_{ij}	second- and fourth-order strength tensors
G	shear modulus, N/mm^2
h	thickness of shell elements, mm
L	slot length, mm
l	characteristic length of finite element mesh, mm
l_{min}	shortest length of finite element , mm
M	moment per unit length stress resultant, N
m	distributed moment due to bulk viscosity, N/mm
N	force per unit length stress resultant, N/mm
n	number of specimens
$\boldsymbol{n}$	unit surface normal
P	force, N
p	viscous pressure, N/mm^2
p_b	bulk viscosity pressure, N/mm^2
R	transverse radius of the tape-spring cross-section, mm
r	radius of curvature of curvature of the elastic fold of bent tape spring, mm
R^u	failure radius, mm
s	$1/6^{\text{th}}$ of span between bottom supports of four-point bending rig, mm
SW	slot width, mm
U	global translation components of tape-spring hinge model, mm
u, v, w	translations in x, y, z directions, mm
$\boldsymbol{v}$	velocity vector, mm/s
V	volume fraction

W	areal weight, g/m^2
x_i	measured or derived property
X, Y, Z	global coordinate system of tape-spring hinge model
x, y, z	material coordinate system (tow directions)
x', y', z	coordinate system for loading directions

Greek Symbols

α	time scaling factor
β	mass scaling factor
δ	maximum relative deflection, mm
ε	mid-plane strain, mm/mm
ϵ	strain, mm/mm
$\dot{\epsilon_v}$	volumetric strain rate, 1/s
γ	engineering shear strain, mm/mm
κ	curvature, 1/mm
$\dot{\kappa}$	twice the mean curvature rate, 1/mm·s
ν	Poisson′s ratio
ϕ	angle between tow directions (x and y) and loading directions (x' and y'), degrees
ψ	folding angle of tape-spring hinge, degrees
ρ	density, kg/m^3
$\hat{\sigma}_i$	N_x, N_y, N_{xy} for $i = 1, 2, 3$ and M_x, M_y, M_{xy} for $i = 4, 5, 6$
σ	direct stress, N/mm^2
τ	shear stress, N/mm^2
θ	rotation, radian
ξ	fraction of critical damping in highest frequency mode

Superscripts

± 45	± 45 laminate
0/90	0/90 laminate
u	ultimate strength

Subscripts

c	compression
$comp$	composite
$core$	foam core
f	fibre
m	matrix
s	shear
t	tension

Other Symbols

$(\ldots)', \ldots$	quantity that refers to loading directions x' and y'
CV	sample coefficient of variation, %
ΔL	weave length of fabric, mm
Δt	stable time increment, s
s_{n-1}	sample standard deviation
$\bar{x}$	sample average
$(\ldots)_x, \ldots$	components in direction x, etc.
$(\ldots)^x, \ldots$	deformation directions for unit cell

Acronyms

ASTM	American Society for Testing and Materials
CFRP	Carbon Fibre Reinforced Polymer
CLT	Classical Laminate Theory
FFT	Flattenable Foldable Tubes
FI	Failure Index

FITS	Fold Integrated Thin-film Stiffener
FLATS	Folding Large Antenna Tape Spring
IFH	Integral Folding Hinge
ISAT	Innovative Space-Based Radar Antenna Technology program
MARSIS	Mars Advanced Radar for Subsurface and Ionosphere Sounding
MSAT	Mobile SAtellite System
PTFE	Poly Tetra Fluoro Ethylene
RUC	Representative Unit Cell
SAR	Synthetic Aperture Radar
STEM	Storable Tubular Extendible Member
TDRS	Tracking and Data Relay Satellite

Chapter 1

Introduction

1.1 Overview

The design of large space structures, such as solar sails, solar concentrators and reflector antennas, is limited by the pay load and stowage capacity of launch vehicles. However, most space structures have much larger dimensions than the launchers and the concept of deployable structures allows a large structure to pack into a compact configuration for stowage and transportation and then expand back to the operational configuration. Commonly used deployable schemes include inflatables, mechanically jointed and motorised structures, stored energy deployable structures and structures made of shape-memory alloys.

Deployable structures made from ultra-thin composite materials can be folded elastically and are able to self-deploy by releasing the stored strain energy. They are becoming more widespread because of their lower mass to deployed stiffness ratio, good packaging properties, lower cost due to a smaller number of component parts and ease of manufacture (Warren, 2002). Examples of structures of this kind that have been already flown include the Boeing springback reflectors on the Mobile SAtellite System (MSAT)[1] (Anonymous, 1994; Seizt, 1994) and on the Tracking and Data Relay Satellite (TDRS) H, I, J[2]. Also the three Northrop Grumman Astro Aerospace Flattenable Foldable Tubes (FFT) forming the Mars Advanced Radar for Subsurface and Ionosphere Sounding (MARSIS) antenna on the Mars Express spacecraft (Adams and Mobrem, 2009).

[1] http://www.boeing.com/defense-space/space/bss/factsheets/601/msat/msat.html
[2] http://www.boeing.com/defense-space/space/bss/factsheets/601/tdrs_hij/tdrs_hij.html

1.2 Recent Developments

Structures based on this approach have already been used in a few missions and a range of novel structural architectures that exploit this approach in future missions has been proposed.

MARSIS was the first antenna of its kind, designed to look below the surface of Mars at the different layers of material, and most notably to look for water. The antenna consisted of two 20 m dipoles and a 7 m monopole. All three booms were slotted at certain intervals to stow them in a 1.7 m × 0.3 m × 0.2 m cradle as shown in Figure 1.1b.

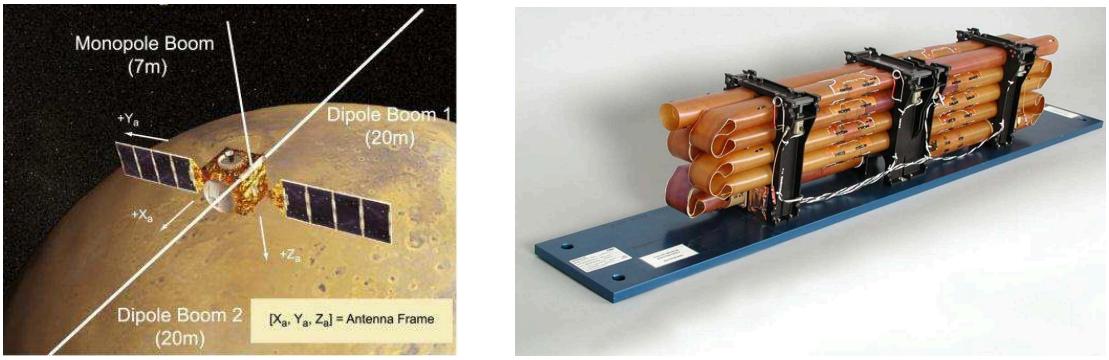

(a) In orbit (b) Stowed

Figure 1.1: MARSIS booms (courtesy: Astro Aerospace).

Novel reflector antenna concepts based on the same general approach have been proposed, including the "hollow solid" reflector structure (Soykasap et al., 2004), the Fold Integrated Thin-film Stiffener (FITS) solar array, which undergoes three different folding stages to achieve a highly compacted configuration (Jorgensen et al., 2005), and the Folding Large Antenna Tape Spring (FLATS) radar concept (Soykasap et al., 2008).

The "hollow solid" deployable reflector concept for low-cost L-band Synthetic Aperture Radar (SAR) uses thin curved carbon fibre reinforced polymer (CFRP) sheets connected by flexible hinges to form a parabolic reflector surface with high accuracy, Figure 1.2.

The FLATS concept by Soykasap et al. (2008), targets a low-mass 50 m^2 deployable antenna that measures the biomass content of forests from a low-Earth orbit. It consists of two Kevlar sheets connected by a compliant Kevlar core that allows the whole structure to be folded elastically and to self-deploy into the original

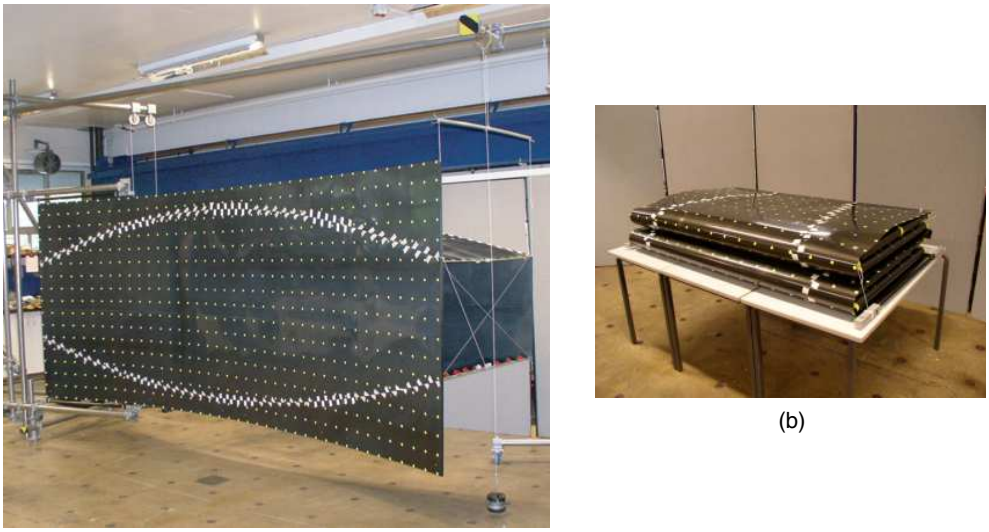

(a) (b)

Figure 1.2: Hollow solid reflector (Soykasap et al., 2004) (a) deployed and (b) folded.

configuration, Figure 1.3.

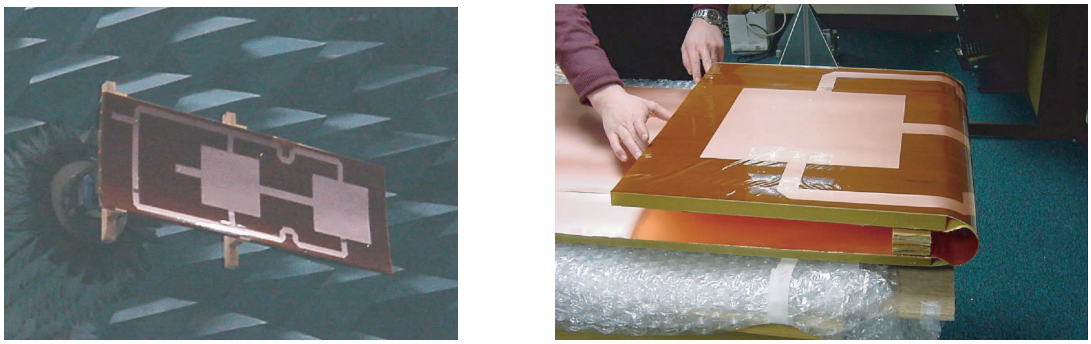

(a) Deployed configuration (b) Folding

Figure 1.3: Folding Large Antenna Tape Spring (Soykasap et al., 2008).

Further examples of technology developments for future missions are RUAG's self-motorised deployment mechanism (Boesch et al., 2008), DLR's lightweight deployable booms (Block et al., 2011; Sickinger et al., 2004) and Phased-Array-Fed Reflector for the Innovative Space-Based Radar Antenna Technology (ISAT) program (Lane et al., 2011). Figure 1.4 shows four lightweight composite booms that deploy a 20 m by 20 m solar sail array.

The deployment schemes that have been considered so far envisage the release of all constraints on the structure, to allow the structure to dynamically deploy and

(a) Snapshots during deployment (b) Booms deploy a solar sail

Figure 1.4: Lightweight deployable booms (courtesy: DLR).

self-latch. However this behaviour needs to be fully understood and optimised as severe dynamic effects at the end of deployment could damage the structure and yet a slow, highly damped deployment may end without ever achieving the fully deployed configuration. Achieving a balance between these effects is challenging, as demonstrated by the large amount of testing and simulation that was required to achieve the successful deployment of the MARSIS booms (Adams and Mobrem, 2009).

1.3 Scope and Aims

The broad aim of this research is to develop simulation techniques to predict both quasi-static and dynamic behaviour of stowed energy deployable structures made of fibre composites. These design tools will lead to a better understanding of their complex behaviour and hence will allow the design of more efficient structures.

A simple boom construction based on a thin-walled tube made of two plies of plain-weave carbon fibre in an epoxy matrix is considered here. Certain regions of the tube are weakened by cutting away some of the composite material to form tape-spring hinges at which can be folded without causing any damage, Figure 1.5. A variant of this hinge design, with three slots, was analysed with the implicit finite element code ABAQUS/Standard by Yee and Pellegrino (2005a) and Soykasap (2009). Also each folding section of the MARSIS booms (Mobrem and Adams, 2009) is in fact a tape-spring hinge with two slots.

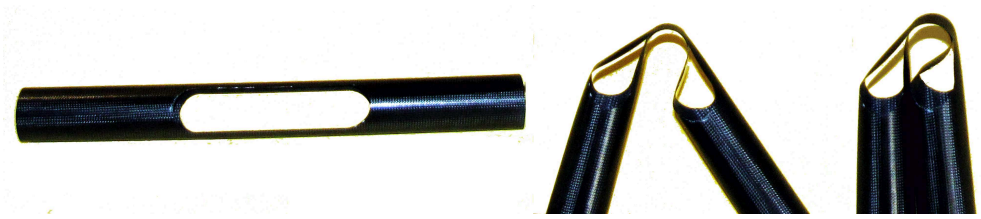

Figure 1.5: Photos of a tape-spring hinge deployed, partially folded and fully folded.

Thin laminates made of woven tows of carbon fibre are not accurately modelled by Classical Lamination Theory (CLT) (Soykasap, 2006; Yee and Pellegrino, 2005b). A more accurate model is a linear-elastic thin Kirchhoff plate whose properties are defined by a homogenisation technique based on the geometric properties of the laminate measured from micrographs, with the tow properties calculated from appropriate rules of mixtures.

A repeating unit cell modelled with periodic boundary condition is used to obtained the properties of the laminate in the form of an ABD stiffness matrix that is experimentally validated. This ABD stiffness matrix is used to define the stiffness properties of the tape-spring hinge finite element model.

Both quasi-static folding and deployment, as well as the dynamic deployment behaviour of a tape-spring hinge is studied first by simulations carried out with the commercial finite element package Abaqus/Explicit (Abaqus, 2010). The safety margin of the structure both during folding and dynamic deployment is evaluated with a six dimensional stress-resultant based failure criterion.

A parametric study of a general hinge geometry defined by three parameters is carried out, to obtain improved designs. These improved designs are then used to arrive at a specific design for a 1 m long tubular boom that can be wrapped around a spacecraft and is able to self-deploy without any damage.

The final design of this boom is then verified by experiments.

The design tools developed in this research can be used to design deployable booms with multiple hinges and optimised boom geometry, to meet any specific mission requirements. However a specific boom diameter and two-ply laminate are selected for demonstration.

1.4 Chapter Organisation

This thesis comprises 11 chapters. After the present introductory chapter, Chapter 2 begins with a brief review of the development of stored energy deployable structures. The first part of the chapter describes tape-spring hinge designs used in the space industry followed by larger deployable structures based on similar structural concepts. The second part of the chapter revises the available techniques to model woven carbon fibre composites and different failure criteria.

Chapter 3 describes the manufacturing process used to construct composite booms and other test specimens. The construction of a tube made of two-ply carbon fibre laminate is explained first. The alterations to this procedure in constructing a flat or curved specimen is explained next and finally the fabrication procedure for a tape-spring hinge is described.

Chapter 4 studies the constituent properties of the laminates. The fibre and matrix properties are obtained from corresponding manufactures and a weight based approach is used to calculate the fibre volume fraction. The geometric properties of a tow are obtained from micrographs of the tow cross-section. Finally, the laminate properties are measured with a series of stiffness and strength characterisation experiments.

Chapter 5 considers a repetitive unit cell and carried out an analysis of a micro-mechanical model to determine the homogenised stiffness properties of the unit cell. The geometric and stiffness properties of the tows obtained in Chapter 4 are used to construct a finite element model of the unit cell, subject to periodic boundary conditions. Using virtual work the material stiffness is expanded in the form of an ABD stiffness matrix. Suitable definition for the tow cross-section shape and waviness are obtained through a series of sensitivity studies. Two extreme ply arrangements are also considered. The possibility of using a micro-mechanical failure criterion is then investigated.

Chapter 6 presents a stress-resultant based, six dimensional failure criterion for symmetric two-ply plain weave carbon fibre composites. Five uni-axial strength tests are used to construct the failure locus and five additional combined tests are performed to verify the accuracy of the criterion. The chapter concludes with a discussion on the limitations and assumptions used in constructing the criterion.

Chapter 7 describes the simulation techniques developed for both quasi-static and dynamic deployment predictions. A brief introduction to the available features,

simulation parameters and necessary checks is presented first. The sensitivity of the simulation to various parameters is investigated for both quasi-static and dynamic simulations.

Chapter 8 analyses both quasi-static and dynamic deployment behaviour of the hinge simulated in Chapter 7. The hinge behaviour is characterised by the moment-rotation response during quasi-static folding and deployment, and by the angle-time variation during dynamic deployment. The sensitivity of the results to different boundary conditions is investigated using infinite elements.

Chapter 9 explains the design optimisation procedure followed to obtain improved hinge designs. A general hinge geometry is defined with three parameters and several selected design are analysed with the design tools presented in Chapter 7. Use of these hinge designs in a 1 m long foldable boom with two hinges is then investigated.

Chapter 10 performs an experimental validation of the final design of the boom. The safety of both failure critical and failure safe designs of the boom is investigated and the predicted failure locations are verified. Both quasi-static and dynamic deployment behaviour of a selected hinge design are compared to experimental results. Finally the dynamic deployment behaviour of a two-hinge boom is verified.

Chapter 11 presents a summary of the design tools developed during this research, followed by a set of conclusions. Finally, some suggested future research directions are presented.

Chapter 2

Literature Review

This chapter presents an overview of the literature on stored energy deployable structures and the analysis of woven composites. The chapter begins with an introduction to various stored energy deployable structures and explains previously developed hinge designs that use tape-springs. Next a review of larger structures that extend the tape-spring concept to store the elastic strain energy by deforming the entire structure is presented. The second part of the chapter describes various models used for stiffness characterisation of woven composites and concludes with commonly used criteria for failure analysis.

2.1 Stored Energy Deployable Structures

Stored energy deployable structures have been among the leading candidates for space structures from the dawn of space exploration. These structures are designed to fold elastically and self-deploy by releasing the energy stored within the structure. Their capability of self-deploying to the original configuration without permanent deformation is a key attraction.

2.1.1 Tape Spring Hinges

The simplest stored-energy deployable structure is the tape spring, of which an example is the steel tape measure (also known as carpenter tape). They are increasingly being used as a replacement of more traditional hinge mechanisms due to their high repeatability and pointing accuracy. Unlike traditional hinge mechanisms, tape-springs do not include moving parts that can become jammed due to

long-term stowage or adverse environmental conditions.

There has been an extensive amount of research into the behaviour of metal tape springs (Seffen and Pellegrino, 1999; Szyszkowski et al., 1997; Watt, 2003). However the present trend is to use fibre reinforced polymers due to their lighter weight and the possibility of altering their properties by using different fibre arrangements and composition.

Seffen and Pellegrino (1999) show that the behaviour of a tape-spring can be characterised by the moment rotation relationship, see Figure 2.1, where the origin of the $M(\theta)$ curve is denoted as O. The behaviour is highly dependent on the sign of the moment, Figure 2.2. When a positive moment is applied, i.e. a moment that induces tensile stresses along the edges of the tape spring, first the tape-spring shows a linear behaviour from O to A, as the tape bends into a smooth curve. At A the tape suddenly snaps and becomes approximately straight in two pieces separated by a localised bend. From B to C the arc length of the localised bend increases with constant moment. During the unfolding process the tape-spring follows the path from C to D and suddenly snaps to E. However with a negative moment, i.e. a moment that induces compressive stresses along the edges of the tape spring, the linear behaviour ends much sooner and a sudden bifurcation occurs at F which corresponds to a flexural torsional deformation. In this case unfolding follows almost the same path.

Mansfield (1973) through an analytical study has shown that tape-spring like structures are subjected to snap-through flexural buckling or buckling into a torsional mode, depending on the magnitude of the transverse curvatures of the structure.

The behaviour of composite tape-springs is similar to that described above. Yee and Pellegrino (2005a) show that the relationship between the transverse radius of the tape-spring cross-section, R, and the longitudinal radius of curvature of curvature of the elastic fold, r is equal to the square root of the ratios between D_{11} and D_{22} for a tape-spring made with a balanced and symmetric laminate. For an isotropic tape spring, $r = R$ (Calladine, 1988).

The use of tape-springs in hinges for deployable structures dates back to the 1960's. Vyvyan (1968) showed that the bending stiffness in the deployed configuration and the moment required to buckle a hinge are both improved by arranging the tape-springs in an offset configuration as shown in Figure 2.3. In the deployed configuration short tape-springs exhibit significant stiffness and buckling resistance

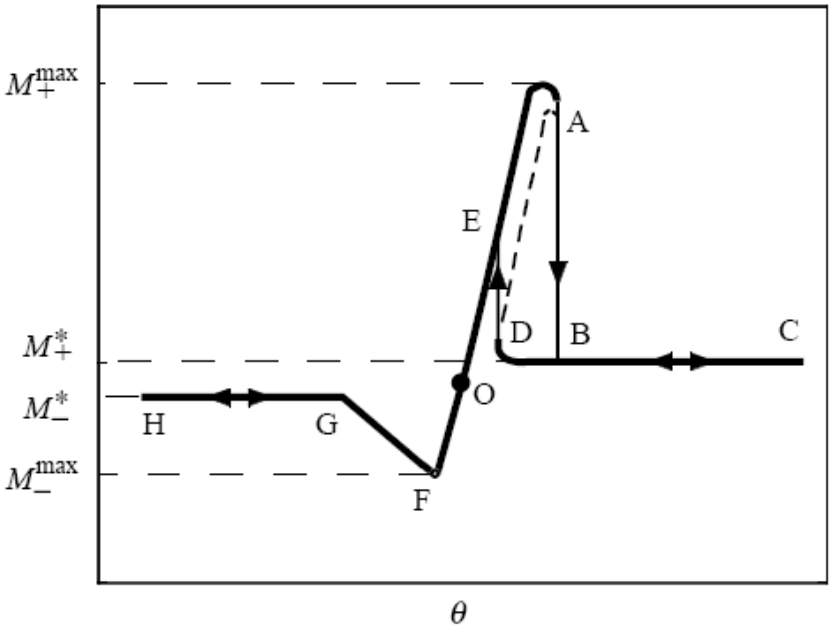

Figure 2.1: Typical moment-rotation relationship of a tape-spring (Seffen and Pellegrino, 1999)

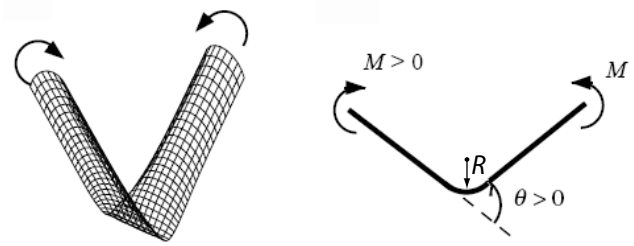

(a) Opposite-sense

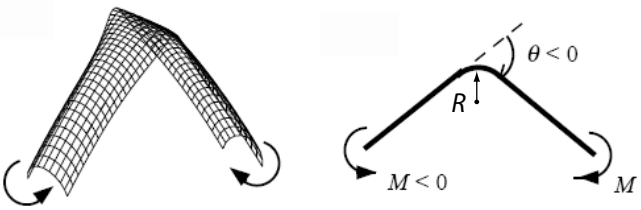

(b) Equal-sense

Figure 2.2: Sense of bending of tape-springs.

because they are subjected mainly to axial tension and compression. Once the tape-springs are buckled, this resistance becomes significantly lower because they are loaded in bending. Also, the offset tape-spring arrangement provides a higher torsional resistance.

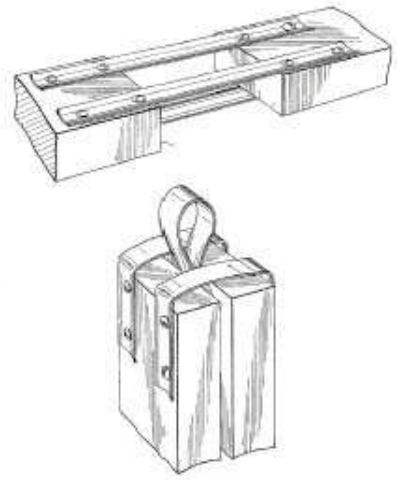

Figure 2.3: Hinge layout described by Vyvyan (1968) in deployed and folded configurations.

Chiappetta et al. (1993) proposed a more compact geometry, but with an increased deployment moment by arranging the tape-springs in a symmetric configuration as shown in Figure 2.4a. Two tape-springs come into contact with each other on folding and hence store a higher amount of strain energy. They also describe the possibility of using CFRP laminates instead of the more standard spring steel or beryllium copper. Figure 2.4b shows their proposal for using these tape-spring hinges in an array antenna.

A self-motorised deployment mechanism introduced by Boesch et al. (2008) incorporates four pairs of CFRP tape-springs in a row, each with the concave side facing inwards, Figure 2.5. Thus the tapes in each pair are bent one in the equal sense, i.e. with the longitudinal curvature in the same sense as the transverse curvature of the tape, and one in the opposite sense; this configuration loads to a high latching moment and hence to a highly repeatable deployed configuration. However, depending on the amount of strain energy stored in the folded hinge and the maximum moment that it can carry without beginning to fold, the hinge may fail to properly latch the first time that it reaches the fully deployed configuration and,

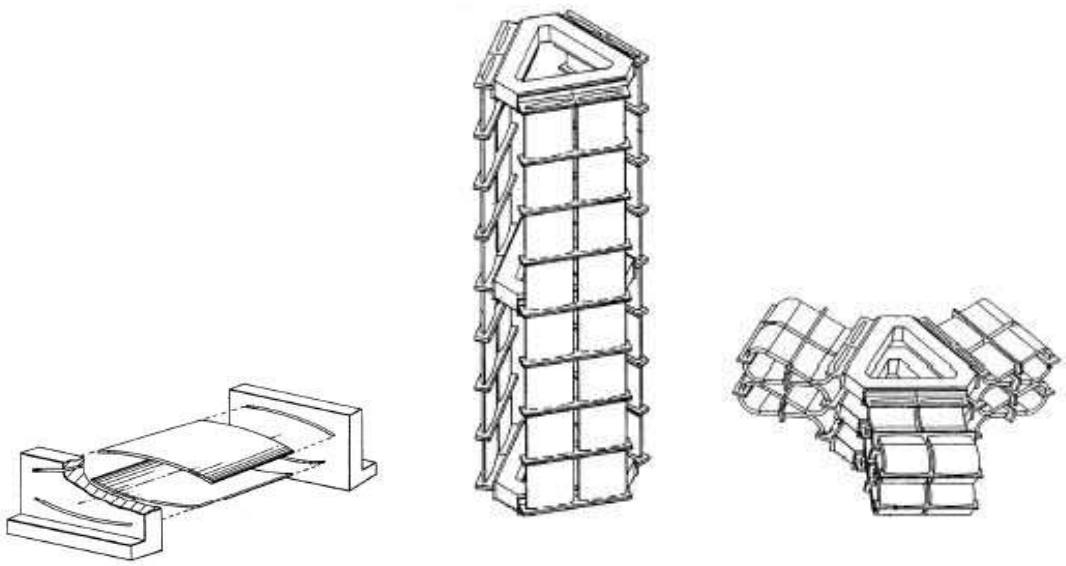

(a) Hinge layout (b) Deployed and stowed configuration of the boom

Figure 2.4: Tape-spring hinge and its application by Chiappetta et al. (1993).

due to an excessive amount of kinetic energy, it may continue through the deployed configuration and start folding in the opposite sense the tape-spring that was originally bent in the equal sense. This process involves buckling of this tape-spring and may cause permanent damage.

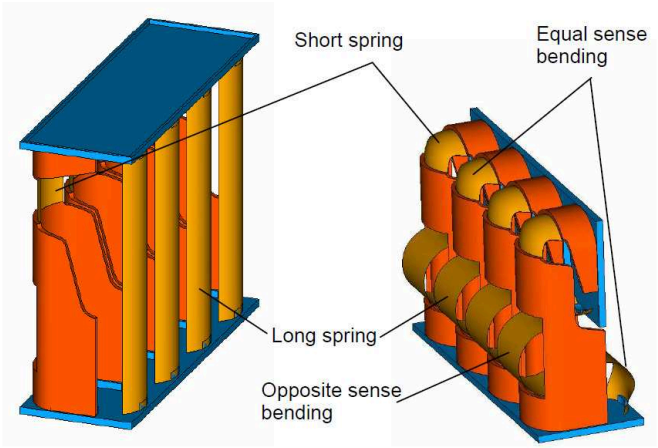

Figure 2.5: Self-motorised deployment mechanism by Boesch et al. (2008)

Various other designs that use tape-springs were proposed by Fang and Lou (1999); Keller et al. (2004); Seffen (2001); Silver and Warren (2010); Warren et al.

(2005); Watt (2003), etc.

2.1.2 Monolithic Structures

Recent developments for future space missions have extended the tape-spring concept to larger structures where the entire structure is made of combinations of large tape-spring like portions. Here not only the folding lines but the entire structure is subjected to elastic deformation.

In fact, this concept goes back to the 1960's when the Storable Tubular Extendible Member (STEM) was invented in Canada (Rimrott and Fritsche, 2000), Figure 2.6(a). The STEM is an extension of the principle used in the coilable, self-straightening steel tape measure; it consists of a thin-walled cylindrical shell with circular cross-section. It is flattened and rolled up onto a drum within a cassette for stowage. It is deployed by rotating the drum in the opposite direction. A STEM is quite stiff axially and in bending, but because of the open tubular section it has low torsional stiffness. The bi-STEM is a STEM where two identical cylindrical shells are placed one inside the other, Figure 2.6(b). A bi-STEM has higher bending stiffness and better mechanical damping behaviour. The interlocking STEM is a version of the bi-STEM, Figure 2.6(c) with a higher torsional stiffness.

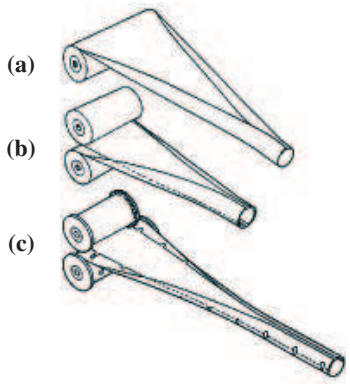

Figure 2.6: Storable Tubular Extendible Members. (a) STEM (b) bi-STEM (c) interlocking bi-STEM

Rubin (1969) uses a similar concept to construct an extendable boom made of joining two omega-shaped thin metal shells at the edges. The cross-section of this boom can be flattened and then rolled into a coiled configuration. DLR's ultralight CFRP deployable boom uses the same concept but with a composite

material. This boom consists of two edge-bonded omega-shaped carbon fibre open shells with 0.1 mm wall thickness, each with a weight of 62 g/m. Block et al. (2011) show that the boom deployment needs to be controlled as excessive strain energy leads to a chaotic deployment. They have used two different controlled deployment schemes. The first, method uses an inflatable polymer hose inside the boom and the other uses electromechanical uncoiling device.

Figure 2.7: Ultralight deployable CFRP boom (courtesy: DLR).

The FLATS proposed by Soykasap et al. (2008) consists of two 2.82 m by 8.64 m large panels. Each panel is built as a large tape spring made of two three-ply Kevlar sheets maintained at a distance of 40 mm gap by 7 longitudinal spacers. FLATS undergoes two folding stages, first the curved panels are flattened and then z-folded. During folding strain energy is stored in the Kevlar sheets. The longitudinal spacers have two main functions, first to maintain an accurate separation between the panels and second to limit the bending radius. Soykasap et al. (2008) show that four-ply Kevlar sheets would not recover their original shape after folding into a 30 mm bending radius.

The novel deployable reflector concept developed by Soykasap et al. (2004) is based on forming a collapsible hollow solid using four thin-walled CFRP sheets. The structure presented in this study packages to $1/16^{\text{th}}$ of its deployed volume and it is two-and-half times lighter than a traditional reflector structure made out of lightweight, curved panels with self-locking hinges.

The half-scale model in Figure 2.8 is made of T300/LMT45 laminate (0/45/0) with uniform thickness of 0.3 mm. The four sheets were connected by 3M 79 woven-glass tape and 3M Scotch-Weld DP490 epoxy resin. This structure undergoes two different folding stages. First it is flattened by folding the side walls and then into

an accordion, Figure 2.8. The minimum bending radius was set at 24 mm providing a margin of 2.3 on material failure.

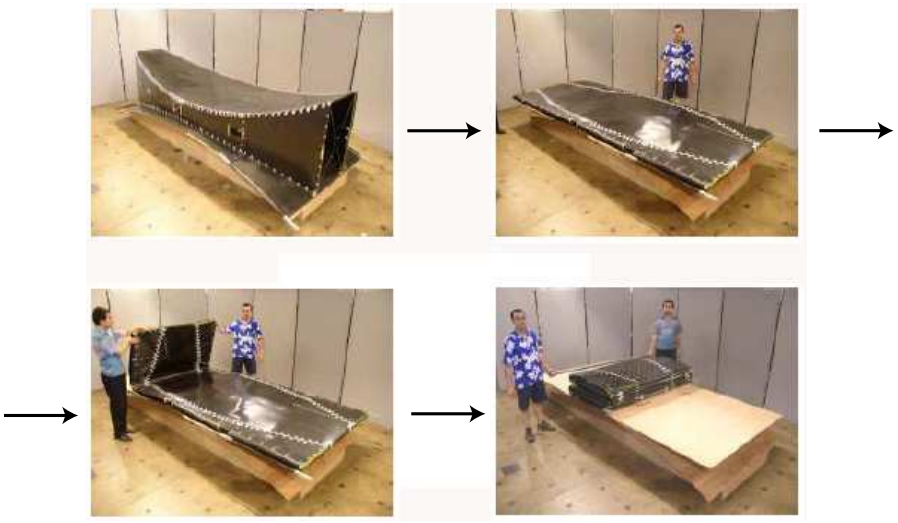

Figure 2.8: Folding sequence of the reflector (Soykasap et al., 2004).

Marks (2002) presents a foldable boom where tape-springs are formed by cutting two parallel longitudinal slots in a thin-walled tube as shown in Figure 2.9. As the tape-springs form part of the boom, the whole structure is simple to manufacture and its continuity leads to good stiffness and thermal properties. This design can be flattened elastically to minimise the stowed volume; in the proposed concept, flexible stiffeners can be added to provide additional torsional stiffness. Warren (2002) described a similar approach but with different slot geometries and arrangements to construct collapsible trusses.

The FFT developed by Astro Aerospace which constructed the MARSIS antenna is an application of the design presented by Marks (2002). The MARSIS antenna is made of thin walled S-Glass and Kevlar composite. The antenna is manufactured into three parts as two 20 m long dipoles and a 7 m long monopole, consisting of composite tubes with diameters of 38 mm and 20 mm respectively (Marks et al., 2002). These tubes are slotted at certain intervals (1.53 m for the dipoles and 1.3 m for the monopole) to facilitate folding into a cradle, Figure 2.10. In addition to folding, these tubes are compressed to partially flatten them down to half of their diameter (19 mm for the dipoles and 10 mm for the monopole), to achieve a more compact configuration together with higher elastic energy within the system.

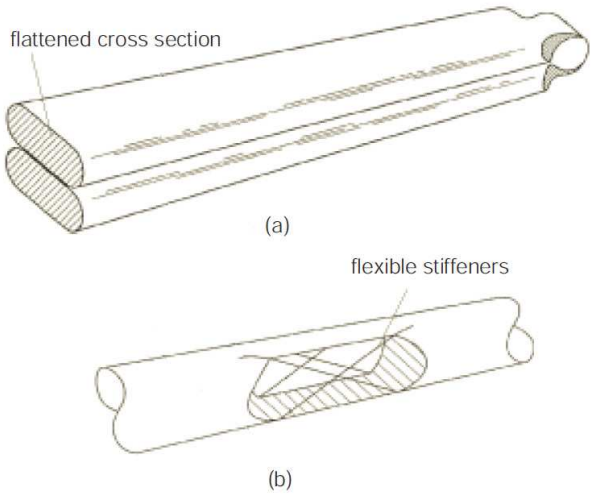

Figure 2.9: Fattenable foldable boom hinge (Marks, 2002).

However the dipole hinges have a very low deployment moment, 0.2 Nm, and hence any significant friction or air drag that would occur on Earth would prevent its deployment. This, together with its large dimensions, make it impractical to deploy it in any ground test facilities. Thus this structure was qualified for launching relying solely on simulations and component testing.

(a) Hinge

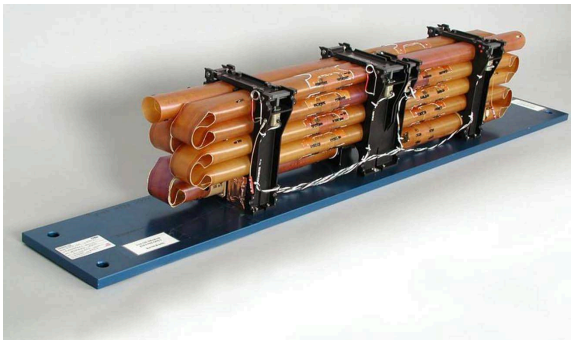

(b) Stowed configuration

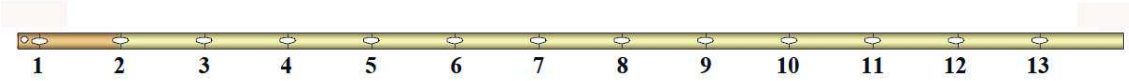

(c) Complete boom

Figure 2.10: Flattenable foldable tube (courtesy: Astro Aerospace).

Mobrem and Adams (2009) stated that the structural behaviour of these joints

is complex and needs to be properly understood. It is important to optimise the total stowed energy within the system to control the dynamics of deployment while ensuring that the structure will self-deploy.

Silver et al. (2004) carried out controlled displacement snap-through studies of tape-springs which constitute the Integral Folding Hinge (IFH), with the aim of deriving design guidelines for axial loading. Further investigation of the bending-induced buckling response of an individual IFH was presented later (Silver et al., 2005). Figure 2.11 shows a support structure constructed from IFH.

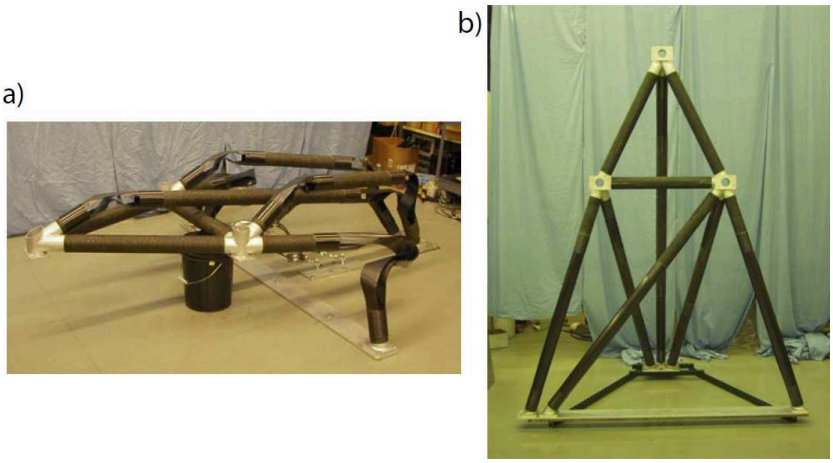

Figure 2.11: Support structure concept based on Integral Folding Hinge (Silver et al., 2005) (a) stowed and (b) deployed.

Yee (2006) studied the dynamic deployment behaviour and repeatability of a CFRP boom made by cutting three parallel slots in a thin-walled tube, Figure 2.12. He conducted a series of experiments on approximately 1 m long boom with a single point off-load system and showed that the dynamic deployment behaviour of the boom can be divided into three phases, namely, deployment, large displacement vibration (low frequency) and final vibration (high frequency), Figure 2.13. He found that the hinge is unable to resist the angular momentum of the boom at the point of latching, hence the boom overshoots the fully deployed configuration.

Soykasap (2009) used a simplified approach to characterise the angle-time variation of Yee's experiments. He followed a semi-analytical approach to predict the dynamic deployment behaviour of the boom. The moment rotation profile of a boom hinge was obtained from nonlinear finite element analysis and dynamic deployment simulation of the boom were then carried out analytically.

Figure 2.12: Three-slot CFRP tube hinge (Yee, 2006).

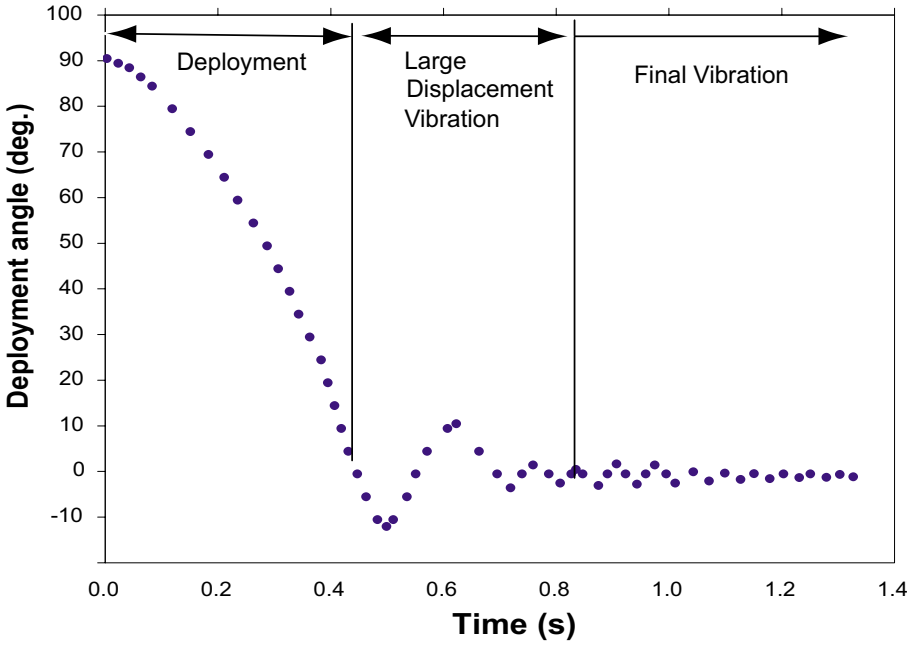

Figure 2.13: Angle-time response of three-slot boom (Yee, 2006).

2.2 Woven Composite Materials

Fibre composites have gained increasing popularity over metal alloys due to their high strength to weight ratio and the wider range of design possibilities offered by tailorable material properties. Textile composites provide better performance in intra- and inter-laminar strength and damage tolerance over composites made from unidirectional lamina. They can be classified as woven fabrics, braided fabrics and knitted fabrics according to the arrangement and presentation of their reinforcing elements, (Cox and Flanagan, 1997).

The two basic constituents of textile composites are the tows, i.e. continuous strands of fibres and the matrix which keeps them together. There are two sets of interlacing tows acting as reinforcement. When the two sets of tows are interlaced at right angles, the longitudinal tows, in the machine direction, are known as warp, and the perpendicular tows as fill or weft. Figure 2.14 shows a schematic of the components of a woven fabric.

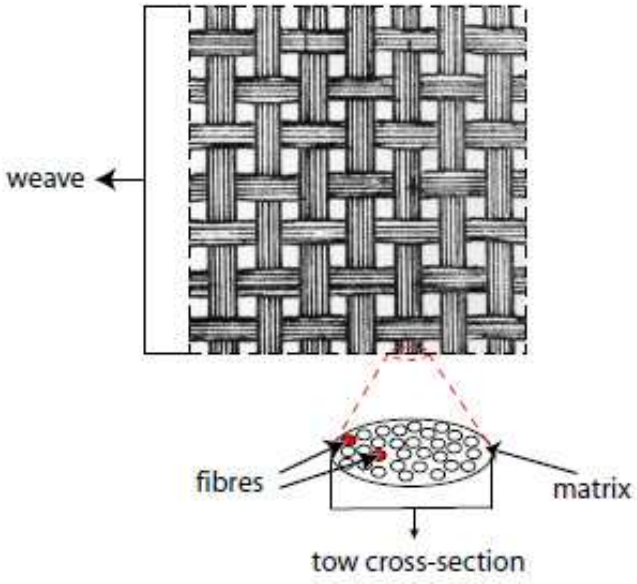

Figure 2.14: Schematic of a woven fabric composite.

The weave style controls the draping, surface smoothness and stability of the fabric. Figure 2.15 shows examples of orthogonal woven fabrics.

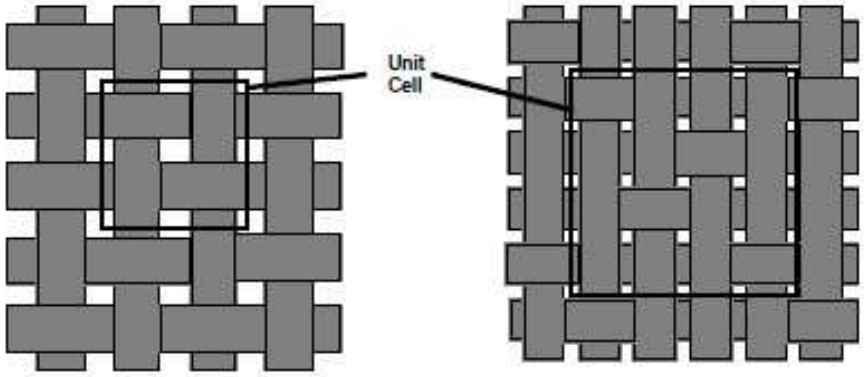

(a) Plain weave (b) Crows-foot satin weave

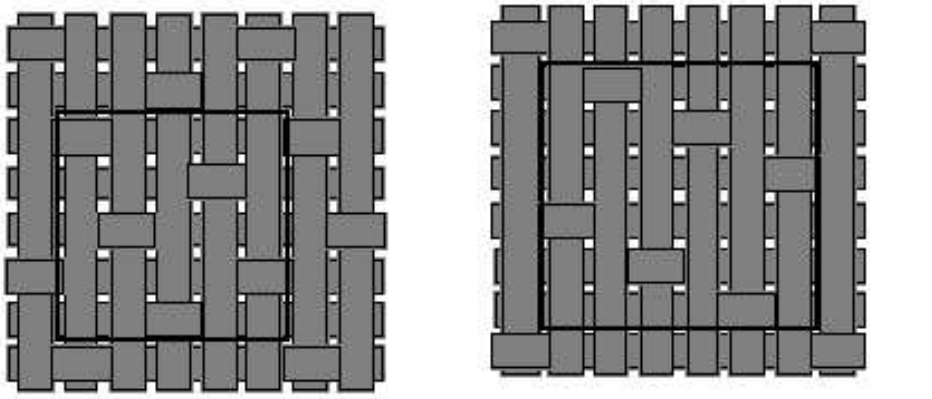

(c) Five-harness satin weave (d) Eight-Harness satin weave

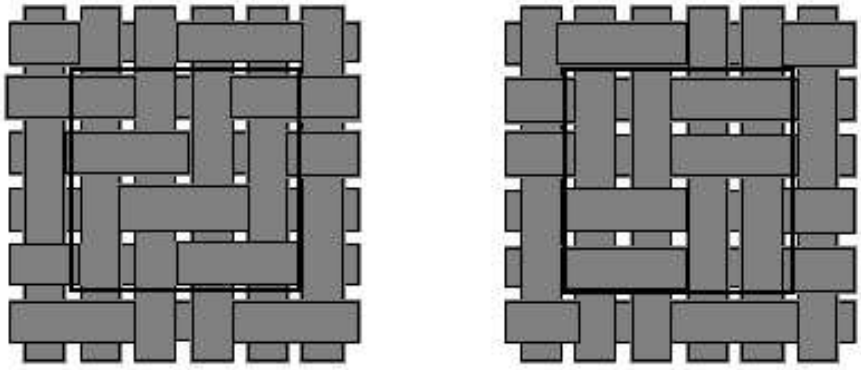

(e) 2×2 twill weave (f) 2×2 basket weave

Figure 2.15: Examples of biaxial woven fabrics (Cox and Flanagan, 1997).

2.2.1 Modelling Woven Composites

The mechanical behaviour of composite materials consisting of many unidirectional plies forming a laminate is well described in standard textbooks (Daniel and Ishai, 2006; Gibson, 2007; Jones, 1999; Tsai and Hahn, 1980). In general, the lamina properties are estimated using rule of mixtures and the laminate properties are calculated with the CLT.

However, in the case of textile composites it is difficult to use simple analytical models due to their complex architecture. Soykasap (2006) explained that even though the in-plane properties of woven composite materials can be estimated accurately using CLT, the corresponding bending properties lack any accuracy for one- or two-ply woven laminates. He showed that such estimates can result in errors of up to 200% in the maximum bending strains or stresses, and up to 400% in the bending stiffness.

Researchers have used finite element analysis to understand the behaviour of textile composites by modelling a representative unit cell (RUC). Depending on the scale of interest, the RUC can comprise parts of tow geometries that are repeated in building the entire textile geometry or at a smaller scale the repeated fibre pattern filled with matrix.

Early work on modelling woven fabrics has been carried out by Ishikawa and Chou (1982). They extended CLT to a woven fabric composite that has been idealised as pieces of cross-ply laminates consisting of groups of plates arranged in series or parallel, depending on the cross-ply laminate design. A constant stress or strain state was assumed respectively for the series and parallel cases. The model ignored the through thickness shear deformation, fibre continuity and the non-uniform stress and strain distributions in the interconnection regions. They showed that the parallel and the series models give upper and lower bound estimates of the in-plane extensional modulus, respectively. This is known as the mosaic model, Figure 2.16(a).

Extending their work to consider fibre undulation Ishikawa and Chou (1983a) introduced a 1D crimp model called the fibre undulation model, Figure 2.16(b). This model considered the fibre continuity and undulation in the loading direction, however the interlaced regions between the tows were not considered in either of these models. Ishikawa and Chou (1983b) proposed a bridging model in order to obtain a better representation of the load distribution and the load transfer between tows, Figure 2.16(c).

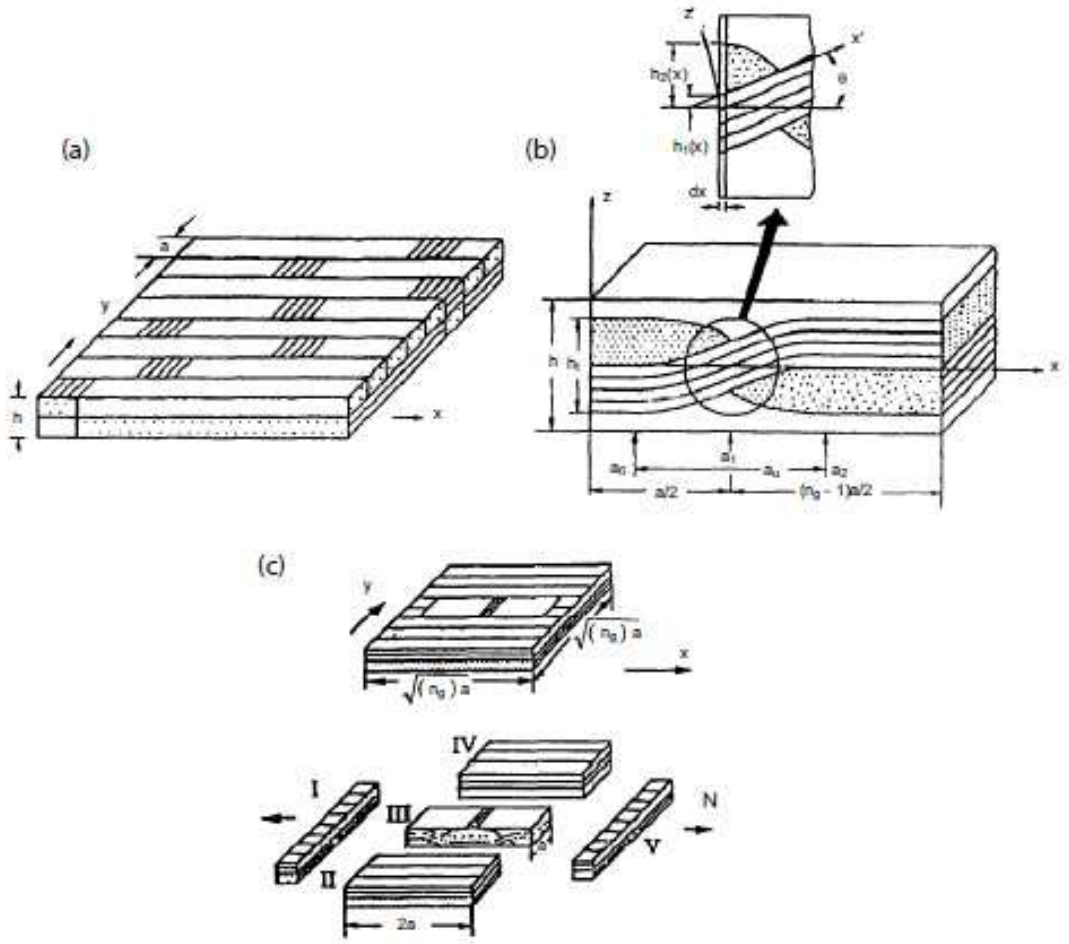

Figure 2.16: Models developed by Ishikawa and Chou (1983b): (a) mosaic model (b) fibre undulation model (c) bridging model.

Cox et al. (1994); McGlockton et al. (2003); Xu et al. (1995) have developed a so called binary model to compute the elastic constants of any textile composite. Fibre tows are modelled simply and reasonably as embedded 1D line elements. This method has been shown to provide accurate prediction of stiffness properties. Furthermore, it is robust and readily adaptable to provide insight into the effects of altering parameters such as tow waviness, tow misalignment, varying weave architectures, etc. However, this technique does not yield a detailed map of the stress field in a RUC or allow for cross-sectional variation of the tow geometry, as the fibre tow is simulated as a 1D line element with representative material properties.

Whitcomb et al. (2000) proposed systematic procedures for deriving boundary conditions for periodic sub-structures. By symmetry, they formulated and set up the boundary conditions of a partial unit cell that represent a portion of the RUC. Their analysis performed by identifying an identical coordinate system for all partial unit cells. Use of partial unit cells significantly reduces the computational effort. Tang and Whitcomb (2003) improved the derivation procedure to eliminate the need for a common point between the partial unit cells.

Naik and Ganesh (1992) presented two fabric composite models for the on-axes elastic analysis of two-dimensional orthogonal plain weave fabric lamina. These are two dimensional models taking into account the actual strand cross-section geometry, a possible gap between two adjacent strands, and the undulation and continuity of the strands along both warp and fill directions. They state that shape functions considered to define the geometry of the woven fabric lamina compare well with the photomicrographs of actual woven fabric lamina cross-sections. Naik and Ganesh (1995) extended this work to the prediction of thermoelastic properties.

Karkkainen et al. (2006) presented a direct micro-mechanical based finite element model for the analysis of a single-ply plain weave laminate, Figure 2.17a. This model considers bending effects which had been ignored in the conventional models by assuming a uniform stress state in the unit cell. The RUC is modelled as a linear-elastic thin Kirchhoff plate whose properties are defined by a homogenisation technique and periodic boundary conditions are assumed at the boundaries. The constitutive relationship for the homogenised plate is written in the form

$$\begin{Bmatrix} N_x \\ N_y \\ N_{xy} \\ -- \\ M_x \\ M_y \\ M_{xy} \end{Bmatrix} = \left(\begin{array}{ccc|ccc} A_{11} & A_{12} & A_{16} & B_{11} & B_{12} & B_{16} \\ A_{21} & A_{22} & A_{26} & B_{21} & B_{22} & B_{26} \\ A_{61} & A_{62} & A_{66} & B_{61} & B_{62} & B_{66} \\ -- & -- & -- & -- & -- & -- \\ B_{11} & B_{21} & B_{61} & D_{11} & D_{12} & D_{16} \\ B_{12} & B_{22} & B_{62} & D_{21} & D_{22} & D_{26} \\ B_{16} & B_{26} & B_{66} & D_{61} & D_{62} & D_{66} \end{array}\right) \begin{Bmatrix} \varepsilon_x \\ \varepsilon_y \\ \gamma_{xy} \\ -- \\ \kappa_x \\ \kappa_y \\ \kappa_{xy} \end{Bmatrix} \tag{2.1}$$

where N and M denote force- and moment-resultants and ε and κ denote mid-plane strain and curvatures. γ denotes the engineering shear strain. The 6×6 constitutive matrix is denoted by ABD and its 3×3 submatrices are denoted by A, B and D.

Kueh and Pellegrino (2007) developed a similar model for a single-ply triaxial woven composite but using beam elements to predict mechanical properties, Figure 2.17b. Through a series of experiments they showed that this simple model is capable of accurately predicting tensile, compressive, shear and bending stiffness. Datashvili et al. (2011) later replaced rigid connections between tow crossover points with elastic beam elements to capture thermal properties.

Jiang et al. (2007) proposed a domain superposition technique for the simulation of woven fabric composites. Instead of modelling the tows and the likely degenerated resin pockets regions among tows explicitly, this technique separately models the tow domain and the global domain which are both non-degenerated, and can thus be easily discretised using the traditional solid elements. During the solution process, the two domains are superimposed by coupling them together to produce the exact results. They state that the numerical simulation results of this technique correlate very well with the results of conventional finite element analysis.

Extensive research has been done on various aspects of composite in recent years. Internal geometry evaluation of non-crimp 3D orthogonal woven carbon fabric composite by Karahan et al. (2010) and work on in-plane permeability of triaxially braided reinforcements by Endruweit and Long (2011) to mention a few.

2.2.2 Common Failure Criteria

Failure criteria discussed in this section targets failure prediction of a lamina. However failure of a laminate can be predicted by applying these at lamina level. For

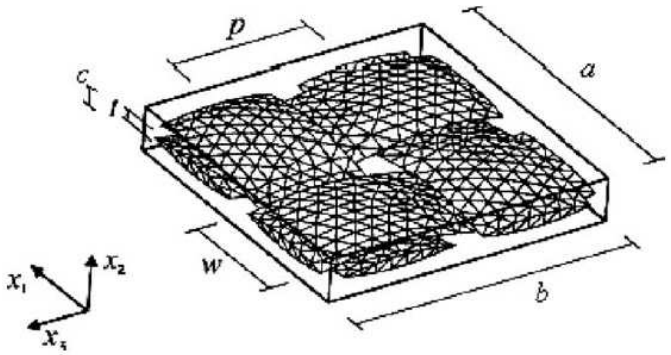

(a) Solid element model for single-ply plain-weave laminate by Karkkainen et al. (2006)

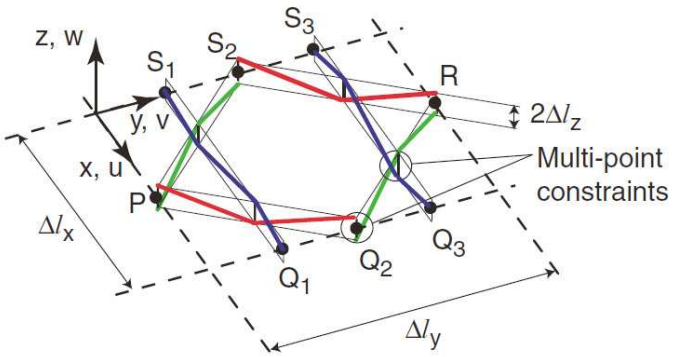

(b) Beam element model for single-ply tri-axial weave laminate by Kueh and Pellegrino (2007)

Figure 2.17: Representative unit cells for plain-weave and tri-axial weave laminates.

example first-ply failure considers failure of a single lamina as failure of the laminate.

Current designs of textile composites are often based on well know phenomenological failure criteria, which are originally developed for unidirectional composites. The maximum stress, maximum strain and interactive failure criteria proposed by Tsai-Wu and Hashin are commonly used in industry for predicting failure of composites (Daniel and Ishai, 2006).

The maximum stress criterion predicts failure of a single lamina when any principal material axis stress component exceeds the corresponding strength. Therefore, the following set of inequalities must be satisfied:

$$-\sigma_{1c}^{u} < \sigma_1 < \sigma_{1t}^{u} \tag{2.2a}$$

$$-\sigma_{2c}^{u} < \sigma_2 < \sigma_{2t}^{u} \tag{2.2b}$$

$$|\tau_6| < \tau_s^{u} \tag{2.2c}$$

where σ and τ are the direct and in-plane shear stresses; the subscripts 1, and 2 denote longitudinal and transverse directions and 6 denotes in-plane shear; the subscripts t, c and s denote denotes tension, compression and shear, respectively and the superscript u denotes the ultimate strength.

Similarly, the maximum strain criterion for a lamina predicts failure when any principal material axis strain component exceeds the corresponding ultimate strain. Therefore, the following set of inequalities must be satisfied:

$$-\epsilon_{1c}^{u} < \epsilon_1 < \epsilon_{1t}^{u} \tag{2.3a}$$

$$-\epsilon_{2c}^{u} < \epsilon_2 < \epsilon_{2t}^{u} \tag{2.3b}$$

$$|\epsilon_6| < \epsilon_s^{u} \tag{2.3c}$$

where ϵ denotes strain.

Tsai and Wu (1971) proposed a tensor polynomial theory by assuming the existence of a failure surface in the stress space. In contracted notation it takes the form

$$f_i\sigma_i + f_{ij}\sigma_i\sigma_j = 1 \tag{2.4}$$

where f_i and f_{ij} are the second- and fourth-order strength tensors, and i, j = 1,2 ..6. For a two dimensional stress state this can be reduced to

$$f_1\sigma_1 + f_2\sigma_2 + f_{11}\sigma_1^2 + f_{22}\sigma_2^2 + f_{66}\tau_6^2 + 2f_{12}\sigma_1\sigma_2 = 1 \tag{2.5}$$

They have shown that the strength coefficients f_i can be obtained by applying elementary loadings to a lamina and hence

$$f_1 = \frac{1}{\sigma_{1t}^u} - \frac{1}{\sigma_{1c}^u} \tag{2.6a}$$

$$f_2 = \frac{1}{\sigma_{2t}^u} - \frac{1}{\sigma_{2c}^u} \tag{2.6b}$$

$$f_{11} = \frac{1}{\sigma_{1t}^u\sigma_{1c}^u} \tag{2.6c}$$

$$f_{22} = \frac{1}{\sigma_{2t}^u\sigma_{2c}^u} \tag{2.6d}$$

$$f_{66} = \frac{1}{(\tau_6^u)^2} \tag{2.6e}$$

$$f_{12} = -\frac{1}{2}\sqrt{f_{11}f_{22}} \tag{2.6f}$$

Hashin and Rotem (1973) noted that failure of a lamina under a general in-plane loading can be characterised by two failure limits, one for fibre failure and the other for inter-fibre failure as follows:

$$\frac{|\sigma_1|}{\sigma_1^u} = 1 \tag{2.7a}$$

$$\left(\frac{|\sigma_2|}{\sigma_2^u}\right)^2 + \left(\frac{|\tau_6|}{\tau_6^u}\right)^2 = 1 \tag{2.7b}$$

The failure mechanics of textile composites is more complex since failure depends on weave style and detailed properties in addition to fibre and matrix properties. In fact, World Wide Failure Exercise carried by UK Institute of Mechanical En-

gineers and Engineering and Physical Sciences Research Council has shown how difficult it is to predict failure of unidirectional laminates under in-plane loading conditions (Hinton et al., 2004).

Most current failure criteria for woven composites are based on variations of the criteria presented above, applied at a laminate or micro-mechanical level. Although micro-mechanical models have been successfully employed in predicting thermoelastic properties (Chou, 1992; Kueh and Pellegrino, 2007) their use for strength prediction under multi-axial loading is still under development. Extensive research has been carried on prediction of strength under certain loading conditions by analyzing a RUC (Cox et al., 1994; Quek et al., 2004; Whitcomb and Srirengan, 1996). Karkkainen and Sankar (2007) have presented a failure envelope for textile composites in the form of a quadratic polynomial. This is done by extending the Tsai-Wu failure criterion to force and moment resultants. They have estimated failure parameters with aid of finite element calculations carried on a representative unit cell. A more detailed discussion of this procedure is presented in Chapter 6.

Chapter 3

Fabrication Procedures

This chapter presents the fabrication procedures followed to construct both tape-spring hinges and coupons for stiffness and strength characterisation. The chapter explains the process of manufacturing a composite specimen, including the machining of a tubular specimen.

The composite booms and other specimens considered in this research are made of two-ply plain weave carbon fibre laminates. To develop a better understanding of these materials and to better control the quality of the tested specimens, all specimens were constructed starting from a dry fabric that was impregnated with resin. The autoclave curing process was used to construct high quality specimens.

3.1 Construction of Tubes and Other Specimens

The carbon fibre fabric used was Hexcel high strength plain weave fabric, G0801-7-1020, consisting of 7.4 tows/cm 1K T300 fibres in warp and weft directions. The resin used was HexPly 913 epoxy resin, provided on a release paper. The material properties are provided in Chapter 4.

3.1.1 Resin Impregnation

One needs to be careful when working with dry fabric as it can be easily distorted. First the fabric was laid on a cutting table and the tows were checked to ensure that they were properly aligned. Next the edges of the required piece of fabric were marked with masking tape slightly larger than the required dimensions and cut along the centre lines of the masking tape. Then the fabric was smoothly laid on top of

a semi solid film of 913 resin, provided on a release paper. The film was released from the paper by ironing over the surface. The iron was heated to a temperature around 100 °C and smoothly moved over the release paper about five times. Next the resin impregnated fabric with release paper was cut to the exact dimensions and refrigerated. Once the resin had solidified the release paper could be smoothly peeled off. The resin film provided on the release paper has an areal weight of 30 g/m^2. If more resin is required then the same procedure can be repeated. The number of resin film layers used depends on the required fibre volume fraction.

3.1.2 Lay-Up

A 38 mm diameter stainless steel tube was used as a male mould for constructing the composite tubes. The tube surface was polished with numbers 180, 400 and 600 sandpapers and a fine steel wool to obtain a defect free surface. The surface was then cleaned with acetone and air dried for about fifteen minutes.

One of the main difficulties in constructing composite tubes, compared to flat or curved specimens is the separation of the cured specimen from the mandrel. Two different techniques were used to facilitate the release of the cured tube from the mandrel. The first method is to wrap the steel tube with a sheet of Poly Tetra Fluoro Ethylene (PTFE); Tygaflor release fabric was used for this purpose. The other method is to spray PTFE based dry film mould release onto the steel tube; Sprayon MR311 was used. Use of PTFE sheet forms an edge on the interior surface of the cured tube and hence the spraying technique was preferred.

At room temperature resin becomes sticky and it is quite difficult to handle. First, the resin impregnated fabric was laid on top of a Wrightlon 5200B P-3 perforated release film and carefully rolled onto the sprayed male mandrel. Extreme care was required during this process to avoid wrinkling. When a better outer surface finish was required, the release film was peeled off and the CFRP layer was covered with PTFE sheet. Next, the lay-up was inserted into a 50 mm diameter 2:1 heat shrinkable tube and heated using a heat gun set to 300 °C. This process helps to keep the fabric in place and avoids any trapped air bubbles. Then the entire component was covered with another release film and then with a breather blanket to facilitate the flow of air around the tube and so to make it permeable to create uniform vacuum. Two thermocouples were attached to the steel mandrel in order to monitor its temperature during the curing process.

In the case of flat specimens, the PTFE release fabric was laid on top of a stainless steel plate. Then the resin impregnated fabric was carefully laid on PTFE sheet and covered with perforated release film followed by a breather blanket.

3.1.3 Vacuum Stage

Two different arrangements were tested for applying vacuum to the tubes. The first was to place the whole lay-up on top of a flat steel plate, to cover it with a Wrightlon 7400 vacuum bag, and to seal it with tape sealant applied all around, Figure 3.1a. With this procedure the external pressure on the tube is not uniform and hence two thicker regions are formed in the cured tube with a region of uniform thickness in between, Figure 3.1b.

The second method was introduced to overcome the distortions mentioned above. This time the vacuum bag was placed around the tube and sealed to itself with tape, Figure 3.1c. This allows the vacuum bag to fully cover the tube and hence avoids any distortions, Figure 3.1d.

In both techniques two vacuum ports are placed at either end of the tube by cutting two holes in the vacuum bag. A vacuum gauge was connected to one port and air was pulled out with a vacuum pump connected to the other port. Then the package was tested for capability of holding a vacuum for one minute. The complete sequence from laying up to vacuum bagging is shown in Figure 3.2.

In the case of flat specimens, the lay-up was covered with a Wrightlon 7400 vacuum bag and sealed to the stainless steel plate with tape sealant applied all around.

3.1.4 Autoclave Curing

The vacuum ports were first connected to the autoclave and tested for one minute for leakage. Then two thermocouples were attached to the autoclave and a temperature controlled curing process was carried out. The laminate curing process is determined by the curing cycle of the resin used. The following cycle was applied while the laminate remains under vacuum throughout the entire process.

- Cure temperature: 125 °C
- Cure time: 60 minutes

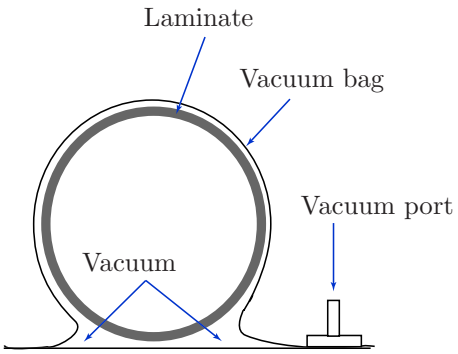

(a) Vacuum method 1

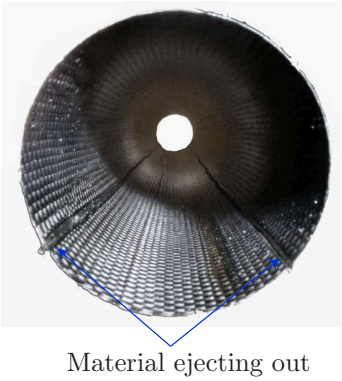

(b) Outcome of method 1

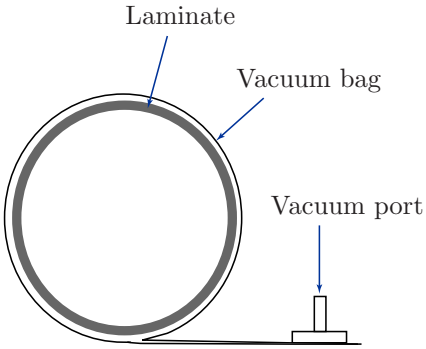

(c) Vacuum method 2

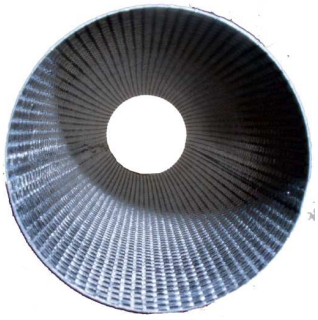

(d) Outcome of method 2

Figure 3.1: Different vacuum bagging techniques.

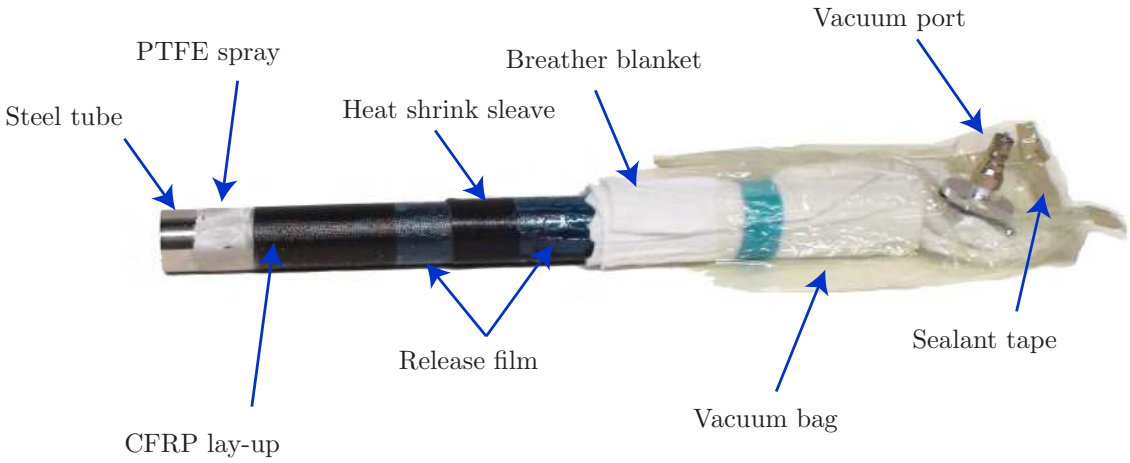

Figure 3.2: Complete lay-up sequence.

- Heat up rate: 3 °C per minute
- Cure pressure: 600 kPa
- Cool down rate: 3 °C per minute

After cooling down, all wrapping materials were removed and the composite tube was pulled out from the mandrel by twisting the tube. In the case of long tubes a higher torque was required to separate the laminate from the mandrel. Thermal cycling was occasionally used to weaken the bond between the laminate and the mandrel. Once the tube had been taken out the two ends were smoothed with number 400 sand paper.

3.2 Hinge Fabrication

CFRP components cannot be cut or ground with standard milling machines as slow rpm rotary tools tend to introduce micro cracks. Therefore, a Dremel 400 XPR high speed rotary tool set to 25,000 rpm was used for machining.

The cutting pattern was first marked on the composite tube with a white fine point oil based paint marker and clamped on a holding stand. The rotary tool was mounted on a three way finely adjustable table to follow the cutting pattern marked on the tube. Figure 3.3 shows the complete setup.

Straight portions of the slot were cut with a diamond cutting tool and the curved parts were ground with silicon oxide or carbide grinders. It is difficult to cut smooth curved edges because the manual motion of the cutting table is not precise. Therefore the edges were carefully smoothed with number 400 sand paper followed by number 600 sand paper.

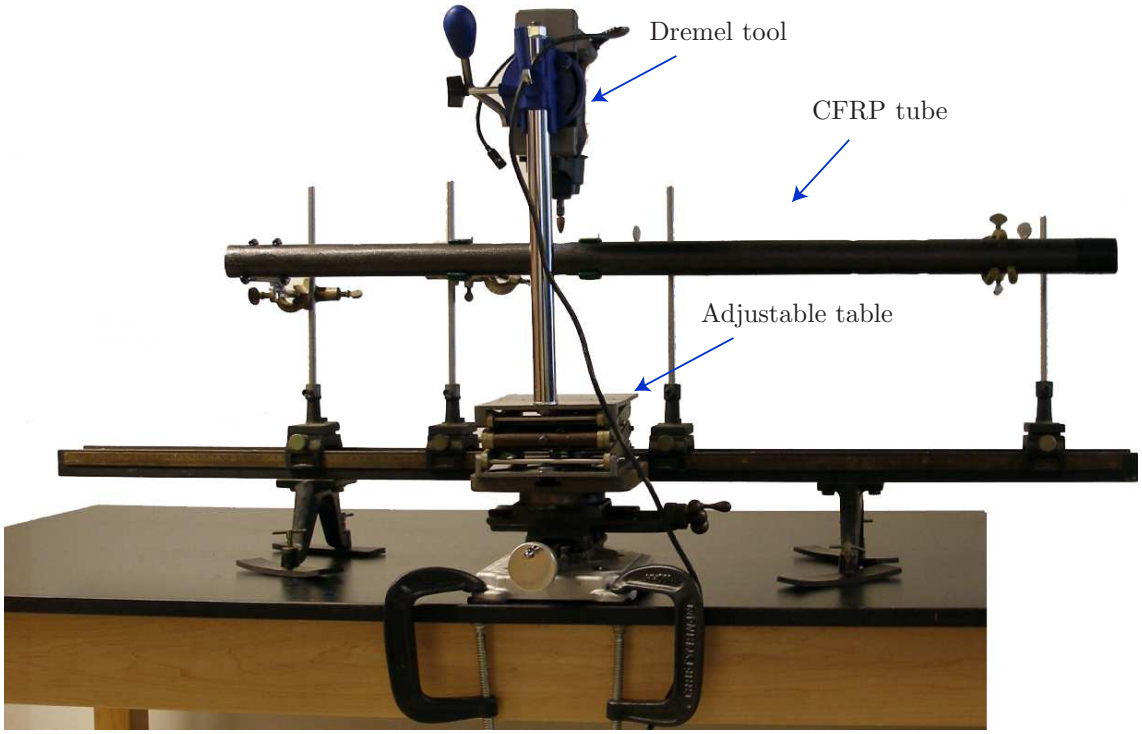

Figure 3.3: Fabrication setup.

Chapter 4

Material Characterisation

This chapter presents the material properties of both constituents and laminates. The fibre and resin properties are obtained from the manufacturers. The fibre volume fraction of the laminates is calculated by measuring the weights of the dry fabric and of the cured composite. The geometric properties of the cured tows are obtained from measurements of micrographs of the tow cross-sections.

The second part of the chapter describes various tests used for characterisation of the stiffness and strength properties of two-ply plain weave laminates. Standard tensile and four-point bending tests are performed on both two-ply 0/90 and ± 45 laminates for stiffness characterisation. Tensile, compression, shear, bending and twisting tests are performed to obtain five uniaxial strength parameters from which a failure criterion will be defined in Chapter 6. Five additional combined loading tests are carried out for verification of the failure criterion. These combined loading conditions are obtained by performing standard tensile and bending tests on off-axis specimens and/or initially curved specimens.

All loading conditions are defined with respect to the tow directions. Thus in each test the applied loading is transformed to the tow directions. It is also assumed that flattening a curved specimen introduces a uniform initial moment that remains constant during any subsequent test.

Here x and y denote orthogonal tow directions and x' and y' denote orthogonal loading directions, Figure 4.1. However, x' and y' are denoted as x and y when two sets of axes coincide.

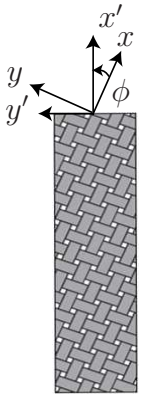

Figure 4.1: Definition of material and loading directions.

4.1 Constituent Properties

4.1.1 Fibre and Resin Properties

The composite material considered in this research are made of two-ply plain weave T300-1k carbon fibre fabric and HexPly 913 resin. The fibre and resin properties, obtained from the manufacturers are given in Table 4.1.

Properties	**T300 fibre**	**HexPly 913 resin**
Longitudinal stiffness, E_1 (N/mm^2)	233,000	3,390
Transverse stiffness, E_2 (N/mm^2)	23,100	3,390
Shear stiffness, G_{12} (N/mm^2)	8,963	1,210
Poisson′s ratio, ν_{12}	0.2	0.41
Density, ρ (kg/m^3)	1,760	1,230
Areal weight of fabric/film, W (g/m^2)	98	30

Table 4.1: Fibre and resin properties (Hexcel; Torayca)

4.1.2 Calculating Fibre Volume Fraction

The fibre volume fraction, V_f, and the matrix volume fraction, V_m, are defined as ratios with respect to the total volume of the composite, excluding voids. V_f can be defined as follows

$$V_f = \frac{\rho_m W_f}{\rho_m W_f + \rho_f W_m} \tag{4.1}$$

where ρ_f = density of fibres, ρ_m = density of matrix, W_f = areal weight of fibres and W_m = areal weight of matrix. The matrix volume fraction can be calculated from

$$V_m = 1 - V_f \tag{4.2}$$

Five 100 mm × 100 mm pieces of a two-ply plain weave laminate were weighed and a value for the average areal weight, W_c, was obtained, see Table 4.2.

Specimen:No.	weight/area (g/m^2)
1	280.39
2	280.62
3	279.60
4	276.70
5	285.35
Average	280.53

Table 4.2: Areal weight of cured samples

Hence the areal weight of the matrix is

$$W_m = W_{comp} - W_f = 280.53 - 98.0 \times 2 = 84.53 \text{ g/m}^2$$

Three resin film layers with two fabric layers were used in making these two-ply specimens. Therefore the above value of W_m is consistent with the properties given by the manufacturer, Table 4.1. Thus from Equation 4.1

$$V_f = \frac{1230 \times 196}{1230 \times 196 \times +1760 \times 84.53} = 0.62$$

Then from Equation 4.2

$$V_m = 1 - 0.62 = 0.38$$

4.1.3 Tow Geometry

Micrographs were used to measure the geometric properties of the tows, following the process in Yee (2006). A 20 mm × 10 mm composite specimen was held upright and submerged in a mixture of Epofix Resin and Epofix 81 Hardener with a ratio of 15 to 2. Subsequently, it was cured in a fume cupboard. The rate of curing was

proportional to the amount of hardener used in the mixture. A slower curing rate is preferred as it allows more time to release any trapped air bubbles.

The cured specimen was then ground to eliminate any additional epoxy resin on the surface. By gradually wearing off the surface, the composite specimen becomes fully exposed. The grinding process was then followed by a polishing process that aims to remove scars and scratches due to grinding. Before proceeding to polishing, the specimen was cleaned thoroughly under running water to avoid contamination from particles originating from the grinding process. After cleaning the specimen, it was first polished on a revolving plate using a piece of paper containing water based monocrystalline of particle size 6 micron. Then, it was cleaned again under running water before going through the same polishing procedures but with water-based monocrystalline of particle size 1 micron.

Once, the specimen surface had only minimal scars and scratches it was ready for observation under the Nikon Eclipse LV100 optical microscope with $\times 20$ magnification. An overlay of optical images taken in segments along the specimen is shown in Figure 4.2.

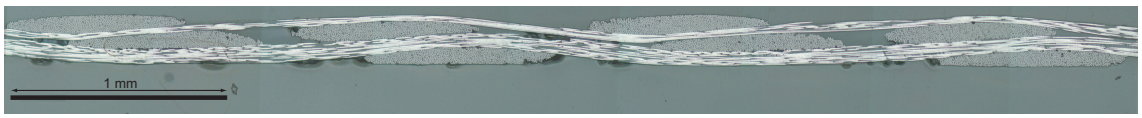

Figure 4.2: Micrograph of T300-1k/913 two-ply plain weave laminate

To determine the cross-sectional properties of a tow, a micrograph was loaded in the Autocad (2002) software and scaled with respect to the scale bar printed in the image by the microscope. The software allows to measure the dimensions and also to determine the area within an enclosed region defined by a closed line drawn along the edges of a tow. This analysis was carried out on ten tow sections obtained with four different composite specimen. The average properties that were obtained are given in Table 4.3.

Weave length, ΔL	2.664 mm
Maximum tow thickness, a	0.059 mm
Tow cross-sectional area	0.0522 mm^2

Table 4.3: Average geometric properties of a T300-1k/HexPly913 tow

4.2 Stiffness and Strength Characterisation Experiments

Interweaving and interlacing of the tows plays a major role in determining the mechanical response of textile composite materials. Extensive work has been done for developing standard test methods for textile composites (Masters and Portanova, 1996). ASTM D6856-2003 (2008) provides general guidelines for testing textile composites and necessary alterations that should be made before using standards developed for unidirectional laminates.

The stiffness and strength properties of the two-ply T300-1k/Hexcel 913 plain weave laminate were characterised by tensile, compressive, bending and combined failure tests described below.

All tests were done on an Instron 5569 materials testing machine with 50 kN and 1 kN load cells. All measurements of strain and deflection were made with Epsilon LE01 and LE05 laser extensometers.

4.2.1 Tensile Test

The tensile tests were conducted according to the ASTM D3039/D3039M-2008 (2008) test procedure with guidance from ASTM D6856-2003 (2008). Six 227 mm long and 25 mm wide specimens were constructed. 50 mm long and 25 mm wide aluminium-alloy tabs with 5° bevel angle were bonded to each specimen with high strength adhesive Devcon Plastic Welder. This leaves an exposed length of 127 mm. Retro-reflective strips were attached in the central region about 50 mm and 15 mm apart to measure the longitudinal and transverse strains, respectively.

Each specimen was connected to the tensile testing machine with wedge clamping jaws. The specimens were pulled at a rate of 2 mm/min while measuring the load with a 50 kN load cell. Few additional specimens were subjected to four cycles of 80% of the failure load to confirm that there is no hysteretic response.

4.2.2 Compression Test

Standard compression test procedures have been developed for thick composites, but these standards are not applicable here because thin specimens under compression fail by buckling. Thus, following Fleck and Sridhar (2005), the compression tests

were performed on short sandwich columns. In fact, Yee (2006) and Kueh (2007) used the same approach to estimate the compressive strength of plain weave and triaxial weave composites, respectively. It is important to select a suitable set of specimen dimensions when using short sandwich columns to achieve the required failure by fibre microbuckling (Fleck and Sridhar, 2005). Each specimen was made by bonding two 60 mm long and 40 mm wide composite face sheets to 12.5 mm thick Divinicell H200 PVC foam core with Devcon Plastic Welder. Then two aluminium-alloy end caps were bonded to the sandwich specimen to provide a uniform load distribution across the width of the specimen, Figure 4.3a.

During the compression test, additional lateral supports were provided by applying four PVC foam blocks clamped with 1 mm thick aluminium-alloy plates to prevent the face sheets from debonding from the foam core, Figure 4.3b. Two retro reflective strips were attached about 30 mm apart in the 10 mm wide central region for laser extensometer measurements, on both sides of the specimen. The specimens were loaded at a rate of 0.06 mm/min while using the 50 kN load cell.

4.2.3 Shear Test

The ASTM D3518/D3518M-1994 (2007) $[\pm 45]_{ns}$ tensile test method was used for measuring the in-plane shear strength. This method has been developed for measuring the shear strength of a lamina and is not used for laminates since the specimen is subjected to bi-axial tensile loads, in addition to shear. Thus a correction has to be made for estimating the pure shear strength, as will be explained in Section 6.3.1.

Ten two-ply ± 45 specimens with similar dimensions to the tensile specimens of Section 4.2.1 were made. However, 50 mm long emery cloth tabs were used instead of aluminium-alloy tabs. Two retro-reflective strips were attached 50 mm and 15 mm apart, respectively for the longitudinal and transverse strain measurements. Each specimen was pulled at a rate of 2 mm/min until failure.

4.2.4 Bending Test

Four-point bending tests and platen folding tests were conducted to measure the bending stiffness and strength, respectively.

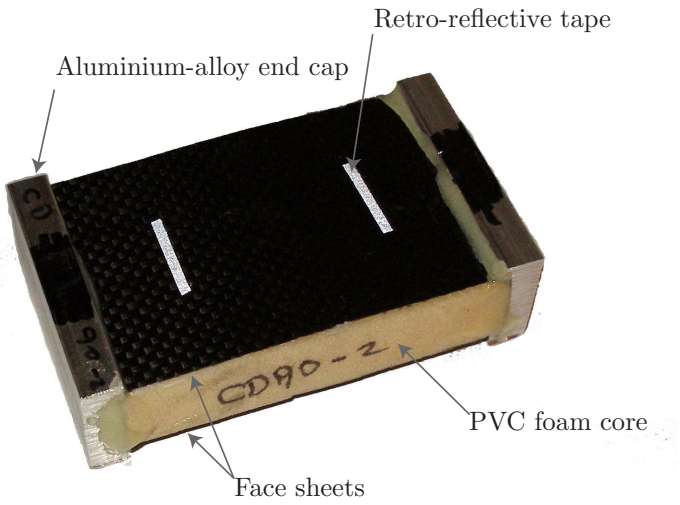

(a) Compression specimen

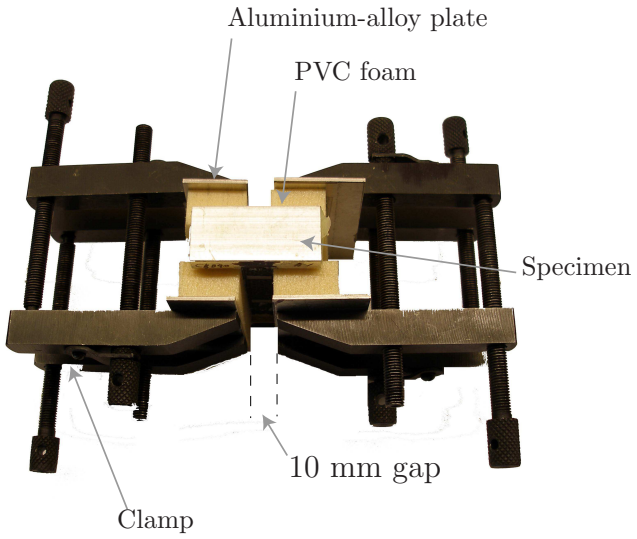

(b) Lateral support system

Figure 4.3: Compressive failure test.

4.2.4.1 Stiffness

A four-point bending configuration was chosen, instead of three-point bending, as it produces a region subject to a uniform bending moment and so it is more reliable. The test setup, based on ASTM D790M-1986 (1986), is shown in Figure 4.4. The span between the outer supports was 60 mm and the distance between the (inner) two points at which the loading was applied was set at 20 mm. The deflections imposed during this test were very small, the maximum value of relative displacement, δ, being in the region of 0.5 mm, corresponding to a deflection-to-span ratio of 40; the maximum value of the applied load was in the region of 2 N. Friction effects associated with longitudinal deflections at the supports were eliminated by taking the average response for both loading and unloading. 100 mm long and 50 mm wide specimens with both two-ply 0/90 and ± 45 arrangement were tested to measure bending stiffness along the fibres and at 45° to the fibres. Each specimen was tested twice by turning it upside down after the first test.

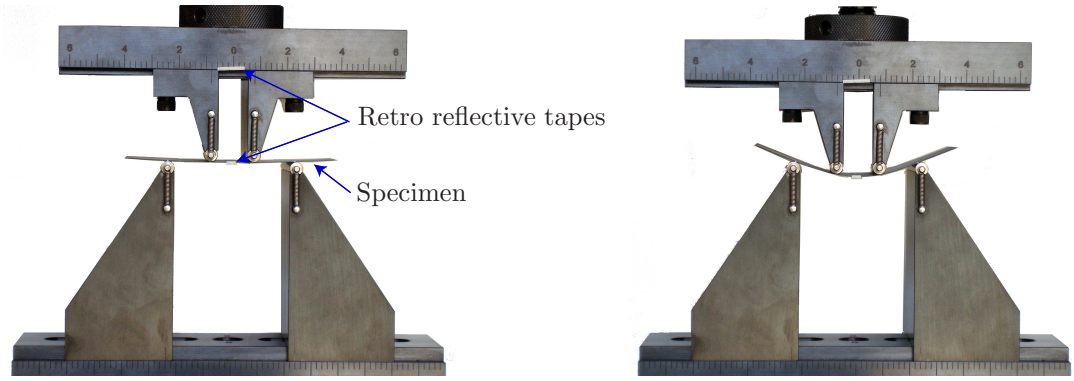

(a) Starting configuration (b) Loaded configuration

Figure 4.4: Four-point bending test setup.

4.2.4.2 Failure

Standard three-point or four-point flexural strength tests are not applicable for thin laminates, because the elastic deformation range is too large. Hence the platen folding test (Sanford et al., 2010), which aims to determine the smallest radius and the corresponding load to which a laminate can be folded before failure, was used. 100 mm long and 50 mm wide specimens were attached to two flat aluminium-alloy plates connected to the testing machine, Figure 4.5. Each specimen was compressed at a rate of 2 mm/min while recording the applied force with a 1 kN load cell. A

Sony Handycam HDR-XR500V digital video camera was used to record the test at a rate of 30 frames per second. The picture just before failure is used to measure the failure radius. However, this setup does not measure the transverse moment. Therefore the ABD stiffness matrix presented in Chapter 5 is used to estimate the transverse moment at failure.

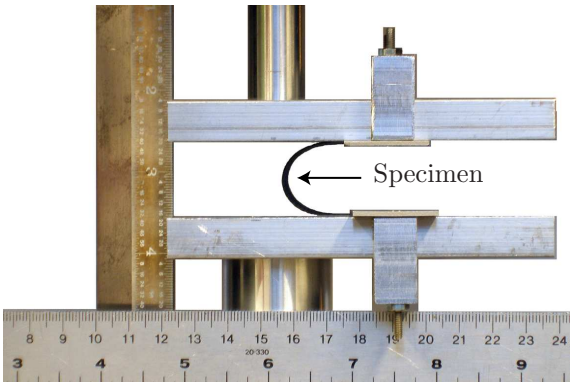

Figure 4.5: Platen folding test setup.

4.2.5 Twisting Test

It is not practical to apply large torsional rotation in a pure twisting test as the end conditions have to follow the non-linear geometric deformations required to eliminate the presence of other loading conditions. Instead, the platen folding test described in Section 4.2.4 was carried out on five two-ply ±45 laminates. Due to the off-axis fibre orientation of this type of specimen, this configuration applies a twisting moment in the tow directions, as well as biaxial bending moments. The calculation of the applied moments in the tow directions is presented in Section 4.3.5.

4.2.6 Biaxial Tests

The uniaxial test procedures described in Sections 4.2.1-4.2.5 can be applied to initially curved and/or off-axis specimen to obtain combined loading responses.

Initially curved specimens were first flattened and then tested in the tensile or bending configurations described above. This type of test allows to apply a certain load type, which depend on the selected test configuration, on a specimen subjected to a constant moment. Similar to the twisting and shear tests described earlier, off-axis fibre orientation can be used to introduce a combined axial loads and shear

or twisting loads. Specimens with different initial radii were used to vary applied constant moments.

4.2.6.1 In-Plane Loading

Off-axis tensile tests are commonly used as biaxial loading tests to verify material properties determined with standard uniaxial tests (Adams et al., 2003). Five $[30/-60]_2$ specimen were tested. The specimen dimensions and test procedure were similar to the shear tests described in Section 4.2.3. This configuration allows to investigate failure under combined biaxial and shear loads.

4.2.6.2 Axial-Bending Coupling

This type of coupling was achieved by performing tensile tests on initially curved two-ply 0/90 specimen, Figure 4.6a. The specimens were cured using 38 mm, 50 mm and 75 mm diameter cylindrical molds. Then each specimen was subjected to four-point bending to measure the moment required to flatten it, Figure 4.6b. It was assumed that a curved specimen behaves in a way similar to a flat specimen on the micro scale and that the moment required to flatten an initially curved specimen remains constant throughout the test. Each specimen was 125 mm long and 25 mm wide, with 25 mm long emery cloth tabs glued to each end. This provides a 75 mm test length. Retro-reflective strips were attached at 25 mm and 15 mm apart for longitudinal and transverse strain measurements, respectively. Shorter specimens were used due to difficulty in constructing long curved specimen. However, in each specimen the test length consisted of around 29 repeating unit cells, the length of a unit cell is 2.66 mm. ASTM D6856-2003 (2008) recommends the gauge area to be larger than at least two unit cells. Also retro-reflective strips were placed sufficiently away from the supports to minimise edge effects.

Three sets of curved specimens with initial longitudinal radius, r_x with 19.1 mm, 25.4 mm and 38.1 mm were tested to measure the interaction between N_x and M_x. Other sets of specimens with initial transverse radius, r_y equal to 25.4 mm and 38.1 mm were tested to measure the interaction between N_x and M_y.

4.2.6.3 Shear-Twist Coupling

Longitudinally curved two-ply ± 45 specimens were subjected to the same type of shear tests described in Section 4.2.3. This configuration applies all six loading

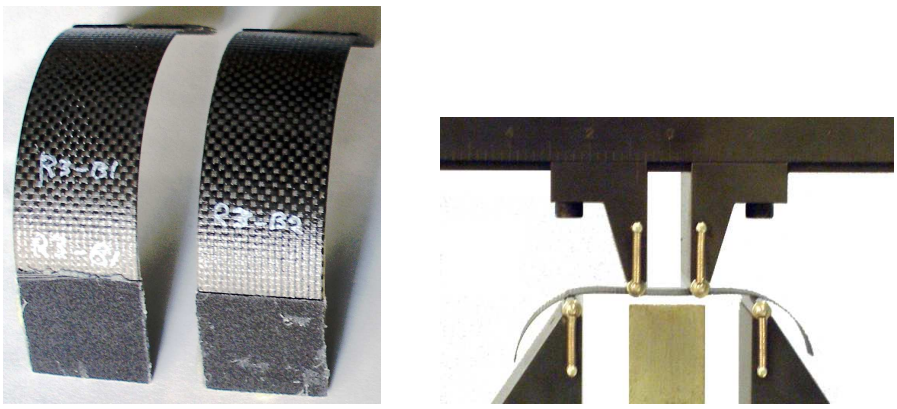

(a) Curved specimen (b) Measuring bending moment

Figure 4.6: Axial-bending interaction tests.

conditions on a specimen. The applied twisting moment can be varied by testing specimens with different initial curvatures.

4.2.6.4 Biaxial Bending

The bending failure test described in Section 4.2.4.2 can be applied to an initially transversely curved specimen to obtain a biaxial bending response.

Hence, an initially curved specimen was first flattened and then subjected to longitudinal bending up to failure. The applied transverse moment was varied by varying the initial curvature. It can be assumed that the applied bending moment has the value required to flatten the curved specimen and remains constant throughout the test. Biaxial bending tests were not performed during this research but instead the results obtained by Yee (2006) on a similar laminate were used.

4.2.6.5 Combined Bending-Twisting Loading

Introducing off-axis fibre orientation in the biaxial bending test described in Section 4.2.6.4 introduces both biaxial bending and twisting loads on the specimen. Different initially transversely curved off-axis specimens were used to vary the biaxial and twisting load combinations.

Two set of two-ply ±45 specimens with initial transverse radius of 25.4 mm and 38.1 mm were subjected to bending failure tests to investigate the coupling effects between bending and twisting.

4.3 Experimental Results

This section analyses the results obtained from the experiments described in Section 4.2. Note that due to symmetry of the laminate x and y can be interchanged. For each experiment the sample average, $\bar{x}$, sample standard deviation, s_{n-1} and sample coefficient of variation, CV are presented. These three quantities are defined as

$$\bar{x} = \frac{\left(\sum_{i=1}^{n} x_i\right)}{n} \tag{4.3}$$

$$s_{n-1} = \sqrt{\frac{(\sum_{i=1}^{n} x_i^2 - n\bar{x}^2)}{(n-1)}} \tag{4.4}$$

$$CV = \frac{100 \times s_{n-1}}{\bar{x}} \ \% \tag{4.5}$$

where x_i = measured or derived property and n = number of specimens.

4.3.1 Tensile Properties

Figure 4.7 shows a typical N_x vs. ε response obtained from the tensile tests and Table 4.4 summarises the initial stiffness and failure values that were obtained. Note that all these specimen were subjected to failure at multiple locations (failure code LMV in ASTM D3039/D3039M-2008 (2008)). Ideally, each specimen should fail in the middle region, but it is difficult to capture where the failure was initiated. A video taken with a Sony Handycam HDR-XR500V at 30 frames per second showed that failure occurs within a single frame which corresponds to 0.03 s. However, if failure was initiated near the ends then the obtained failure strength can be considered as a lower bound of the actual strength.

4.3.2 Compressive Properties

To measure the compressive failure strength it is required that the tested specimen should have failed by face sheet microbuckling, Figure 4.8. However it is almost impossible to achieve microbuckling of both sheets at the same time. Hence only the extensometer reading for the failed side was considered and the failure stress-

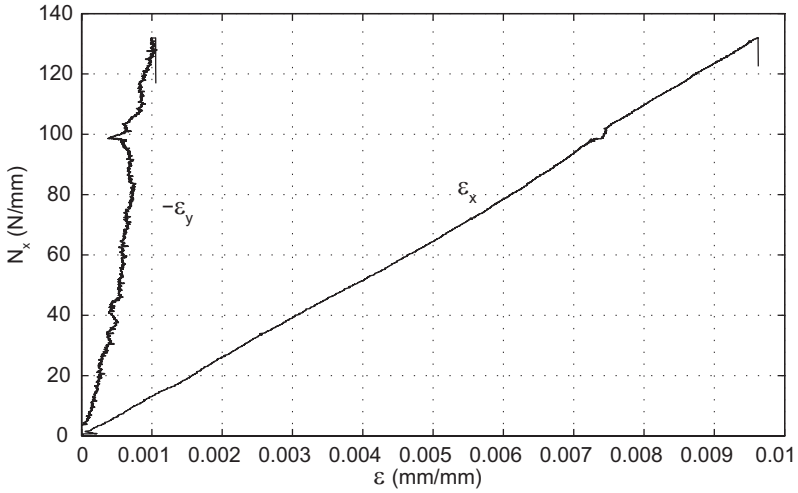

Figure 4.7: Typical tensile response.

Specimen	Stiffness (N/mm)	Poisson's ratio	ε_x (%)	N_x (N/mm)
TD90-1	13,110	0.10	0.96	133.60
TD90-2	12,250	0.05	1.05	135.80
TD90-3	13,220	0.12	1.06	143.20
TD90-4	12,070	0.14	1.04	141.00
TD90-5	13,150	0.13	1.01	138.50
TD90-6	13,130	0.12	0.99	144.70
$\bar{x}$	12,822	0.11	1.02	139.47
s_{n-1}	517	0.03	0.04	4.30
CV	4.03	29.3	3.80	3.08

Table 4.4: Tensile properties.

resultant was calculated by assuming that both sheets had been equally loaded. This value was modified to account for the load taken by the foam core.

$$N_{xc} = \frac{P - \sigma_{core} A_{core}}{2b} \tag{4.6}$$

σ_{core} was estimated from stress-strain response of PVC foam given by Fleck and Sridhar (2005).

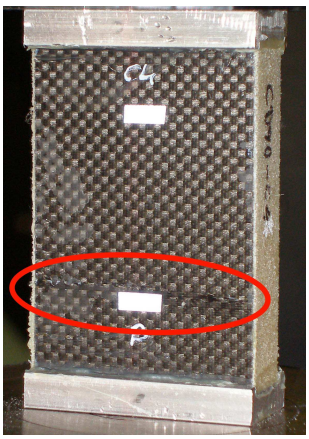

Figure 4.8: Face sheet microbukling.

Figure 4.9 shows compressive response for two sides of a single specimen. This is the closest agreement that was obtained among the two sides of any specimen, however the failure strengths obtained for other specimens were in the same range, Table 4.5.

4.3.3 Shear Properties

Table 4.6 shows the axial stiffness, Poisson's ratio and tensile strength of two-ply ± 45 laminate specimens.
Standard expressions to calculate the shear-resultant and shear strain are

$$N_{xy} = \frac{N_{x'}}{2} \tag{4.7a}$$

$$\gamma_{xy} = \varepsilon_{x'} - \varepsilon_{y'} \tag{4.7b}$$

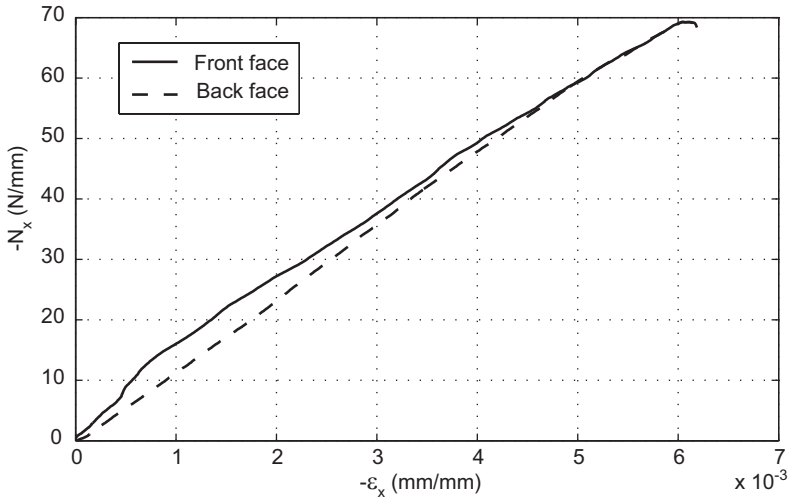

Figure 4.9: Compressive response measured from two sides of a single specimen.

Specimen label	$\lvert\varepsilon_x\rvert$ (%)	$\lvert N_x\rvert$ (N/mm)
CD90-1	0.69	63.23
CD90-2	0.70	77.89
CD90-3	0.61	67.50
CD90-4	0.64	60.56
CD90-5	0.59	57.36
CD90-6	0.66	64.96
CD90-7	0.49	59.50
CD90-8	0.56	59.49
CD90-9	0.56	60.39
CD90-10	0.61	63.66
$\bar{x}$	0.61	63.42
s_{n-1}	0.06	5.75
CV	10.59	6.10

Table 4.5: Compressive failure values

Specimen	Axial stiffness (N/mm)	Poisson's ratio	$N_{x'}$
TD45-1	2465	0.80	39.56
TD45-2	2708	0.78	39.54
TD45-3	2380	0.98	41.70
TD45-4	2061	0.85	38.54
TD45-5	2416	0.75	42.40
TD45-6	2556	0.88	40.26
TD45-7	2809	0.79	49.00
TD45-8	2653	0.79	38.34
TD45-9	2489	0.84	38.84
TD45-10	-	-	38.58
$\bar{x}$	2504	0.84	40.68
s_{n-1}	218	0.07	3.23
CV	8.71	8.37	7.94

Table 4.6: Axial stiffness, Poisson's ratio and tensile strength of two-ply ±45 laminate.

Figure 4.10 shows a typical shear response, obtained by applying the transformation in Equation 4.7 to the measurements obtained from an actual test.

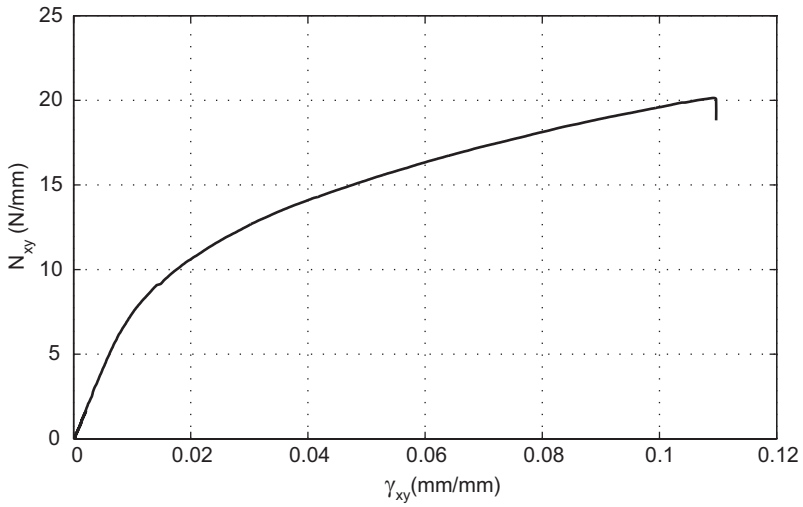

Figure 4.10: Typical shear response of a specimen.

It should be noted that in reality these specimens were subjected to N_x and N_y loads in addition to N_{xy}. In general these biaxial loads can be neglected for ±45 specimen made out of unidirectional fibres (Adams et al., 2003), however this assumption is not valid in estimating the laminate shear strength. Section 6.3.1 describes the correction procedure followed to estimate the pure shear strength.

4.3.4 Bending Properties

4.3.4.1 Stiffness

The four-point bending experiment explained in Section 4.2.4 measures the total force, P, required to bend the specimen and the relative displacement between the cross-head and the specimen, δ. Figure 4.11(a) shows a free-body diagram for this setup. Note that the mid-span, BC, is only subjected to a uniform moment and due to symmetry it can analysed as the cantilever shown in Figure 4.11(b). Hence the applied moment is given by

$$M = Ps \tag{4.8}$$

From the moment-curvature relationship

$$\kappa = \frac{M}{EI} = \frac{Ps}{EI} \tag{4.9}$$

where EI is the bending stiffness of the plate. The tip deflection of the cantilever is then

$$\delta = \frac{Ps^3}{2EI} \tag{4.10}$$

From Equations 4.9 and 4.10

$$\kappa = \frac{2\delta}{s^2} \tag{4.11}$$

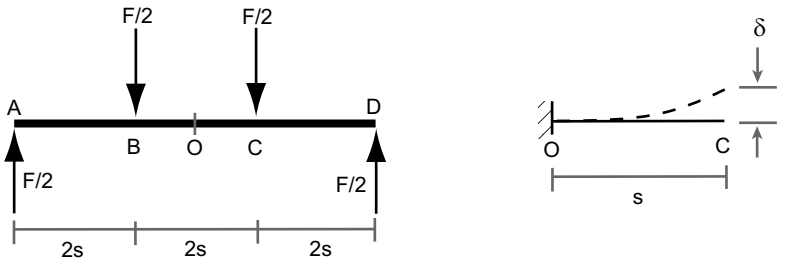

(a) (b)

Figure 4.11: Free body diagram of four-point bending configuration.

An average of the loading and unloading curves was taken to remove the effects of support friction. Figure 4.12 shows typical moment-curvature response of two-ply

0/90 laminates and Table 4.7 presents experimental results. The same procedure was followed to obtain the bending stiffness of two-ply ±45 laminates, Table 4.8.

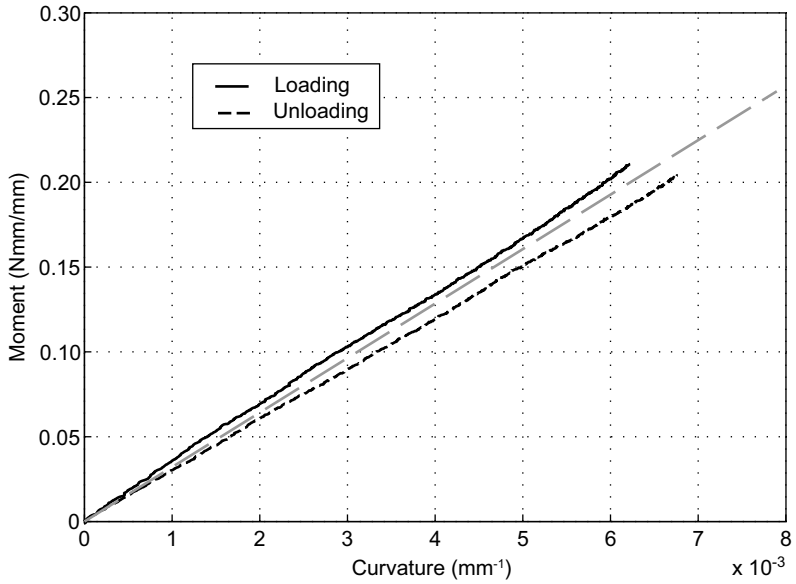

Figure 4.12: Moment-curvature response for two-ply 0/90 laminate.

Specimen	Stiffness (Nmm)
BD90-B1	45.81
BD90-B2	37.30
BD90-B3	40.88
BD90-B4	38.21
BD90-B5	30.58
BD90-B6	32.54
$\bar{x}$	37.55
s_{n-1}	5.54
CV	14.8

Table 4.7: Bending stiffness values for two-ply 0/90 laminate.

4.3.4.2 Strength

As mentioned before the platen folding test setup does not measure the transverse moment, which was estimated by converting the measured curvatures using the relationship given by ABD stiffness matrix presented in Chapter 5. It should be highlighted that two plies with the same tow orientation can be arranged in several

Specimen	Stiffness (Nmm)
BD45-1-top	21.27
BD45-2-top	21.37
BD45-3-top	21.17
BD45-4-top	21.18
BD45-5-top	21.67
$\bar{x}$	21.33
s_{n-1}	0.21
CV	0.96

Table 4.8: Bending stiffness values for two-ply ±45 laminate.

different ways. Thus two extreme cases, fibres in-phase and out-of-phase (Soykasap, 2006) were considered.

The failure radius was calculated by measuring the distance between the two aluminium-alloy platens from the picture taken just before failure.

Sanford et al. (2010) state that the curve formed by an initially flat coupon folded between two parallel platens is similar to an ellipse. The actual curve depends on the load distribution where the coupon transitions from being pressed flat against the platens to being free of the platens, as well as the constancy of the coupon bending stiffness. If a pure moment with no transverse force exists at this point the curve becomes circular. Sanford et al. (2010) have shown that in presence of a transverse force the curve can be described by an elastica. However for simplicity, here it is assumed that the specimen bends as a semicircle, Figure 4.13, and hence the applied moment resultant can be calculated as

$$M_x = \frac{PR^u}{b} \tag{4.12}$$

where P = applied load, R^u = failure radius and b = specimen width.

Table 4.9 presents the failure moments and curvatures obtained from platen folding tests performed on two-ply 0/90 laminates.

4.3.5 Twisting Strength

Table 4.10 shows the measured failure curvatures and moments in the loading directions. Note that $\kappa_{y'} = \kappa_{x'y'} = 0$, but $M_{y'} \neq 0$. The ABD stiffness matrix given in Equation 5.17 is used to calculate the moment in the transverse direction. It can

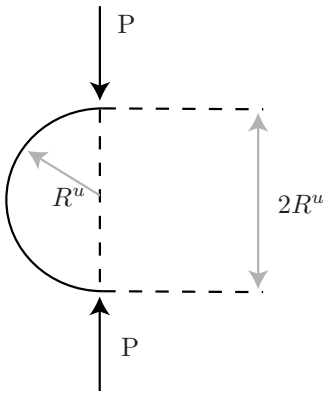

Figure 4.13: Bending failure sketch.

Specimen	κ_x (1/mm)	M_x (Nmm/mm)
BDF90-1	0.182	3.004
BDF90-2	0.175	2.718
BDF90-3	0.167	3.108
BDF90-4	0.170	3.312
BDF90-5	0.156	2.990
BDF90-6	0.170	3.055
BDF90-7	0.168	3.103
$\bar{x}$	0.170	3.041
s_{n-1}	0.008	0.178
CV	4.67	5.86

Table 4.9: Bending failure values for two-ply 0/90 laminate.

be shown that

$$M_{x'} = D_{11}^{\pm 45} \kappa_{x'} \tag{4.13a}$$

$$M_{y'} = D_{12}^{\pm 45} \kappa_{x'} \tag{4.13b}$$

$$M_{x'y'} = 0 \tag{4.13c}$$

However it should be noted that the ABD matrix was developed to capture the initial stiffness of the laminate. Comparing $M_{x'}$ from Equation 4.13(a) with the measured value from Table 4.10 it can be seen that there is a 40% stiffness reduction. Assuming that the transverse stiffness is subjected to a similar reduction, we obtain

$$M_{y'} = 0.6 \times D_{12}^{\pm 45} \kappa_{x'} \tag{4.14}$$

Once $M_{x'}$ and $M_{y'}$ are known they can be transformed to the tow directions with the standard transformation

$$M_x = \frac{M_{x'} + M_{y'}}{2} \tag{4.15a}$$

$$M_y = M_x \tag{4.15b}$$

$$M_{xy} = \frac{M_{y'} - M_{x'}}{2} \tag{4.15c}$$

These equations confirm that the specimens were subjected to M_x and M_y loads in addition to M_{xy}, and hence this is not a pure twisting experiment. The procedure followed to obtained the pure twisting strength is explained in Section 6.3.2.

4.3.6 Combined Loading Results

This section presents the results obtained from the combined loading tests.

4.3.6.1 Off-Axis Tensile Strength

Table 4.11 shows the axial strength of a two-ply 30/-60 laminate. Using standard transformations it can be shown that the force resultants along the tow directions

Specimen	$\kappa_{x'}$ (1/mm)	$M_{x'}$ (Nmm/mm)
BDF45-1	0.235	3.063
BDF45-2	0.219	3.208
BDF45-3	0.232	3.155
BDF45-4	0.234	2.962
BDF45-5	0.236	3.473
$\bar{x}$	0.231	3.172
s_{n-1}	0.007	0.192
CV	3.02	6.07

Table 4.10: Bending failure values for two-ply ±45 laminate.

are given by

$$N_x = \cos^2\phi \; N_{x'} \tag{4.16a}$$

$$N_y = \sin^2\phi \; N_{x'} \tag{4.16b}$$

$$N_{xy} = \sin\phi\cos\phi \; N_{x'} \tag{4.16c}$$

Specimen	$N_{x'}$ (N/mm)
TD30-1	45.69
TD30-2	45.44
TD30-3	45.53
TD30-4	48.01
TD30-5	50.62
$\bar{x}$	47.06
s_{n-1}	2.26
CV	4.80

Table 4.11: Tensile failure values for $[30/\text{-}60]_2$ laminate.

4.3.6.2 Axial-Bending Interaction

Table 4.12 presents the failure strengths obtained for longitudinally curved specimens. In all cases failure occurred in the middle region of these specimens.

Table 4.13 shows the failure values of N_x with the applied M_y values, obtained from tensile tests carried out on transversely curved specimens. Note that the

Specimen	r_x (mm)	N_x (N/mm)	M_x (Nmm/mm)
TBD90-D1.5-1	19.1	68.96	1.986
TBD90-D1.5-2	19.1	72.37	1.986
TBD90-D1.5-3	19.1	81.52	1.986
TBD90-D1.5-4	19.1	110.10	1.854
TBD90-D1.5-5	19.1	93.75	1.722
TBD90-D2-1	25.4	73.80	1.357
TBD90-D2-2	25.4	81.17	1.265
TBD90-D2-3	25.4	119.00	1.447
TBD90-D2-4	25.4	86.12	1.327
TBD90-D2-5	25.4	87.56	1.560
TBD90-D2-6	25.4	99.25	1.600
TBD90-D2-7	25.4	104.70	1.610
TBD90-D3-1	38.1	108.20	0.989
TBD90-D3-2	38.1	104.70	0.775
TBD90-D3-3	38.1	103.90	0.743

Table 4.12: Tensile failure values for longitudinally curved two-ply 0/90 laminate.

transverse moment was not measured in this case but taken as the average obtained from curved specimens with the same initial curvature in Table 4.12.

Specimen	r_y (mm)	N_x (N/mm)	M_y (Nmm/mm)
TBD90-D2Y-1	25.4	145.20	1.349
TBD90-D3Y-1	38.1	136.80	0.836
TBD90-D3Y-2	38.1	136.10	0.836

Table 4.13: Tensile failure values for transversely curved two-ply 0/90 laminate.

4.3.6.3 Shear-Twist Interaction

Table 4.14 shows the failure force resultants in the loading direction. The specimens considered here had an initial radius of 38.1 mm.

4.3.7 Bending-Twisting Interaction

Table 4.15 shows the failure moments obtained by testing transversely curved two-ply ±45 specimens. The moment resultants in the tow directions were calculated by following the same procedure described in Section 4.3.5, however note that in the present case $\kappa_{y'} \neq 0$. Hence Equation 4.14 should be replaced by

Specimen	$N_{x'}$ (N/mm)	$M_{x'}$ (Nmm/mm)
STD45-1	42.42	0.043
STD45-2	39.30	0.039
STD45-3	42.04	0.042
STD45-4	38.36	0.040
$\bar{x}$	40.53	0.041
s_{n-1}	2.01	0.002
CV	4.95	4.45

Table 4.14: Tensile failure values for longitudinally curved two-ply ±45 laminate.

$$M_{y'} = 0.6 \times (D_{12}^{45}\kappa_{x'} + D_{22}^{45}\kappa_{y'}) \tag{4.17}$$

where $\kappa_{y'} = \frac{1}{r_{y'}}$

Specimen	$r_{y'}$ (mm)	$\kappa_{x'}(1/mm)$	$M_{x'}$ (Nmm/mm)
BTD45-D2Y-1	25.4	0.262	3.552
BTD45-D2Y-2	25.4	0.283	3.870
BTD45-D3Y-1	38.1	0.254	3.092
BTD45-D3Y-2	38.1	0.276	3.035
BTD45-D3Y-3	38.1	0.252	2.838
BTD45-D3Y-4	38.1	0.226	2.677
BTD45-D3Y-5	38.1	0.224	2.804

Table 4.15: Bending failure values for transversely curved two-ply ±45 laminate.

Chapter 5

Micro-Mechanical Modelling

Thin laminates made from fabric layers are not modelled accurately by classical laminate theory (Soykasap, 2006). Hence, the two-ply laminate studied in this dissertation is modelled as a linear-elastic thin Kirchhoff plate whose properties are defined by a homogenisation technique. The first part of the chapter explains our method for estimating the tow properties and for constructing the homogenised plate model. Then our stiffness predictions are compared with the experimental results obtained from Chapter 4. Finally an attempt is made to use homogenisation in reverse to predict material failure.

5.1 Estimating Tow Properties

In order to construct the micro-mechanical model, one first needs to estimate the tow properties. Each tow is modelled as a three-dimensional continuum having transversely isotropic properties.

5.1.1 Engineering Constants

The five independent engineering constants are determined as follows (Daniel and Ishai, 2006). The longitudinal extensional modulus and the Poisson's ratios are obtained from the rules of mixtures

$$E_1 = E_{1f}V_f + E_m(1 - V_f) \tag{5.1}$$

$$\nu_{12} = \nu_{13} = \nu_{12f} V_f + \nu_m (1 - V_f) \tag{5.2}$$

The transverse extensional modulus can be estimated with the Halpin-Tsai semi-empirical relation

$$E_2 = E_3 = E_m \frac{1 + \chi \eta V_f}{1 - \eta V_f} \tag{5.3}$$

where

$$\eta = \frac{E_{2f} - E_m}{E_{2f} - \chi E_m} \tag{5.4}$$

and the parameter χ is a measure of reinforcement of the composite that depends on the fibre geometry, packing geometry, and loading conditions. This has been set to 2.0 (Daniel and Ishai, 2006).

The shear modulus $G_{12} = G_{13}$ is found from the Halpin-Tsai semi-empirical relation (Daniel and Ishai, 2006)

$$G_{12} = G_{13} = G_m \frac{(G_{12f} + G_m) + V_f (G_{12f} - G_m)}{(G_{12f} + G_m) - V_f (G_{12f} - G_m)} \tag{5.5}$$

The in-plane shear modulus, G_{23}, is obtained by solving the following quadratic equation (Quek et al., 2003):

$$\left(\frac{G_{23}}{G_m}\right)^2 A + \left(\frac{G_{23}}{G_m}\right) B + C = 0 \tag{5.6}$$

where

$$\begin{aligned} A &= 3V_f (1 - V_f)^2 \left(\frac{G_{12f}}{G_m} - 1\right) \left(\frac{G_{12f}}{G_m} + \zeta_f\right) \\ &+ \left[\left(\frac{G_{12f}}{G_m}\right) \zeta_m + \zeta_m \zeta_f - \left(\left(\frac{G_{12f}}{G_m}\right) \zeta_m - \zeta_f\right) (v_f)^3\right] \\ &\times \left[\zeta_m V_f \left(\frac{G_{12f}}{G_m} - 1\right) - \left(\left(\frac{G_{12f}}{G_m}\right) \zeta_m + 1\right)\right] \end{aligned} \tag{5.7}$$

$$\begin{aligned} B &= -6V_f(1-V_f)^2\left(\frac{G_{12f}}{G_m}-1\right)\left(\frac{G_{12f}}{G_m}+\zeta_f\right) \\ &+ \left[\left(\frac{G_{12f}}{G_m}\right)\zeta_m+\left(\frac{G_{12f}}{G_m}-1\right)V_f+1\right] \\ &\times \left[(\zeta_m-1)\left(\frac{G_{12f}}{G_m}+\zeta_f\right)-2(V_f)^3\left(\left(\frac{G_{12f}}{G_m}\right)\zeta_m-\zeta_f\right)\right] \\ &+ (\zeta_m+1)V_f\left(\frac{G_{12f}}{G_m}-1\right)\left[\frac{G_{12f}}{G_m}+\zeta_f+\left(\left(\frac{G_{12f}}{G_m}\right)\zeta_m-\zeta_f\right)(V_f)^3\right] \end{aligned} \tag{5.8}$$

$$\begin{aligned} C &= 3V_f(1-V_f)^2\left(\frac{G_{12f}}{G_m}-1\right)\left(\frac{G_{12f}}{G_m}+\zeta_f\right) \\ &+ \left[\left(\frac{G_{12f}}{G_m}\right)\zeta_m+\left(\frac{G_{12f}}{G_m}-1\right)V_f+1\right] \\ &\times \left[\frac{G_{12f}}{G_m}+\zeta_f+\left(\left(\frac{G_{12f}}{G_m}\right)\zeta_m-\zeta_f\right)(V_f)^3\right] \end{aligned} \tag{5.9}$$

and

$$\zeta_m = 3-4\nu_m \tag{5.10}$$

$$\zeta_f = 3-4\nu_{12f} \tag{5.11}$$

The transverse Poisson's ratio ν_{23} can be calculated from

$$G_{23} = \frac{E_2}{2(1+\nu_{23})} \tag{5.12}$$

Table 5.1 presents the tow properties obtained using these equations with $V_f' = 0.68$. The measured V_f from experiments was 0.62 but in calculating the tow properties this value was increased to 0.68 to compensate for the additional resin that is added at the tow interfaces, when setting up the micro-mechanical model. This will be explained in more detail in Section 5.2.

Material Properties	Value
Longitudinal stiffness, E_1 (N/mm^2)	159,520
Transverse stiffness, $E_2 = E_3$ (N/mm^2)	11,660
Shear stiffness, $G_{12} = G_{13}$ (N/mm^2)	3,813
In-plane shear stiffness, G_{23} (N/mm^2)	3,961
Poisson′s ratio, $\nu_{12} = \nu_{13}$	0.267
Poisson′s ratio, ν_{23}	0.472

Table 5.1: Properties of cured T300-1k/913 tow

5.1.2 Geometry

The most important geometric parameters that are required for accurate modelling of the woven laminate are the tow cross-sectional shape and area, the tow waviness and the ply arrangement. As described in Section 4.1.3 this particular laminate has a weave length $\Delta L = 2.664$ mm, a tow cross-sectional area of 0.0522 mm^2, and a maximum tow thickness $a = 0.059$ mm.

5.1.2.1 Tow Cross-Section and Waviness

In the simplest micro-mechanics model the tows were initially modelled as wavy beams having an equivalent rectangular cross-sectional area (Mallikarachchi and Pellegrino, 2008) but in this model the beams are constrained only along their centre lines and so the distributed nature of the constraint provided across the tow width is neglected. Hence this model did not capture Poisson's effects accurately, in particular it provided rather poor predictions of A_{12} and gave $D_{12} = 0$ (see Section 5.3).

The next step was to use a solid model with the same equivalent rectangular cross-section but with a piecewise linear centre lines, Figure 5.1a. This provides a good connection between warp and weft tows in the overlapped regions. However, the tow undulation regions are not in contact and also the transitions between the two types of regions are not smooth.

To get uniform contact between the tows and to provide a smooth transition both tow cross-section and waviness were then defined with three different orders of sine waves. The surfaces of each tow were thus defined by

$$z = a\left(\pm 2 \pm \sqrt[d]{\left|\sin\left(\frac{2\pi x}{\Delta L}\right)\right|} \pm \sqrt[d]{\left|\sin\left(\frac{2\pi y}{\Delta L}\right)\right|}\right) \tag{5.13}$$

where the sign of the first term is + for the upper ply and − for the lower ply; the signs of the second and third terms are respectively $(+,+)$ for the top surface of the ply, $(+,-)$ or $(-,+)$ for the interface between the two tows, and $(-,-)$ for the lower surface of the ply. Note that the x, y, z coordinate system is such that the tow centre lines lie in planes parallel to xz and yz. The exponent d is set to 1, 2 and 4 to obtain sin, $\sqrt{\sin}$ and $\sqrt[4]{\sin}$ variation. Figures 5.1b and 5.1c show cross-sections and 3D views of the two different models based on sine wave variation. Note that Whitcomb and Srirengan (1996) also used a sine wave to define the waviness and tow cross-section in their model.

This representation of the tow surfaces ensures a perfect geometric match between tows in the same ply, however tows in different plies touch only at four points and hence there is a gap that has been filled with 6-node triangular prisms modelling additional neat resin. The fibre volume fraction of the tows was changed accordingly to maintain the overall fibre volume fraction at $V_f = 0.62$. Therefore V_f was set to 0.68 in estimating the tow properties for the model sine wave with $d = 4$.

5.1.2.2 Ply Arrangement

When considering a two-ply woven laminate there are infinitely many possible arrangements of the plies, obtained by translating one ply with respect to the other ply. Soykasap (2006) considered two extreme configurations known as fibres in-phase and fibres out-of-phase. Hence all five tow arrangements presented in Section 5.1.2.1 were considered for both of these extreme cases. Figure 5.2 shows two different arrangements.

5.2 Homogenised Plate Model

Figure 5.3 shows a finite element model where the tow geometries were defined by the fourth root of a sine wave and the two plies are in phase. The model consists of 1520 and 3200, 6-node triangular prisms elements, respectively for each tow and for the additional resin. The boundary nodes were attached by means of rigid vertical beams to dummy nodes lying in the mid-plane. Each dummy node was related to the corresponding dummy node opposite by means of a constraint equation that enforces periodic boundary conditions. These equations prescribe the relative displacements and rotations of the dummy nodes in terms of the mid-plane strains and out-of-plane

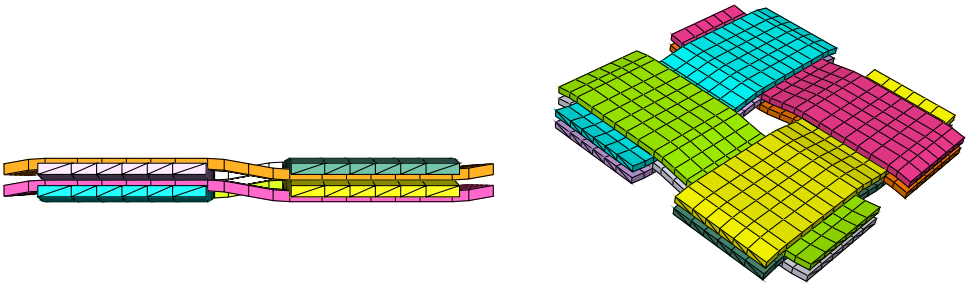

(a) Rectangular

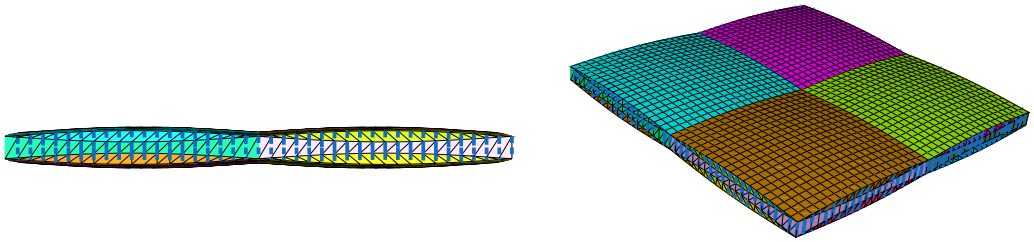

(b) Sine wave ($d = 1$)

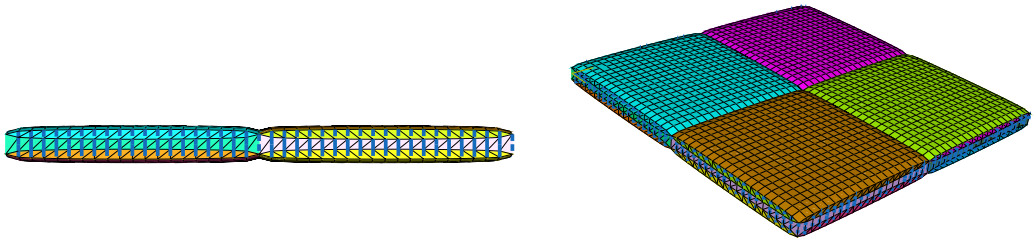

(c) Fourth root of a sine wave ($d = 3$)

Figure 5.1: Unit cell geometry with different cross-sectional profiles and waviness.

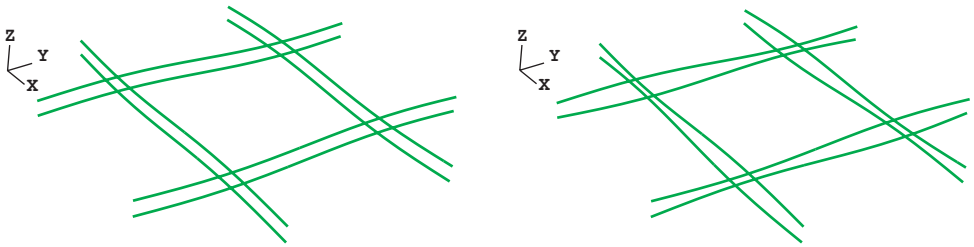

(a) Fibres in-phase (b) Fibres out-of-phase

Figure 5.2: Two extreme ply arrangements.

curvatures of the homogenised Kirchhoff plate.

$$\varepsilon_x = \frac{\partial u}{\partial x} \tag{5.14a}$$

$$\varepsilon_y = \frac{\partial v}{\partial y} \tag{5.14b}$$

$$\gamma_{xy} = \frac{\partial u}{\partial y} + \frac{\partial v}{\partial x} \tag{5.14c}$$

$$\kappa_x = -\frac{\partial^2 w}{\partial x^2} \tag{5.14d}$$

$$\kappa_y = -\frac{\partial^2 w}{\partial y^2} \tag{5.14e}$$

$$\kappa_{xy} = -2\frac{\partial^2 w}{\partial x \partial y} \tag{5.14f}$$

It should be noted that the *engineering shear strain* and *twice the surface twist* have been used in the definition of these deformation variables.

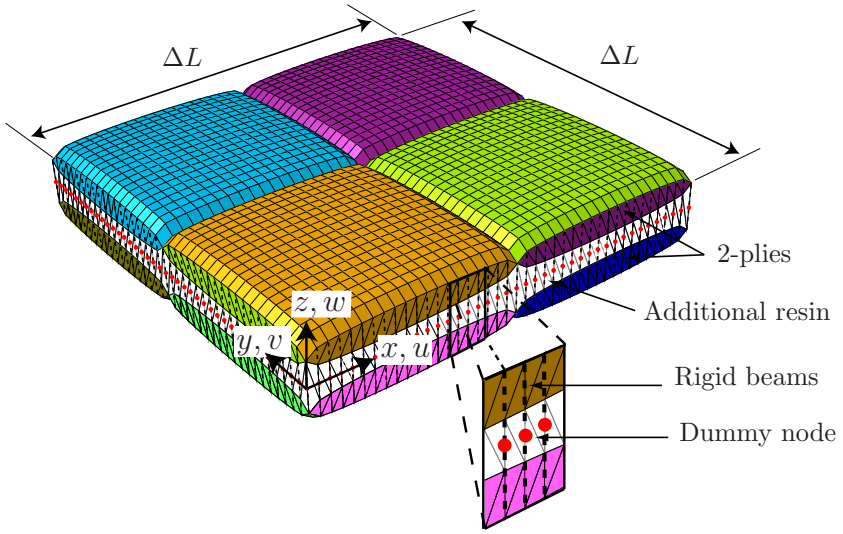

Figure 5.3: Finite element model for unit cell of two-ply laminate (with 3× magnification in z-direction).

The following constraint equations were enforced

$$\Delta u^x = \varepsilon_x \, \Delta L \tag{5.15a}$$
$$\Delta v^x = \frac{1}{2} \, \gamma_{xy} \, \Delta L \tag{5.15b}$$
$$\Delta u^y = \frac{1}{2} \, \gamma_{xy} \, \Delta L \tag{5.15c}$$
$$\Delta v^y = \varepsilon_y \, \Delta L \tag{5.15d}$$
$$\Delta w^x = -\frac{1}{2} \, \kappa_{xy} \, y \, \Delta L \tag{5.15e}$$
$$\Delta w^y = -\frac{1}{2} \, \kappa_{xy} \, x \, \Delta L \tag{5.15f}$$
$$\Delta \theta_x^x = -\frac{1}{2} \, \kappa_{xy} \, \Delta L \tag{5.15g}$$
$$\Delta \theta_y^x = \kappa_x \, \Delta L \tag{5.15h}$$
$$\Delta \theta_x^y = -\kappa_y \, \Delta L \tag{5.15i}$$
$$\Delta \theta_y^y = \frac{1}{2} \, \kappa_{xy} \, \Delta L \tag{5.15j}$$
$$\Delta \theta_x^z = 0 \tag{5.15k}$$
$$\Delta \theta_y^z = 0 \tag{5.15l}$$

where subscripts denote the deformation directions and superscripts denote the direction of a pair of boundary nodes, with equal x or y coordinates.

The constitutive relationship for the homogenised plate, in the coordinate directions defined in Figure 5.3, is written in the form of an ABD stiffness matrix.

The entries of the ABD matrix for the two-ply laminate were computed using Virtual Work (Karkkainen et al., 2006; Kueh and Pellegrino, 2007), after carrying out six separate Abaqus/Standard analyses, each corresponding to a unit amplitude of the six deformation variables $\varepsilon_x, \ldots, \kappa_{xy}$. The following ABD matrix was thus obtained

$$ABD^{0/90} = \left(\begin{array}{ccc|ccc} 13009 & 1085 & 0 & 0 & 0 & 0 \\ 1085 & 13009 & 0 & 0 & 0 & 0 \\ 0 & 0 & 667 & 0 & 0 & 0 \\ -- & -- & -- & -- & -- & -- \\ 0 & 0 & 0 & 41.3 & 1.5 & 0 \\ 0 & 0 & 0 & 1.5 & 41.3 & 0 \\ 0 & 0 & 0 & 0 & 0 & 2.3 \end{array}\right) \tag{5.16}$$

where the units are N and mm.

The constitutive matrix $ABD^{\pm 45}$ for a two-ply ± 45 laminate is obtained by a $45°$ rotation of the ABD matrix in Equation 5.16, which gives

$$ABD^{\pm 45} = \left(\begin{array}{ccc|ccc} 7714 & 6380 & 0 & 0 & 0 & 0 \\ 6380 & 7714 & 0 & 0 & 0 & 0 \\ 0 & 0 & 5962 & 0 & 0 & 0 \\ -- & -- & -- & -- & -- & -- \\ 0 & 0 & 0 & 23.6 & 19.1 & 0 \\ 0 & 0 & 0 & 19.1 & 23.6 & 0 \\ 0 & 0 & 0 & 0 & 0 & 19.9 \end{array}\right) \tag{5.17}$$

5.3 Experimental Validation of Material Stiffness

The constitutive matrices obtained from the homogenised plate models in Section 5.2 were verified against the tensile and bending experimental results obtained in Sections 4.3.1, 4.3.3 and 4.3.4.

The use of narrow specimens in the tension tests ensures that the transverse and shear stress resultants are negligibly small, i.e. $N_{y'} \approx N_{x'y'} \approx 0$ in the middle of the specimen. Hence, denoting by a_{ij} the entries of the in-plane compliance matrix obtained by inverting the upper-left 3×3 submatrix of the corresponding ABD matrix

$$\varepsilon_{x'} = a_{11} N_{x'} \tag{5.18}$$

and therefore $1/a_{11}$ can be compared to the measured ratio $N_{x'}/\varepsilon_{x'}$.

In the four-point bending tests wider specimens were used and hence the transverse and twisting curvatures were negligibly small, i.e. $\kappa_{y'} \approx \kappa_{x'y'} \approx 0$, and so the

measured ratio $M_{x'}/\kappa_{x'}$ can be directly compared to D_{11} of the corresponding ABD matrix.

A comparison of the experimental results to the predictions based on the models described in Section 5.1.2.1 is presented in Tables 5.2 and 5.3 for two-ply 0/90 and ±45 laminates, respectively.

Tow model	$\frac{1}{a_{11}}$		ν_{12}		D_{11}	
	in-phase	out-of-phase	in-phase	out-of-phase	in-phase	out-of-phase
Beam	8,192	11,992	0.32	0	45.4	34.4
Solid (rectangular)	8,259	11,141	0.21	0.02	43.0	32.8
Solid (sin)	11,629	12,108	0.08	0.04	45.0	41.5
Solid ($\sqrt{\sin}$)	12,905	-	0.08	-	47.0	-
Solid ($\sqrt[4]{\sin}$)	12,919	13,643	0.08	0.04	41.3	36.8
Experiments	12,833		0.11		37.84	

Table 5.2: Material Properties for two-ply plain weave T300-1k/913, 0/90 laminate.

Tow model	$\frac{1}{a_{11}}$		ν_{12}		D_{11}	
	in-phase	out-of-phase	in-phase	out-of-phase	in-phase	out-of-phase
Beam	440	446	0.96	0.96	23.3	23.5
Solid (rectangular)	1,342	1,342	0.87	0.88	24.4	23.0
Solid (sin)	2,088	2,088	0.84	0.84	25.7	25.9
Solid ($\sqrt{\sin}$)	2,390	-	0.83	-	27.2	-
Solid ($\sqrt[4]{\sin}$)	2,437	2,438	0.83	0.83	23.6	22.4
Experiments	2504		0.84		21.67	

Table 5.3: Material Properties for two-ply plain weave T300-1k/913, ±45 laminate.

Note that there is a significant variation in the bending stiffness of the homogenised plate between the in-phase and out-of-phase 0/90 laminate. This variation was also evident in the experiments as the bending stiffness varied from 31 Nmm to 45 Nmm (see Table 4.7). However in the case of ±45 laminates the difference is rather small. Based on comparison of all three stiffness properties for both 0/90 and ±45 laminates, the solid model with fourth root of sine wave and fibres in-phase was selected. The tubular booms that will be discussed in the following chapters

of this dissertation use a ±45 laminate, hence the ABD stiffness matrix defined in Equation 5.17 will be used as the material stiffness from here onwards.

5.4 Failure Analysis

Once a homogenised material model is used to compute the structural behaviour of a deployable boom the output is defined in the form of stress-resultants and mid-plane strains and curvatures and then the question that arises is whether the material of the boom is able to carry the stress resultants, or undergo these deformations, without damage. Therefore, the possibility of using the homogenisation analysis in reverse to determine the safety of the structure is investigated here.

Verification of failure analysis was carried out by applying a known failure load to the micro-mechanical model presented in Section 5.2. A failure analysis was performed in the micro-mechanical model with a selected failure criterion to check whether it actually predicts failure. For simplicity tension, compression, shear and bending failure tests were considered.

This was studied by applying 80% and 100% of the failure strains or curvatures obtained from uniaxial strength tests described in Chapter 4, to the equations defining the periodic boundary conditions, Equation 5.15. The 100% loading was used to check if the micro-mechanical model predicts that the failure occurs before this limit and the 80% loading to confirm it is not overconservative.

5.4.1 Strain Based Criterion

Following Yang et al. (2005), the maximum fibre strain was obtained by computing the average fibre strain in a moving window with a width equal to half a tow width and then selecting the maximum average value from the micro-mechanical model. Similarly, the maximum resin strain was obtained by computing 1) the maximum half-tow averaged normal strain in the direction perpendicular to the fibres in the same moving window and 2) the maximum average principal strain in the resin filling the space between the two-plies, and then choosing the maximum of the two.

To establish if the structure is able to withstand this deformation, the maximum normal strain in the fibre direction was compared with the failure strain of T300 fibres (1.5%, Torayca), and the maximum resin strain was compared with the failure strain of HexPly 913 epoxy resin in pure tension. This was calulated to be 1.93% by

dividing the tensile strength (Hexcel) by the tensile modulus and assuming linear-elastic behaviour up to failure.

5.4.2 Stress Based Criteria

Both the maximum stress and Tsai-Wu failure criteria were considered. In order to apply a stress based criterion, the tow strengths need to be known. It is assumed that the failure of each tow is similar to that of a unidirectional laminate. Pinho et al. (2006) present strength properties of a T300/913 unidirectional laminate, Table 5.4.

Material Properties	Value
Longitudinal tensile strength, σ_{1t}^{u} (N/mm^2)	2005
Longitudinal compressive strength, σ_{1c}^{u} (N/mm^2)	1355
Transverse tensile strength, σ_{2t}^{u} (N/mm^2)	68
Transverse compressive strength, σ_{2c}^{u} (N/mm^2)	198
Shear strength, τ_{s}^{u} (N/mm^2)	150

Table 5.4: Strength properties of T300/913 uni-directional laminate (Pinho et al., 2006).

Failure calculations were performed at each element in the micro-mechanical model with either failure criterion. The laminate failure can be defined as either failure of a single element, which defines failure initiation, or a certain percentage of elements failing for ultimate failure.

5.4.3 Validation

Two sets of analyses are carried out, with the actual failure strains and curvatures obtained from the experiments and 80% of these values.

It was found that the maximum strain failure criterion does not indicate failure at 100% loading for tensile and compressive loading. Table 5.5 shows the maximum fibre and resin strains corresponding to 100% loading. Note that the ultimate fibre and resin strains are 1.5% and 1.93%, respectively, see Section 5.4.1.

On the other hand the stress based failure criterion was over-conservative. The analysis shows that the laminate cannot take even 80% of loading for tensile, shear and bending. Table 5.6 shows the percentage of elements are deemed to have failed by the two criteria, for a load of 80% of the actual failure strains and curvatures.

Figures 5.4a shows contours of the fibre strains and Figures 5.4b and 5.4c show the failed elements for an imposed curvature of 80% the actual failure curvature, using the maximum stress and the Tsai-Wu criterion, respectively.

Loading	Max. fibre strain (%)	Max. resin strain (%)
Tension	0.78	1.55
Compression	-0.54	-1.40
Shear	0.25	4.00
Bending	0.95	2.11

Table 5.5: Maximum fibre strain (averaged over half a tow width) and resin strains corresponding to measured failure loads.

Loading	Max. Stress	Tsai-Wu
Tension	50	50
Compression	0	0
Shear	95	95
Bending	20	30

Table 5.6: Percentage of elements that have failed under 80% of the failure loading.

5.4.4 Conclusions

Even though the micro-mechanical model is fairly accurate in capturing the material stiffness, its failure predictions are quite poor. The exact tow geometry may not matter in predicting the stiffness but it is clearly important in failure analysis as stress concentrations will depend on geometry.

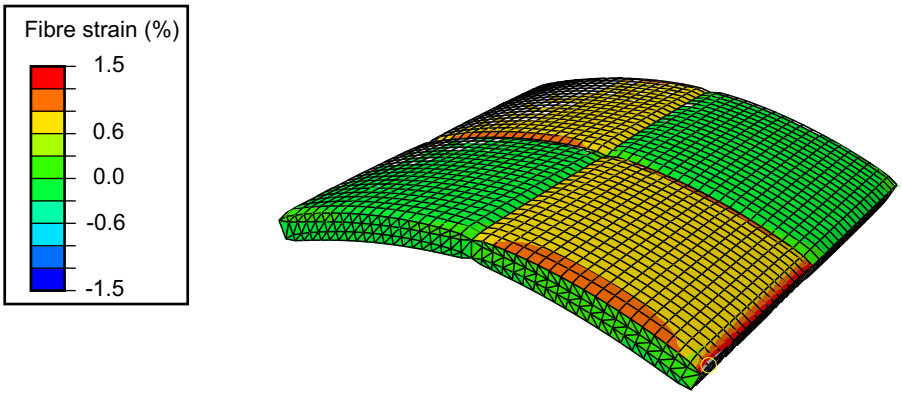

(a) Fibre strain distribution

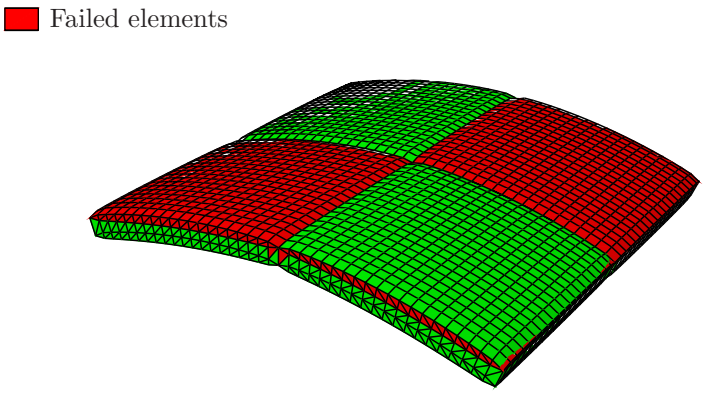

(b) Maximum stress

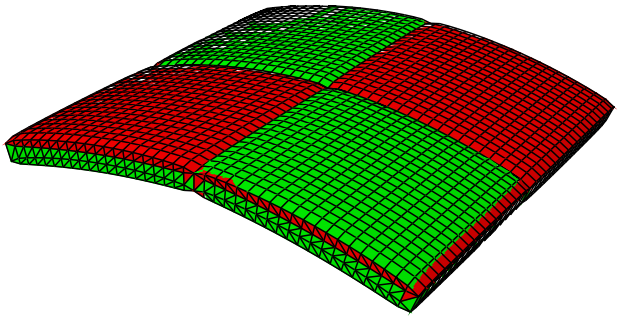

(c) Tsai-Wu

Figure 5.4: Failure analysis of laminate subjected to 80% bending load.

Chapter 6

Failure Criterion

This chapter presents a six-dimensional failure criterion defined in terms of stress-resultants. A quadratic failure locus presented in the literature is examined first. First this locus was constructed using the uniaxial strength experiments performed in Chapter 4 and then the combined loading test results were used to verify the accuracy of the locus. It is shown that this quadratic locus works well for in-plane loading conditions but not for bending or if this is an interaction between in-plane and bending loads. The second part of the chapter describes an alternative failure locus defined in terms of three inequalities that define failure due to in-plane, bending and interaction between in-plane and bending loads.

6.1 Quadratic Failure Locus

Karkkainen and Sankar (2007) have presented a failure envelope for textile composites in the form of a quadratic polynomial. This locus was defined by extending the Tsai-Wu failure criterion to force and moment resultants. The values of the failure parameters were estimated with the aid of finite element calculations carried out on a representative unit cell. It should be noted that Manne and Tsai (1998) have used a similar strain based criterion in their work on the design optimisation of composite plates. The applicability of Karkkaninen and Sankar's failure criterion for our two-ply plain weave laminate is investigated here.
The quadratic polynomial in six-dimensional space can be expressed as

$$\hat{f}_i\hat{\sigma}_i + \hat{f}_{ij}\hat{\sigma}_i\hat{\sigma}_j = 1 \tag{6.1}$$

where $\hat{\sigma}_i = N_x,\ N_y,\ N_{xy}$ for $i = 1,\ 2,\ 3$ and $M_x,\ M_y,\ M_{xy}$ for $i = 4,\ 5,\ 6$. $\hat{f}_i$ and $\hat{f}_{ij}$ represent 27 failure coefficients such that Equation 6.1 defines failure when its magnitude exceeds 1. $\hat{f}_i$ and the diagonal terms $\hat{f}_{ii}$, define the effects corresponding to individual uniaxial loads. The non-diagonal terms $\hat{f}_{ij}$ when $i \neq j$, define coupling between different loading conditions.

Due to the symmetry of the laminate these (the strength parameters do not change if x and y are exchanged) 27 failure coefficients can be reduced to 16. Also, because the sign of the shear, bending and twisting loads should not affect the failure locus, $\hat{f}_3 = \hat{f}_4 = \hat{f}_5 = \hat{f}_6 = 0$, i.e. pure bending strength should not depend on whether the applied moment is positive or negative. Similarly, all $\hat{f}_{ij}$ terms for $i = 3,...,6$ or $j = 3,...,6$ when $i \neq j$ are equal to zero, i.e. the failure moment of an axially loaded plate should be the same regardless of bending direction. However, it should be noted that in Karkkanien and Sanker's work the non-diagonal terms were not set to zero.

Hence, the quadratic polynomial can be expressed in terms of only 6 coefficients $\hat{f}_1,\ \hat{f}_{11},\ \hat{f}_{12},\ \hat{f}_{33},\ \hat{f}_{44}$ and $\hat{f}_{66}$. These coefficients can be calculated if there is a sufficient number of known failure points by following a similar approach to Tsai and Wu (1971).

$$\hat{f}_1 = \frac{1}{F_{1t}} - \frac{1}{F_{1c}} \tag{6.2a}$$

$$\hat{f}_{11} = \frac{1}{F_{1t}F_{1c}} \tag{6.2b}$$

$$\hat{f}_{33} = \frac{1}{F_3^2} \tag{6.2c}$$

$$\hat{f}_{44} = \frac{1}{F_4^2} \tag{6.2d}$$

$$\hat{f}_{66} = \frac{1}{F_6^2} \tag{6.2e}$$

Considering the similarity of this failure criterion to Tsai-Wu failure criterion for in-plane loading, $\hat{f}_{12}$ can be approximated as

$$\hat{f}_{12} = -\frac{\hat{f}_{11}}{2} \tag{6.3}$$

Therefore the quadratic polynomial can be obtained from the tension, compres-

sion, shear, bending and twisting failure strength experiments presented in Chapter 4. The five combined loading experiments that were performed can be used to verify the accuracy of the quadratic polynomial given in Equation 6.1.

6.2 Application of Quadratic Criterion

The five uniaxial strengths required to construct the quadratic failure envelope can be estimated from the first five results determined in Section 4.3. Here the failure strengths are taken as the averages obtained from each set of experiments. Because in the shear and twisting tests, the laminate was subjected to additional biaxial loads, the pure strengths are estimated by extrapolation as will be described in Section 6.3. Table 6.1 shows the failure strengths.

Strength	Value
$F_{1t} = F_{2t}$, N/mm	139.47
$F_{1c} = F_{2c}$, N/mm	63.42
F_3, N/mm	17.73
$F_4 = F_5$, Nmm/mm	3.04
F_6, Nmm/mm	0.92

Table 6.1: Uniaxial failure strengths.

Once the uniaxial failure parameters are obtained, the six failure coefficients can be calculated using Equations 6.2 and 6.3. Thus the six-dimensional ellipsoid given in Equation 6.1 can be defined.

At the next stage, the five sets of experimental results for combined loading were used to test the accuracy of this six-dimensional ellipsoid. This check was done by considering three sections of the ellipsoid for, in-plane loading, bending and axial-bending interaction. It was observed that the failure criterion satisfies the additional results for the in-plane loading conditions but not the other two.

Plotting the axial-bending interaction results obtained in Section 4.3.6.2 shows that the interaction between N_x and M_x is not quadratic, Figure 6.1, indeed all of the experimentally determined failure points fall inside the locus. Note that red, light blue and purple stars indicate specimens with initial curvatures 19.1 mm, 25.4 mm and 38.1 mm, respectively. It can be concluded that the quadratic failure locus defined by Equation 6.1 is not valid for this laminate.

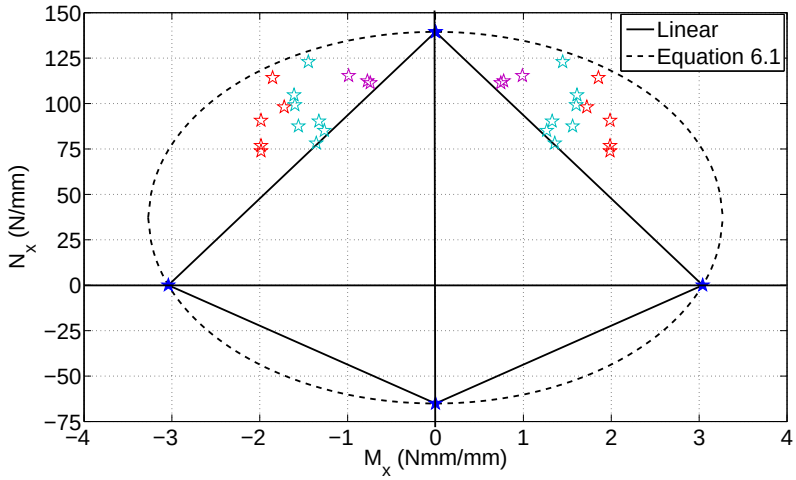

Figure 6.1: Axial-bending interaction.

6.3 Alternative Failure Locus

Section 6.2 has shown that the failure locus defined by a single polynomial does not work well for a two-ply plain-weave laminate. Therefore an attempt is made to construct an alternative failure envelope on the basis of the experimental observations. The loading space is divided into three parts, which take into account in-plane loading, bending loading and the interaction between in-plane and bending loads separately.

6.3.1 In-Plane Failure

In the case of in-plane loading all moment resultants are zero and hence in-plane failure can be defined by an equation of the type of Equation 6.4.

$$\hat{f}_1(N_x + N_y) + \hat{f}_{11}(N_x^2 + N_y^2) + \hat{f}_{12}N_xN_y + \hat{f}_{33}N_{xy}^2 = 1 \tag{6.4}$$

The shear strength results presented in Section 4.3.3 were determined in the presence of axial loads N_x and N_y. Note that these shear tests were in fact tensile tests performed on 45° off-axis specimens. Thus, from Equation 4.16 it can be shown that loads in the tow directions $N_x = N_y = N_{xy} = N_{x'}/2$. Substituting N_x, N_y and N_{xy} with $N_{x'}/2$ in Equation 6.4 and by solving for F_3

$$F_3 = \frac{1}{\sqrt{\hat{f}_{33}}} = \frac{N_{x'}^2}{\sqrt{4 - (4\hat{f}_1 N_{x'} + (2\hat{f}_{11} + \hat{f}_{12})N_{x'}^2)}} \tag{6.5}$$

Hence F_3 can be calculated from average $N_{x'}$ given in Table 4.6.

Figures 6.2a and 6.3a show the cross-sections of the failure locus for $N_y = 0$ and N_{xy}= 0, respectively, along with the failure points used to construct the locus.

The off-axis tensile test results presented in Section 4.3.6.1 are used for validation. Figure 6.2b and 6.3b show the cross-sections of the locus when $N_y = 11.77$ N/mm and $N_{xy} = 20.38$ N/mm, respectively. Note that these figures present all of the failure points obtained from the off-axis experiments but the cross-sections of the locus were chosen for the average values of N_y and N_{xy}. In both cases, the failure points lie outside the locus which provides confidence in using Equation 6.4.

6.3.2 Bending Failure

Yee (2006) showed that for thin plain weave laminate the failure curvature along a tow direction is independent of the curvature applied in the orthogonal direction. Figure 6.4 shows the biaxial bending moment locus constructed from Yee's failure curvature locus using the ABD stiffness matrix given in Equation 5.16 for our material, allowing for a 40% stiffness reduction at failure. Note that the failure moment envelope is almost square, like Yee's failure curvature locus. This implies that M_x is independent of M_y.

The twisting failure tests carried out in Section 4.3.5 were subjected to biaxial bending in addition to twist. Hence the pure twisting strength was calculated as follows.

From Table 4.10 and Equation 4.15 the average moments for flat ±45 laminates are $M_x = M_y = 2.87$ Nmm/mm and $M_{xy} = 0.30$ Nmm/mm. Note that in-plane loads are all zero, $N_x = N_y = N_{xy} = 0$. Since we already decided that M_x and M_y are independent from each other and assuming quadratic interaction between M_x and M_{xy}

$$\begin{aligned} \hat{f}_{44} M_x^2 + \hat{f}_{66} M_{xy}^2 &= 1 \\ F_6 &= \frac{M_{xy}}{\sqrt{1 - \hat{f}_{44} M_x^2}} \end{aligned} \tag{6.6}$$

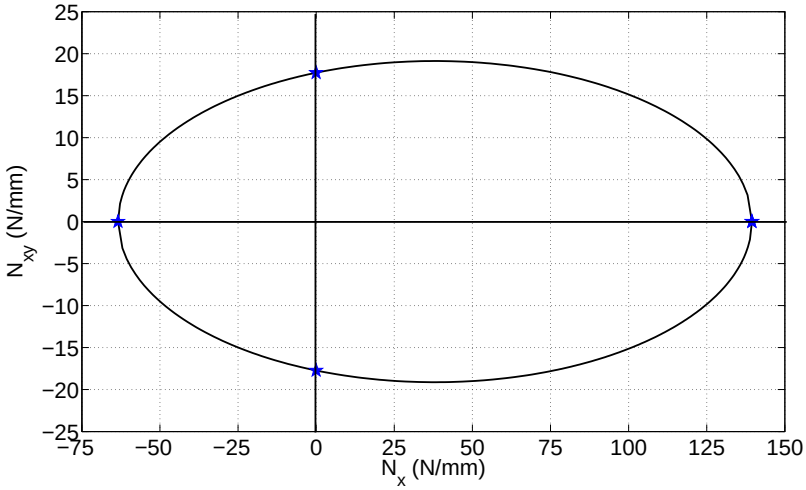

(a) $N_y = 0$

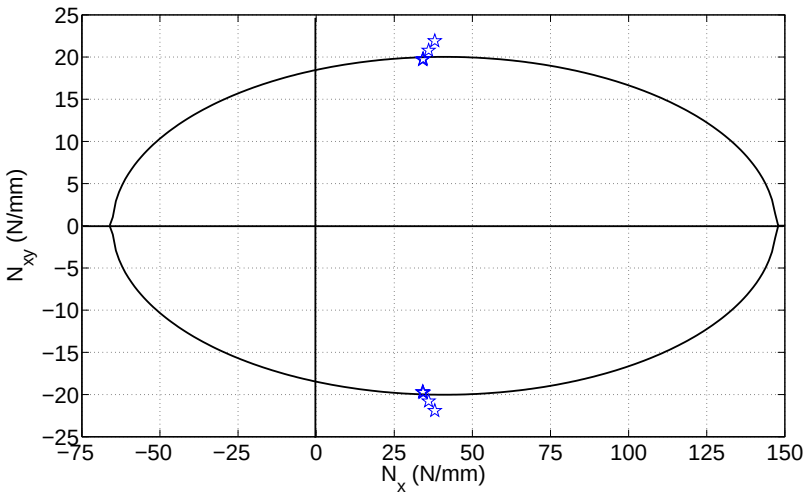

(b) $N_y = 11.77$ N/mm

Figure 6.2: Axial-shear interaction.

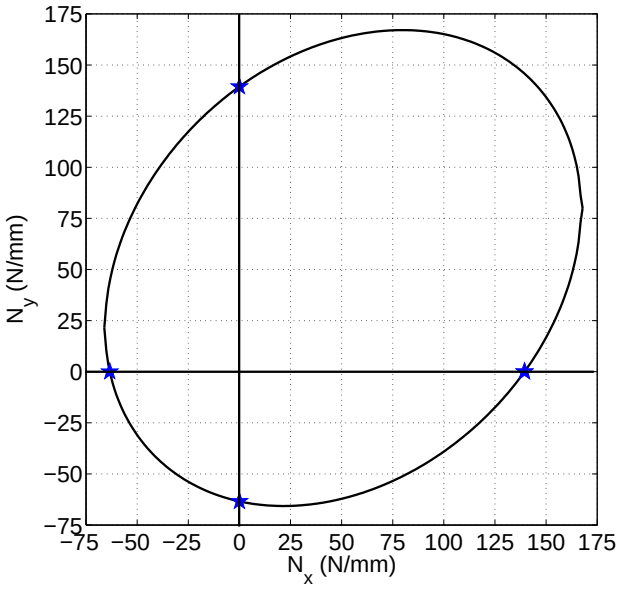

(a) $N_{xy} = 0$

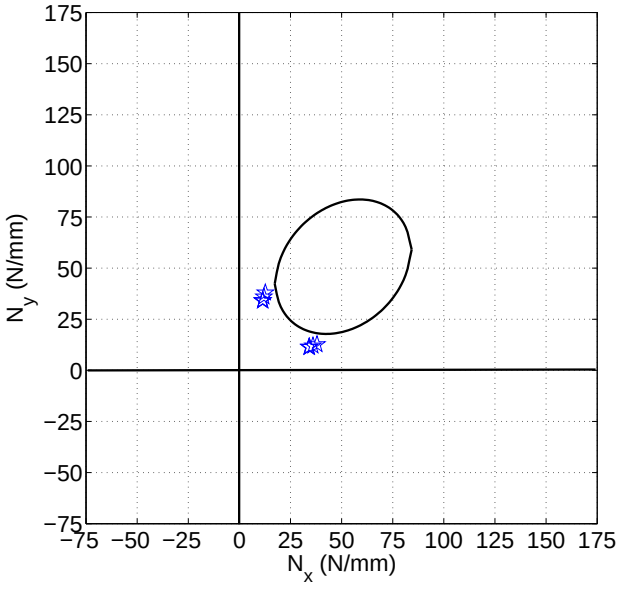

(b) $N_{xy} = 20.38$ N/mm

Figure 6.3: Biaxial failure.

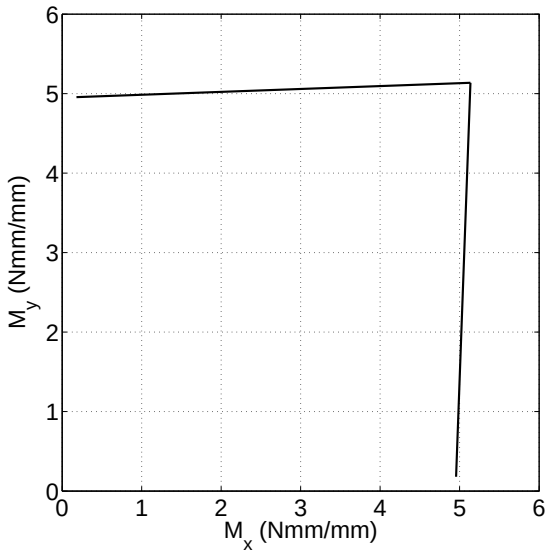

Figure 6.4: Biaxial bending failure locus (constructed from Yee (2006)).

Equation 6.6 defines two cylinders with axes along the M_x and M_y axes, hence all failure points should lie outside of the volume defined by the intersection of these two elliptic cylinders. Figure 6.5 shows a cross-section of the failure locus determined by projecting this values on to the $M_y = 0$ plane. Note that blue and green solid stars represent flat 0/90 and ±45 laminates, respectively. Light blue and purple hollow stars represent ±45 specimens with initial transverse radius of 25.4 mm and 38.1 mm, respectively. Due to the symmetry of the laminate, the M_y vs. M_{xy} locus will look the same.

In conclusion, the failure limits for bending loads can be defined by the following inequalities

$$\hat{f}_{44} M_x^2 + \hat{f}_{66} M_{xy}^2 < 1 \tag{6.7a}$$

$$\hat{f}_{44} M_y^2 + \hat{f}_{66} M_{xy}^2 < 1 \tag{6.7b}$$

6.3.3 In-Plane-Bending Failure

In the case of the tensile tests performed on transversely curved specimens, the failure load was rather close to that for pure tensile strength, Table 4.13. This

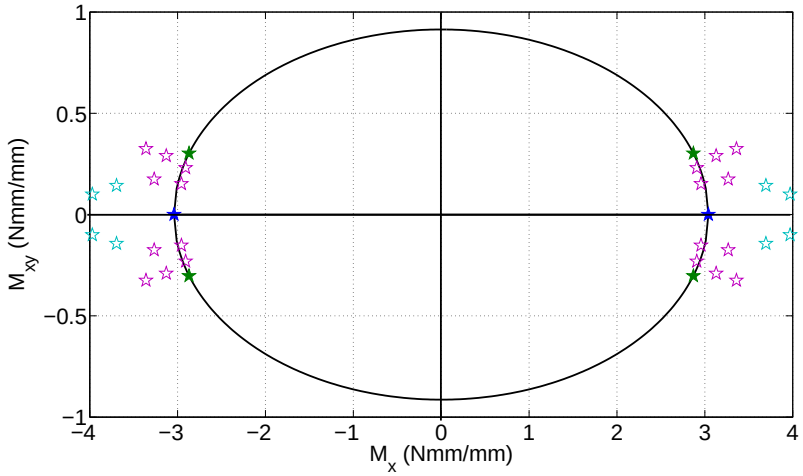

Figure 6.5: Bending-twisting interaction.

shows that axial failure does not depend on a moment applied in the transverse direction. Similarly, Table 4.14 shows that the presence of a twisting moment does not affect the shear strength. Thus it can be concluded that the only interaction to be considered is between in-plane and bending loads applied in the same direction.

From Figure 6.1 it can be concluded that N_x and M_x interact linearly. Due to material symmetry, the interaction between N_y and M_y will be of the same type and hence interactive failure can be expressed by the following inequalities

$$\frac{N_x}{F_x} + \sqrt{\hat{f}_{44}} \times |M_x| < 1 \tag{6.8a}$$

$$\frac{N_y}{F_y} + \sqrt{\hat{f}_{44}} \times |M_y| < 1 \tag{6.8b}$$

where the axial failure strengths F_x and F_y are given by

$$F_x = \frac{-(\hat{f}_1 + \hat{f}_{12}N_y) \pm \sqrt{(\hat{f}_1 + \hat{f}_{12}N_y)^2 - 4\hat{f}_{11}(\hat{f}_1 N_y + \hat{f}_{11}N_y^2 + \hat{f}_{33}N_{xy}^2 - 1)}}{2\hat{f}_{11}} \tag{6.9a}$$

$$F_y = \frac{-(\hat{f}_1 + \hat{f}_{12}N_x) \pm \sqrt{(\hat{f}_1 + \hat{f}_{12}N_x)^2 - 4\hat{f}_{11}(\hat{f}_1 N_x + \hat{f}_{11}N_x^2 + \hat{f}_{33}N_{xy}^2 - 1)}}{2\hat{f}_{11}} \tag{6.9b}$$

Note that Equation 6.9a is obtained by setting $N_x = F_x$ and replacing $<$ with $=$ in Equation 6.4, and then solving the quadratic equation for F_x. Similarly, Equation 6.9b is obtained by setting $N_y = F_y$, etc. and then solving for F_y.

6.3.4 Summary

As described in Section 6.3.3 there is no interaction between axial-twisting, shear-bending and shear-twisting loadings. Also Section 6.3.2 shows that the strength M_x is independent of M_y. Hence the quadratic polynomial assumed in Section 6.2 is not sufficient for failure predictions and it has been shown that a more accurate failure locus is defined from three set of inequalities. In fact this is common in plastic failure of cylindrical shells made of isotropic materials (Calladine, 1972; Hodge Jr., 1954; Sawczuk and Hodge Jr., 1960).

Hence in summary it can be stated that limits on the failure envelope of a two-ply plain weave laminate subjected to force and moment resultants can be defined by

$$\hat{f}_1(N_x + N_y) + \hat{f}_{11}(N_x^2 + N_y^2) + \hat{f}_{12}N_xN_y + \hat{f}_{33}N_{xy}^2 < 1 \tag{6.10a}$$

$$\hat{f}_{44} \times max(M_x^2, M_y^2) + \hat{f}_{66}M_{xy}^2 < 1 \tag{6.10b}$$

$$max(\frac{N_x}{F_x}, \frac{N_y}{F_y}) + \frac{max(|M_x|, |M_y|)}{F_4} < 1 \tag{6.10c}$$

Since it is impossible to visualise a six-dimensional object let us consider a series of three dimensional projections to better understand these three limits.

The in-plane failure envelope is defined by Equation 6.10a, which is an ellipsoid, Figure 6.6. In fact, this is the Tsai-Wu failure criterion given in terms of stress-resultants.

The failure envelope for bending loads is defined by Equation 6.10b. This envelope is defined by the intersection of two cylinders with axes along M_x and M_y, Figure 6.7. Note that when $M_{xy} = 0$ this locus reduces to a square due to the fact that the failure strengths in orthogonal directions (defined with the material directions of the laminate) are independent from each other.

Equation 6.10c defines the interactions between in-plane and bending loads. Fig-

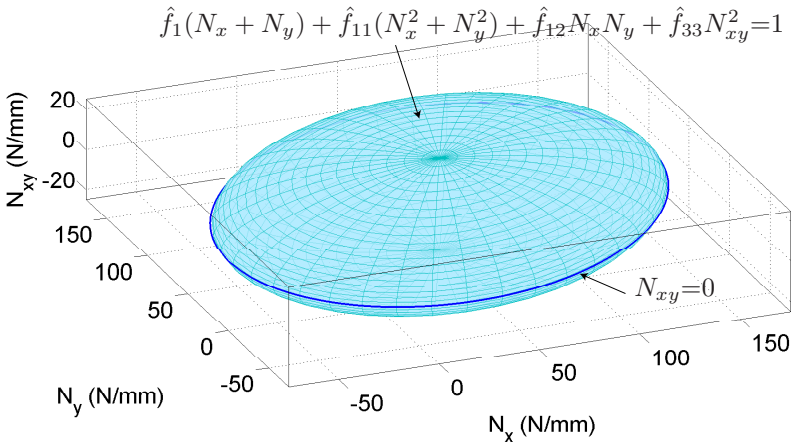

Figure 6.6: In-plane failure envelope.

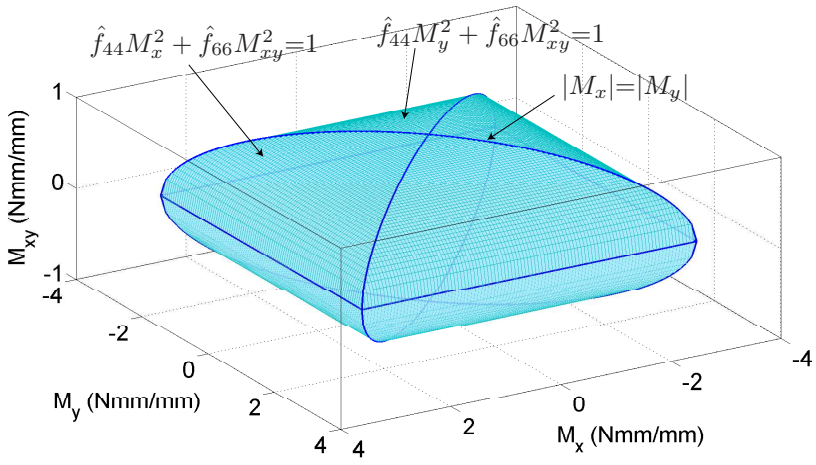

Figure 6.7: Bending failure envelope.

ure 6.8a shows interaction between N_x and N_y with varying M_x. Note that the relationship between axial and bending loads in the same directions is linear but the biaxial in-plane force envelope is an ellipse. Thus the envelope is defined by two cones with a common elliptic base. The interaction between N_x, N_y and M_y has the same shape.

In the case of the interaction between biaxial moments and an in-plane axial load, the failure envelope is given by two prisms defined by linear interactions between an axial force and the moment applied in the same direction but limited by the ultimate bending strength in the orthogonal direction, Figures 6.8b and 6.8c. Note that these two prisms are rotated by 90° about the force axis.

There is no interaction between shear and bending loads; hence the failure locus of N_{xy}, M_x and M_y is a cuboid limited by the shear and bending failure strengths, Figure 6.9a. Similarly, the axial strengths are decoupled from the twisting strength and hence the N_x, N_y, M_{xy} interaction is an elliptic cylinder, Figure 6.9b.

Lastly, the failure interaction between N_{xy}, M_x and M_{xy} is defined by an elliptic cylinder cut at $N_{xy} = |F_3|$, Figure 6.9c. Similarly, the interaction of N_x, N_{xy} and M_{xy} is an elliptic cylinder cut at $M_{xy} = |F_6|$, Figure 6.9d, but this time the axis does not go through the origin due to the difference in tensile and compressive strengths. Figure 6.9e shows the N_x, N_{xy} and M_x envelope.

6.4 Discussion

Three main assumptions were made in developing this failure locus.

- the strength of an initially curved specimen is quite similar to that of a flat specimen, on the micro-level
- the moment required to flatten a curved specimen remains constant up to the point of axial failure
- the ABD stiffness matrix can be used to estimate the transverse moments at failure

The first two assumptions may not be exactly true for specimens with initial curvatures that are themselves close to bending failure. However the tests considered here had comparatively low curvatures, i.e. failure curvature of the laminate is about

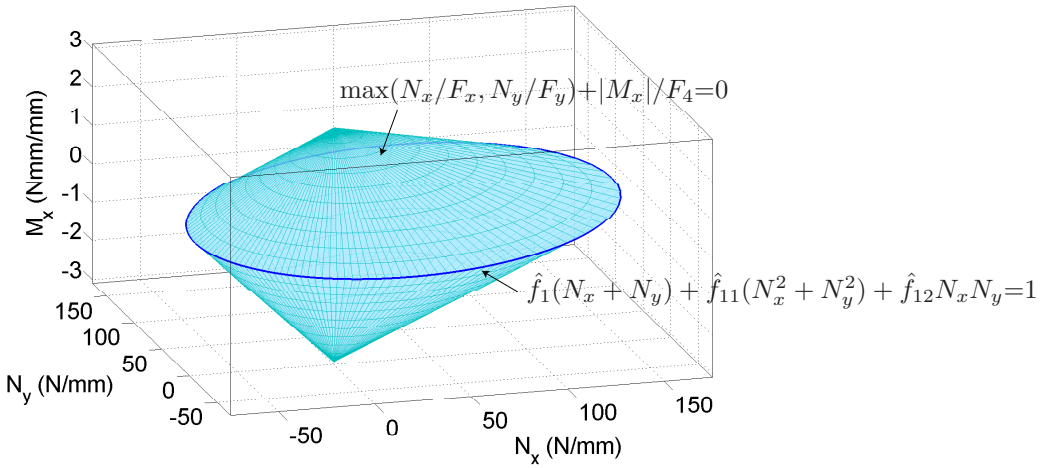

(a) N_x, N_y and M_x

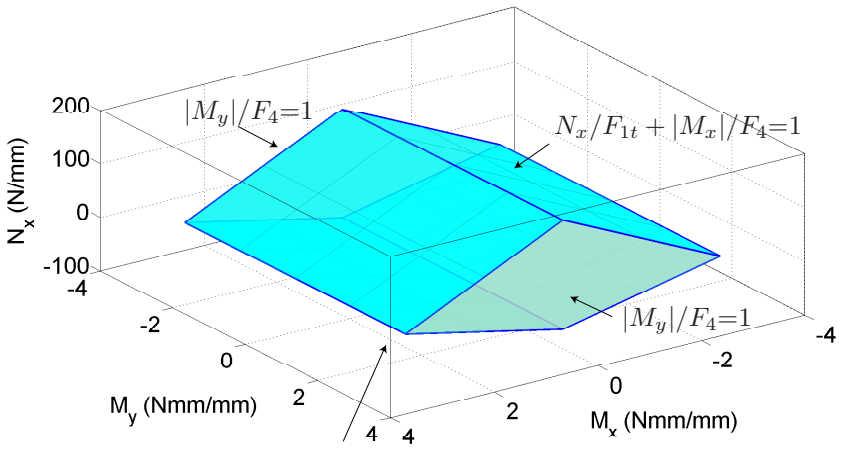

(b) N_x, M_x and M_y

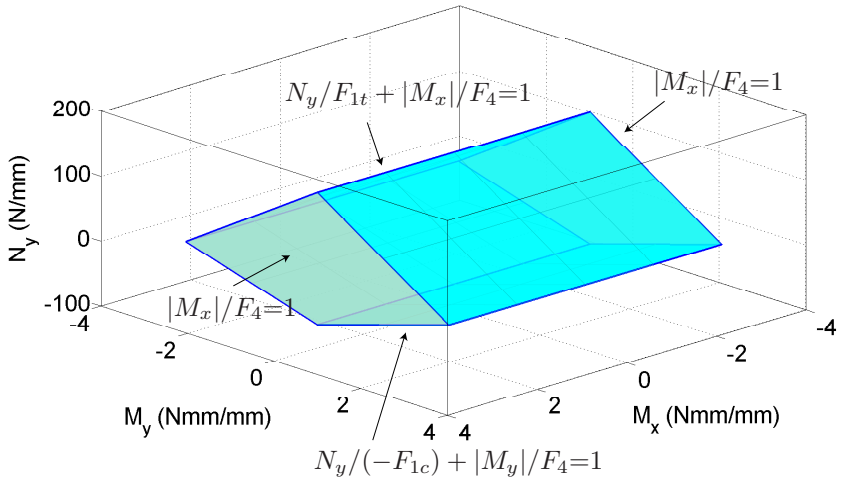

(c) N_y, M_x and M_y

Figure 6.8: Failure interactions between axial forces and bending moments.

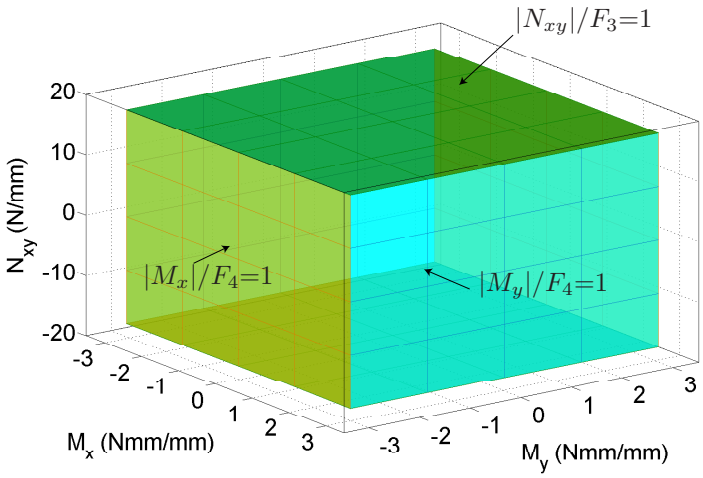

(a) N_{xy}, M_x and M_y

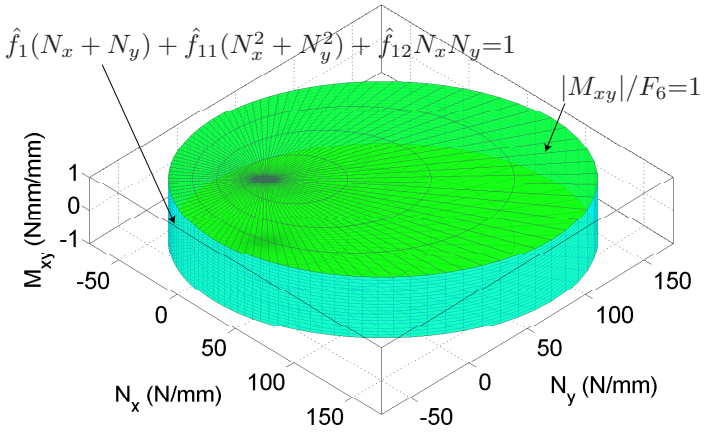

(b) N_x, N_y and M_{xy}

Figure 6.9: Effects of shear force and twisting moment on failure.

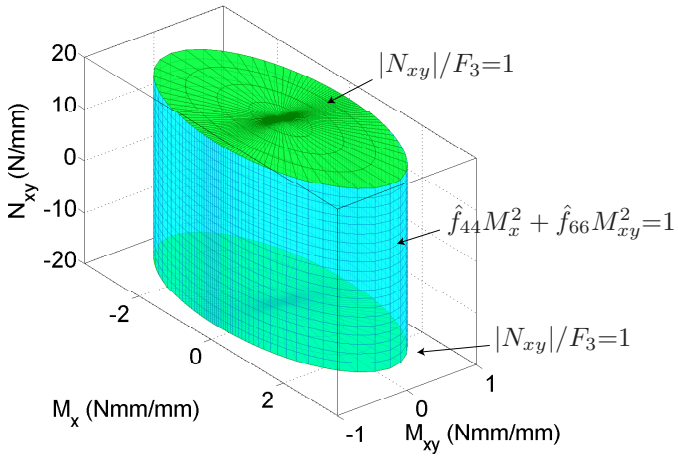

(c) N_{xy}, M_x and M_{xy}

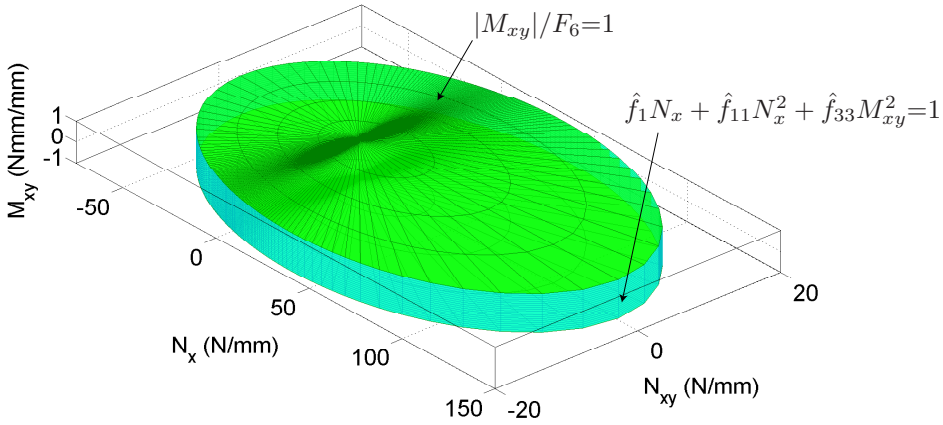

(d) N_x, N_{xy} and M_{xy}

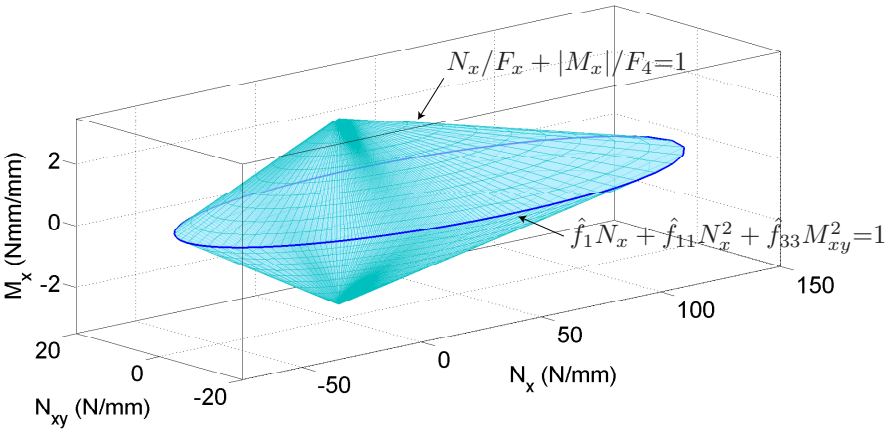

(e) N_x, N_{xy} and M_x

Figure 6.9: Effects of shear force and twisting moment on failure (contd).

0.17 mm^{-1} and the maximum initial curvature reached was 0.052 mm^{-1}. Also it is difficult to perform tensile experiments on specimens having an initial curvature near the bending failure limit.

The experimental setup does not measure the transverse moment of a specimen subjected to longitudinal bending. However both longitudinal and transverse curvatures can be measured. Hence, the transverse moment can be estimated using the ABD stiffness matrix. However the ABD matrix has only been developed for the initial geometry of the laminate. A comparison was made of the measured longitudinal moment with moment estimated using the ABD stiffness matrix and the same stiffness reduction was then used in estimating the transverse moment. This stiffness reduction can be explained by the laminate thickness being reduced, due to the stretching of the tows making them flatten.

In the case of shear and twisting strengths, our experiments did not attempt to achieve conditions of pure shear or twisting. Therefore we have used the proposed failure locus in estimating pure shear and twisting strengths, and additional tests were performed to confirm the accuracy of this approach. The two or three rail shear fixtures cannot be used with this two-ply laminate since it fails by buckling rather than by in-plane shear. One option would be to use thin sandwich specimens similar to those used for the compression tests (Kueh, 2007).

Biaxial bending failure tests were not performed here but instead we made use of the experimental failure curvature locus presented by Yee (2006). Yee used the same carbon fibre fabric impregnated with LTM45 matrix, which provides a similar laminate. This locus was only used to confirm that there is no interaction between longitudinal and transverse bending moments in the case of biaxial bending failure. This result could be due to the fact the ratio D_{12}/D_{11} is quite small and hence has little influence between the two material directions. In the case of axial loading, even though the ratio A_{12}/A_{11} is small the neutral planes are subjected to stretching and hence in-plane longitudinal and transverse loading affects each other.

Figure 6.1 has shown that the failure relationship between axial and bending loads applied in the same direction can approximated to be linear. Therefore Equation 6.8 was developed by defining a linear relation in the ratio between applied load and strength for both force and moment. Since, the axial strength depends on the other two in-plane loads, Equation 6.9 transforms these in-plane failure surfaces, but it should be acknowledged that the experiments were performed with only $N_y = N_{xy} = 0$.

Lastly, failure by delamination was not considered in this research. It is possible that the two-ply laminate may be subjected to delamination. However this was not visible in any of the tests considered for laminate strength measurements or tape-spring hinges.

Chapter 7

Structural Modelling Techniques

This chapter presents the simulation techniques used to compute the structural response of a composite boom with tape-spring hinges. The first part of the chapter gives an introduction to Abaqus/Explicit simulation techniques; various simulation parameters and the checks that are needed to achive an accurate simulation are explained. Techniques for quasi-static folding/deployment simulation of a tape-spring hinge and for selecting suitable simulation parameters through sensitivity studies are explained next. These simulation techniques are then extended to dynamic deployment and the safety of the structure is determined though a failure analysis performed by applying the failure criterion developed in Chapter 6.

7.1 Abaqus/Explicit Simulation Techniques

Folding and deployment simulations of ultra-thin structures involve significant geometric changes that are associated with instabilities, dynamic snaps and extensive contact/sliding between different parts of the structure. In previous studies (Seffen and Pellegrino, 1999; Yee and Pellegrino, 2005a) issues of numerical stability and convergence associated with singularity in the stiffness matrix were the main limit on the range of structural configurations that could be studied and the amount of folding that could be imposed on a given structure. To remove these limitations, an alternative approach that avoids the stiffness matrix has been adopted, which advances the kinematic state of each degree of freedom by direct integration of its equations of motion. This solution is obtained with the Abaqus/Explicit finite element package (Abaqus, 2010).

Three independent techniques were considered to control the analysis: integration time increment, loading rate and numerical damping. Their effects and the limitations that have to be met when one attempts to optimise the related simulation parameters in folding/deployment studies are explained next.

First, the integration time increment should be as large as possible, to reduce the number of increments to complete the simulation. However, explicit time integration is stable only if the Courant condition is satisfied: (Belytschko et al., 2000; Geradin and Rixen, 1994) essentially, the time increment cannot be larger than the time for a wave to travel between adjacent nodes in the finite element mesh. Abaqus/Explicit includes damping effects and estimates the stable time increment limit at each time increment from the approximate relationship Belytschko et al. (2000, chap. 6)

$$\Delta t = \alpha \left(\sqrt{1 + \xi^2} - \xi \right) \frac{l_{min}}{c_d} \tag{7.1}$$

where α, ξ and l_{min} denote time scaling factor, fraction of critical damping in highest frequency mode and the shortest length finite element, respectively. Dilatational wave speed is

$$c_d \approx \sqrt{\frac{E}{\rho}} \tag{7.2}$$

Second, any loads should be applied as smoothly as possible and also the loading rate should be as high as possible, to minimise the number of integration increments required to complete the analysis, provided that the response of the structure remains quasi-static. The smoothness of the load application is achieved with the Abaqus/Explicit command **Amplitude, Definition = Smooth Step*. This prescribes a fifth order polynomial time variation with first and second time derivatives equal to zero at the beginning and end of the time interval. Regarding the overall loading rate, the key question is how short the simulation time can be made without exciting a significant dynamic response. The first mode that would get excited is the fundamental natural mode of the whole structure and, although its frequency and mode shape will change during folding/deployment, it is useful to obtain an approximate estimate at the beginning of the simulation. This can easily be done by an eigenvalue analysis of the structure in its initial configuration.

Third, numerical damping is introduced in the model to dissipate energy build-up at high frequencies, to avoid the sudden collapse of elements due to large out-balance

forces that may develop at a few nodes, and to generally keep down the amount of kinetic energy in the structure. The amount of numerical damping should be as small as possible, to avoid affecting the results of the simulation. This is particularly critical for ultra-thin structures whose low bending stiffness could easily be swamped by damping effects, and also avoid decreasing the stable time increment (note that in Equation 7.1 Δt decreases when ξ is increased).

Abaqus/Explicit allows inclusion of damping in several different ways, of which two —bulk viscosity and viscous pressure— are utilised; these two particular types of damping are explained next.

The first type of damping, bulk viscosity introduces an in-plane strain-rate dependent pressure

$$p_b = \xi \rho c_d l \dot{\epsilon}_v \tag{7.3}$$

and an in-plane curvature-rate dependent moment

$$m = \xi \frac{h^2}{12} \rho c_d l \dot{\kappa} \tag{7.4}$$

both distributed over all shell elements.

The second type of damping, viscous pressure, introduces a velocity-dependent normal pressure over all shell elements

$$p = - \, c_v \boldsymbol{v} \cdot \boldsymbol{n} \tag{7.5}$$

This normal pressure is very effective in quickly damping out dynamic effects and thus reach quasi-static equilibrium in a minimal number of increments. However, it is important to use an appropriate value of c_v; if it is too high the response of the structure will be overdamped and hence the simulation results may be incorrect. Note that, unlike bulk viscosity, viscous pressure does not change the integration time increment.

There is an alternative technique, mass scaling, that is often used to speed up explicit analyses. This technique consists in artificially increasing the density of the material to $\beta\rho$, in order to increase the time increment from Equation 7.1 to $\sqrt{\beta}\Delta t$. This technique would be useful in simulations involving rate-dependent materials, where the load-rate speed-up technique adopted in the present study could not be used, but offers no advantages in the quasi-static work performed here. However,

Abaqus provides a variable mass scaling technique where the user is allowed to define a specific time increment and then Abaqus automatically scale the mass of required elements to satisfiy Equation 7.1.

The key test for the robustness of a particular analysis is to consider the history of the various energy terms and in particular the energy balance history. The energy balance, E_b, is defined as the difference between the energy stored in the structure and/or dissipated during the loading process, $E_i + E_v + E_k$, and the work of all external forces, E_w. In symbols:

$$E_b = E_i + E_v + E_k - E_w \tag{7.6}$$

where the internal energy E_i is equal to the sum of strain energy and artificial energy (due to hourglassing), E_v is the viscous dissipation, E_k is the kinetic energy. In the present simulations the artificial energy was kept negligibly small by using fully integrated elements and by avoiding any localised actions on the shells.

There are two main checks on the energies. First, at any particular time the kinetic energy has to be a small fraction ($< 1\%$) of the internal energy for the results at that time to be considered a valid quasi-static solution. In the case of multi-stable structures if the kinetic energy has reached high levels during an earlier part of the simulation, the possibility that the structure may have reached an alternative equilibrium configuration should be considered. Second, the energy balance should remain equal to the amount of external energy (e.g., thermal) introduced in the system.

In particular, Belytschko et al. (2000) discuss cases where an "arrested instability" in a structure, due to geometric and/or material softening, may result in the integrator losing stability, despite the use of Equation 7.1 to compute the time increment. These authors have reported that all such instabilities can be detected by checking the energy balance, as discussed above.

7.2 Tape-Spring Hinge Finite Element Model

Figure 7.1 shows the finite element model of a tape-spring hinge used to simulate a quasi-static folding and deployment sequence. To simulate the deployment behaviour one needs to compute first the folded configuration of the hinge and this requires that two cross-sections of the tape-spring hinge be rotated in opposite di-

rections until the fully-folded configuration is reached.

The tape-spring hinge model consists of 2546 nodes and 2412 shell elements (S4) with a minimum element length of around 3 mm.

The elastic properties of the shell elements were defined in a cylindrical coordinate system (with directions x', y', z respectively longitudinal, circumferential and radial) by assigning the $ABD^{\pm 45}$ matrix of Equation 5.17 with the **Shell General Section* parameter.

In order to simulate the equal end moment conditions of a pure bending test, two reference nodes A and B were attached to a dummy node, C, using the Abaqus command **Equation* and these reference nodes were rigidly attached to the nearest eight nodes of the holders. The sensitivity studies in Section 7.3.1 were done with the reference nodes attached to a single node.

The boundary conditions, see Figure 7.1, are defined as follows: all degrees of freedom at node A are restrained, except the rotation about the global X-axis. Node B is only allowed to translate along the global Z-axis and rotate about the X-axis. To keep the end moments equal, the rotational degrees of freedom of nodes A and B are restrained by prescribing the condition

$$\theta_X^A - \theta_X^B = \theta_X^C \tag{7.7}$$

where θ_X denotes a rotation about the global X-axis.

To simulate the folding process the folding angle θ_X^C was incremented from 0° to 170° (or in some cases only 160°) over a suitably chosen time interval; details are provided in Section 7.3.

The tape-spring hinge has to be pinched before one starts to rotate the ends. This process is simulated by defining two rigid plates connected by a single beam element which undergoes thermal contraction. The plates are restrained to the Y-Z plane, to maintain symmetry. The connections between the beam element and the rigid plates are modeled as fixed using CONN3D2 elements and *Weld* connector sections.

The definition of several contact surfaces is also required, as different parts of the tape-spring hinge come into contact with each other and also the rigid plates come into contact with the tape-spring hinge. The *General Contact* feature is assigned to the entire model by specifying *Contact Inclusions, All Exterior*. With this option Abaqus/Explicit automatically defines potential contact surfaces around the

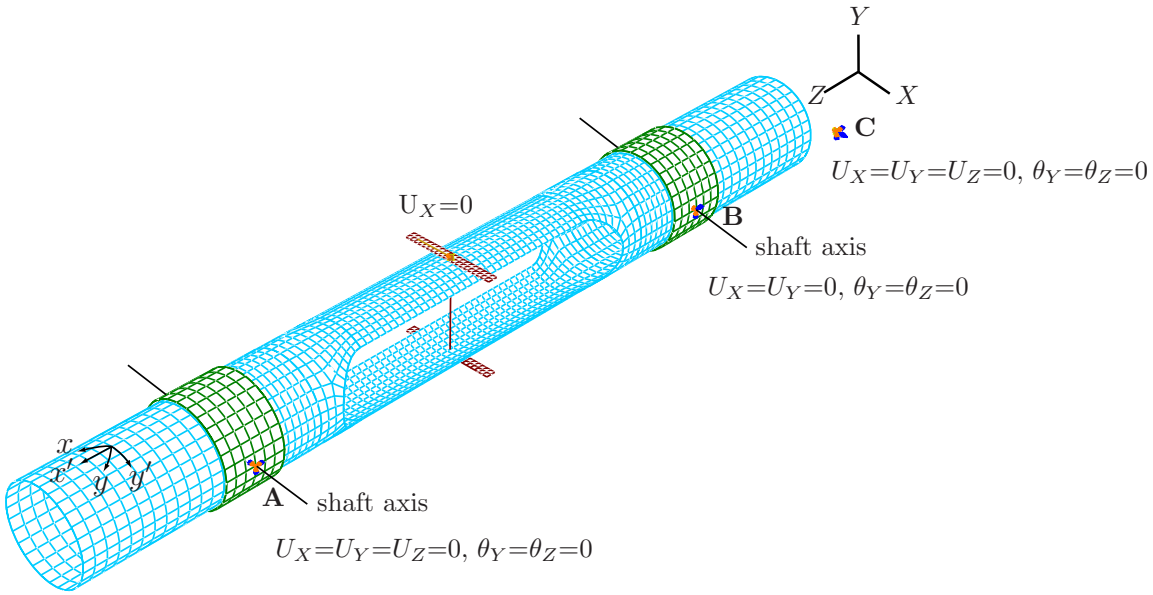

Figure 7.1: Finite element model of tape-spring hinge.

whole hinge surface. However, the beam element connecting the two plates used for pinching is allowed to go through the hinge by using the *Contact Exclusions* parameter.

7.3 Quasi-Static Folding and Deployment

The fundamental natural period of vibration of the tape-spring hinge in the deployed configuration was computed by doing a frequency analysis in Abaqus/Standard. The estimated period was 5 ms, hence the definition of the overall loading rate was initially set such that folding/deployment would occur over a time period of ten times the fundamental period, or 0.05 s. The entire simulation was run with the double precision solver and the energy components were recorded at every millisecond. The ratio between kinetic energy and internal energy was then monitored and the loading rate was decreased until $E_k/E_i < 1\%$.

An example of a successful simulation is presented next, to provide a basis for discussion and as a starting point for various sensitivity studies.

The initial, unstressed configuration of the tape-spring hinge is shown in Figure 7.2a. At the beginning of the folding simulation the thermally controlled beam element connecting the two rigid plates was shortened by decreasing its temperature,

which simulated the pinching of the tape-spring hinge and led to the configuration in Figure 7.2b. The next part of the folding simulation consisted in imposing a rotation $\theta_X^C = 170°$ over 0.8 s (this simulation time was obtained by gradually increasing the initial value of 0.05 s estimated above). After 0.25 s, corresponding to $\theta_X^C \approx 16°$, see Figure 7.2c, contact between the rigid plates and the tape-spring hinge was disabled in order to avoid any spurious constraints on the folded shape. The rotation was then continued and the final outcome is shown in Figure 7.2d. Viscous pressure loading, discussed in Section 7.1, was used to maintain the energy ratio below 1%.

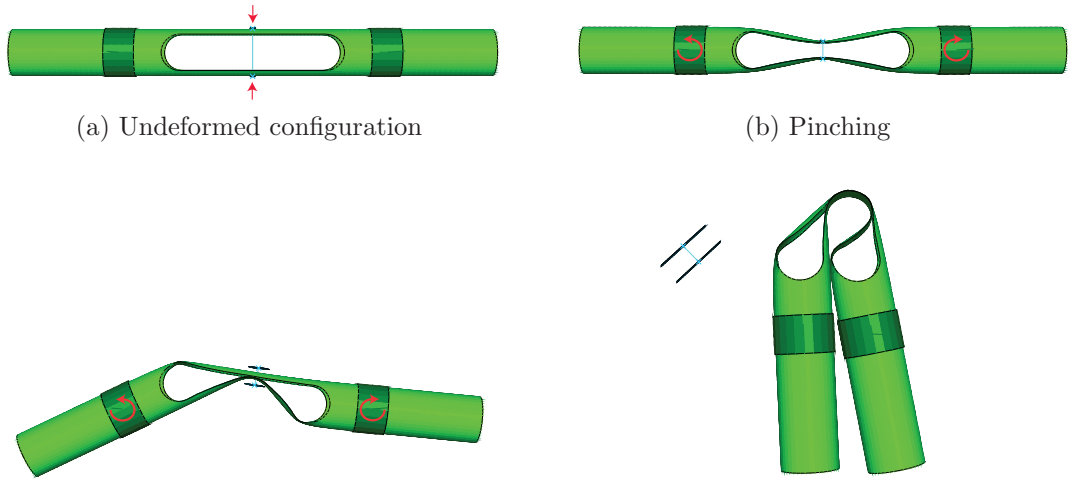

(a) Undeformed configuration

(b) Pinching

(c) Release of contact between hinge and rigid plates

(d) Final folded configuration

Figure 7.2: Stages of folding simulation.

Figure 7.3 shows the variation of the energy terms during this simulation. Note that during the pinching phase there is an input of thermal energy that is not accounted for in Equation 7.6 and this shows as an increase in energy balance. For the rest of the simulation the energy balance remained approximately constant. Throughout the simulation the kinetic energy remained much smaller than the internal energy, which indicates that the intended quasi-static behaviour of the tape-spring hinge has been achieved.

7.3.1 Setting the Simulation Parameters

This section presents various sensitivity studies to determine a set of simulation parameters that provide accurate results and maximal speed up of the simulation. These studies were mainly focused on the deployment part of the simulation because

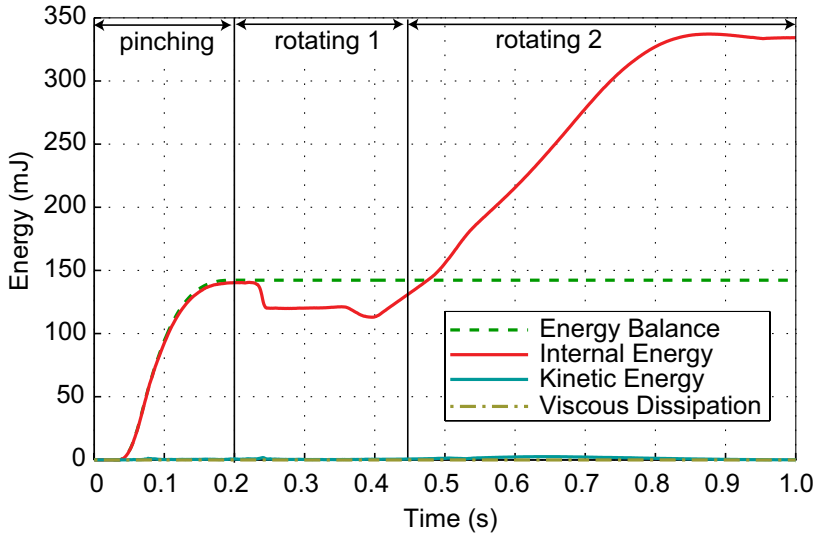

Figure 7.3: Energy histories for folding simulation with $\alpha = 0.8$, $\xi = 0$, $c_v = 2\times\ 10^{-4}\rho c_d$; the maximum folding angle is θ_X^C=170°.

this is the behaviour that is of greatest interest for actual applications. However, it was important to first obtain an accurate representation of the folded configuration and hence two different folding simulations were carried out.

The first folding simulation used no bulk viscosity ($\xi = 0$) but only viscous pressure on the outer surface of the tape-spring hinge during the rotational phase; the expression for the pressure is given by Equation 7.5 with $c_v = 2\times10^{-4}\rho c_d$. The time increment factor in Equation 7.1 was set to $\alpha = 0.8$. The results have already been presented in Figure 7.3. Note that the viscous dissipation is zero because the energy absorbed by the viscous pressure is included in the external work. The energy balance remained constant during the rotation phase which indicates that the simulation was free of instabilities and hence the results are accurate. The kinetic energy was negligibly small at the end of the simulation, indicating that the folded configuration is in quasi-static equilibrium.

The second folding simulation used bulk viscosity ($\xi = 0.10$, but $c_v = 0$) to provide numerical damping. The energy histories are presented in Figure 7.4; note the high level of viscous dissipation, representing 70% of the internal energy at the end of the folding phase. Between 1.0 s and 1.1 s viscous pressure was applied (with $c_v = 2\times10^{-2}\rho c_d$) to decrease the kinetic energy. Reducing the time increment by setting α to less than 1.0 made little difference to these results.

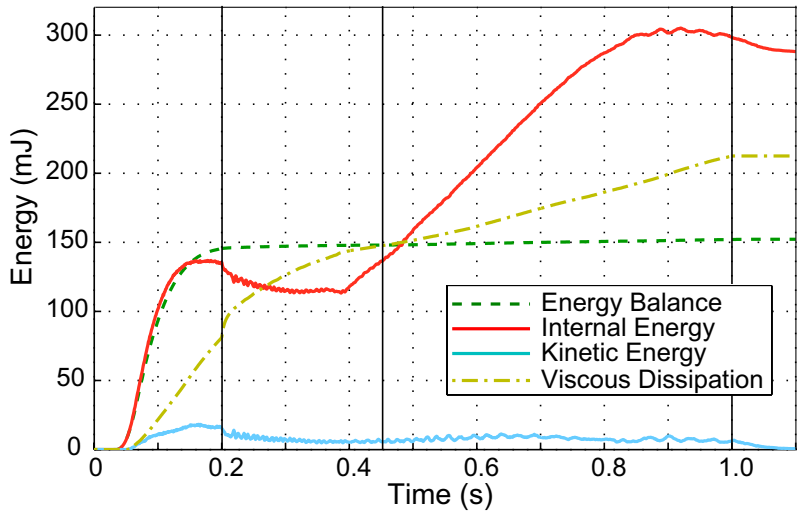

Figure 7.4: Energy histories for folding simulation with $\alpha = 0.8$, $\xi = 0.10$, $c_v = 0$ up to 1.0 s and then $c_v = \times 10^{-2} \rho c_d$.

The final configurations predicted by these two folding simulations are approximately equal, but the first simulation was chosen as a starting point for the deployment studies because it has lower kinetic energy and a smoother moment-rotation relationship.

A folded configuration with $\theta_X^C = 160°$ (to avoid the effects of the contact between the ends of the tape-spring hinge) and $\alpha = 0.5$, $\xi = 0$, $c_v = 2 \times 10^{-4} \rho c_d$ was chosen as the starting point for several deployment simulations with different values of the three control parameters.

The sensitivity to α was examined by setting $\alpha = (0.25,\ 0.80)$ with $\xi = 0$ and $c_v = 0$. Figure 7.5 shows that in this case decreasing Δt decreases the change in energy balance.

The sensitivity to ξ was examined by setting $\xi = (0,\ 0.01,\ 0.10)$. Figure 7.5 shows that increasing ξ leads to a decrease of the change in energy balance. Although increasing ξ leads to a small reduction in Δt, and hence to an increase in the number of simulation increments, it is much more effective in decreasing the energy balance than lowering α.

Despite this encouraging result, one should be cautious before relying on bulk viscosity to reduce the energy balance. The problem is that increasing ξ may prevent full deployment. Figure 7.6 shows the history of the viscous dissipation energy for

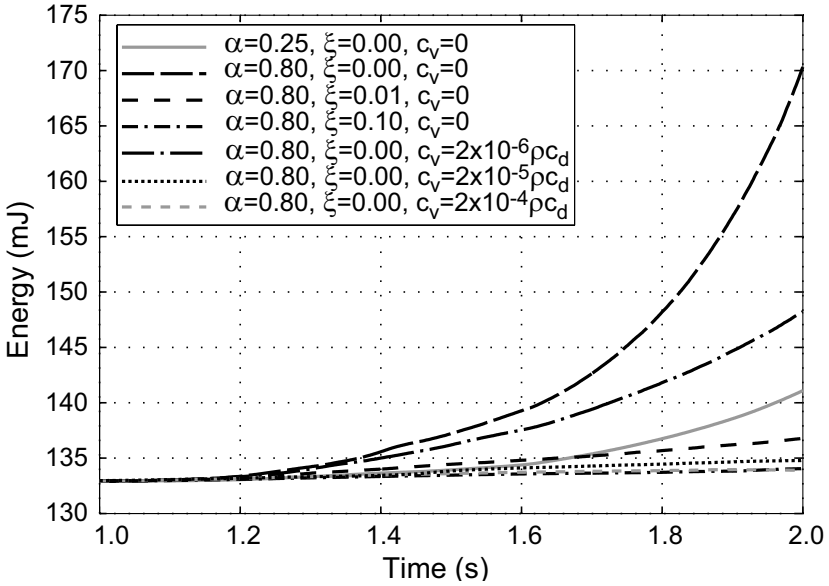

Figure 7.5: Energy balance histories for different values of α, ξ, c_v.

the three cases that have been considered. It is interesting to note that the viscous dissipation during deployment is 13% and 17% of the internal energy in the fully folded configuration, respectively for $\xi = 0.01$ and $\xi = 0.10$.

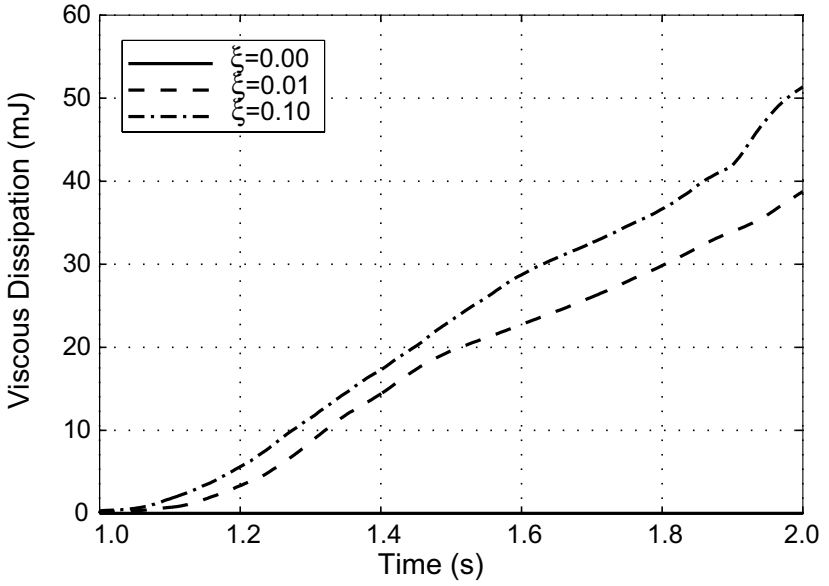

Figure 7.6: Variation of viscous dissipation for $\alpha = 0.80$, $c_v = 0$.

A feature common to the above simulations, in which bulk viscosity was introduced without viscous pressure, is that there was significant vibration, leading to a noisy moment-rotation deployment profile. This issue was addressed by examining the sensitivity to c_v. Four different values of c_v were considered, from 0 to $2 \times 10^{-4}\rho c_d$, while maintaining $\alpha = 0.8$ and $\xi = 0$ and the results are shown in Figure 7.5 and Figure 7.7. Figure 7.5 shows that the higher values of c_v are effective in decreasing the change in energy balance. Figure 7.7 shows that the particular value $c_v = 2{\times}10^{-5}\rho c_d$ suppresses most tape-spring hinge vibration from $\theta_X^C = 160°$ to about 50°. However, increasing c_v by another order of magnitude radically changes the behaviour of the structure.

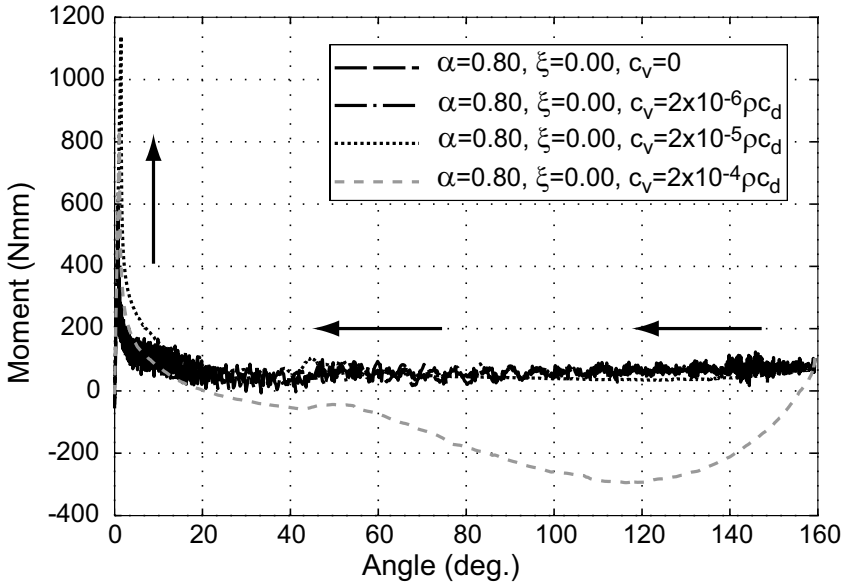

Figure 7.7: Sensitivity of moment-rotation response to c_v, for α=0.8 and ξ=0. The line style matches Figure 7.5.

In conclusion, the viscous pressure coefficient c_v is the most effective tool for keeping the change in energy balance small, but it is important to examine the effects of c_v on the structural response in order to avoid overdamping. Based on the study presented in this section, it was decided that the parameters $\alpha = 0.8$, $\xi = 0$, $c_v = 2{\times}10^{-5}\rho c_d$ are best for deployment simulations of this particular hinge.

Once optimal deployment simulation parameters had been obtained, the overall simulation time was increased from 1 s to 3 s and Figure 7.8 shows the energy history for this final simulation. Note that this particular simulation started from a folded

configuration with $\theta_X^C = 170°$. These results are of very good quality, as the energy balance remains constant throughout the simulation, and show a sudden reduction in internal energy at 3.77 s, accompanied by a small spike in kinetic energy. These features correspond to the dynamic snap back of the hinge into its fully deployed configuration. This jump releases practically all the internal energy in the hinge.

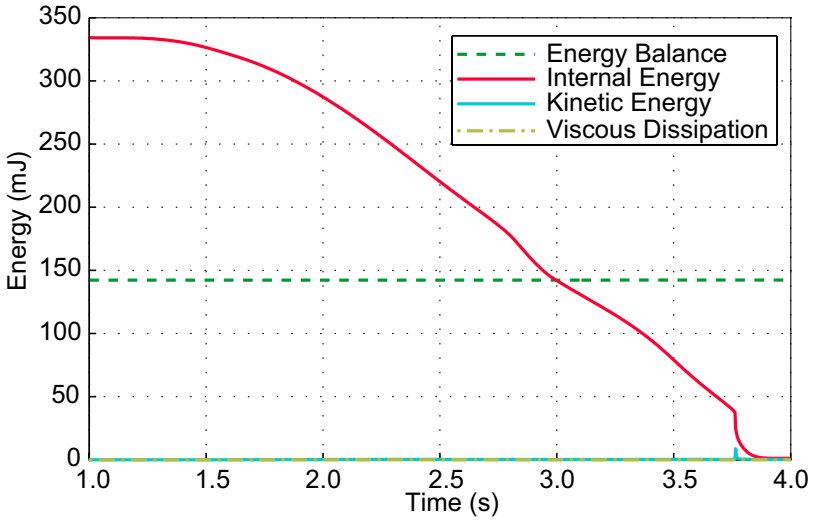

Figure 7.8: Energy histories for 3 s deployment with α=0.8, ξ=0, c_v=$2\times10^{-5}\rho c_d$.

7.4 Dynamic Deployment

Understanding the dynamic deployment behaviour for a self-deployable structure is important. Unlike quasi-static deployment, dynamic deployment will be largely affected by structural components attached to the considered hinge. As an example, the same tape-spring hinge has been connected to an aluminium-alloy tube to form a 1 m long boom with a fixed end connection, Figure 7.9. Due to the use of two different materials and the mass of the connections, their mass distribution over the structure has the values provided in Table 7.1.

The finite element model is similar to that presented in Section 7.3 apart from the equal moment constraints (Mallikarachchi and Pellegrino, 2009a). In order to start the deployment the initial folded configuration has to be determined first, however, because the detailed sequence that leads to this configuration is less important than the final folded configuration itself, provided that the kinetic energy in the

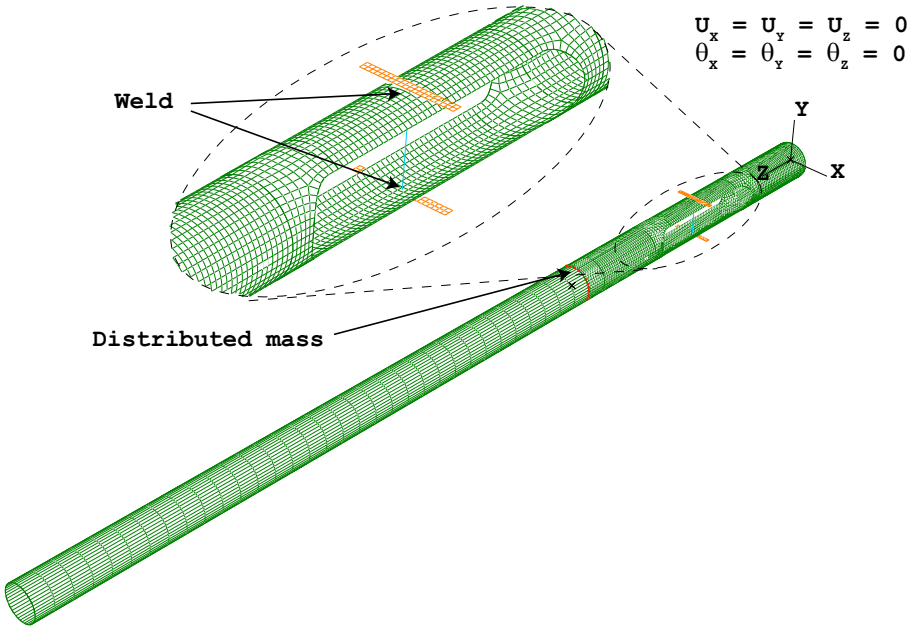

Figure 7.9: Finite element model of considered boom for dynamic simulations.

Region	Mass distribution
$0 < z < 322.5$ mm	318 g/m^2
$z = 322.5$ mm	25.79 g
$322.5 < z < 1000$ mm	2400 g/m^2

Table 7.1: Mass distribution of finite element model for dynamic simulation.

folded configuration is sufficiently small and the energy balance term remains constant during folding, to ensure that the final result is correct. Figure 7.10a shows energy variation corresponding to a 45° folded configuration obtained with the same simulation parameters obtained for the quasi-static folding simulation. However, this is a much larger structure and it has been folded as fast as possible to minimise the computational effort. A 100 times larger viscous pressure, varying over 0.2 s was applied to quickly achieve the fully-folded, static configuration (balancing step in Figure 7.10a). Note the that kinetic energy is quite high during folding but negligible at the end of the simulation and energy balance term is constant throughout.

Deployment is triggered by releasing all constraints used for folding. Unlike the folding simulation, where the simulation time had no physical meaning but was simply chosen such that the kinetic energy would never be too high, in the deployment analysis the simulation time is the actual time over which the motion occurs. Also mass scaling cannot be used here because now the inertia forces are significant.

One need to be careful in using viscous pressure as it tends to damp out the dynamic response. Following a similar parametric study it was found that use of ξ = 0.1 and/or application of $c_v = 2{\times}10^{-5}\rho c_d$ to the hinge region only was successful in eliminating artificial high frequency oscillations in the hinge. Figure 7.10b shows the energy variation for dynamic deployment of this hinge, determined by applying only $\xi = 0.1$. Note that the energy balance term remains constant, which guarantees that the simulation is free of instabilities.

7.5 Failure Analysis

A failure analysis was performed by applying the failure criterion presented in Section 6.3.4 to the stress-resultants obtained from the finite element simulations. Three failure indices, FI-1, FI-2 and FI-3, were defined by evaluating the left hand sides of Equations 6.10a, 6.10b and 6.10c, respectively, and their values were calculated at every integration point and averaged over each element, at every step of the simulation. These three indices are useful to understand the dominant loading condition at each point and, to satisfy the failure criterion, all three values should be less than 1.

Since all simulations used the initial ABD matrix, which is overestimated by approximately 40% of failure strength, see Section 4.3.5, the bending and twist-

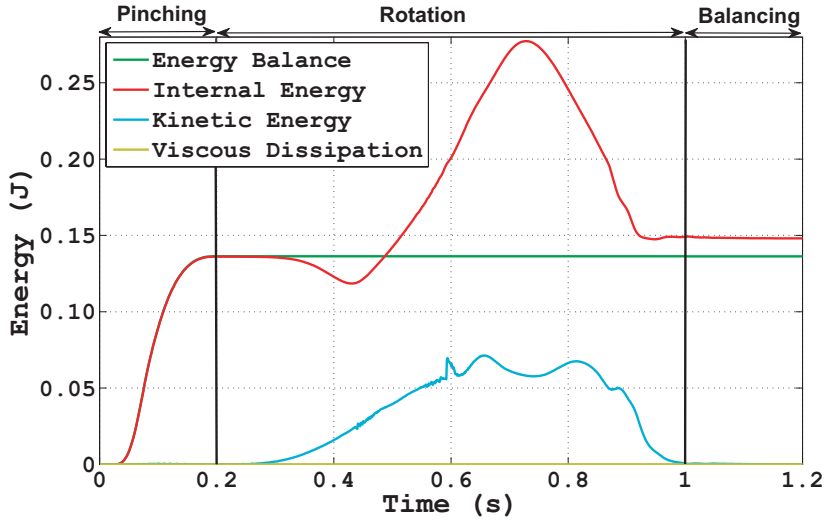

(a) Folding simulation

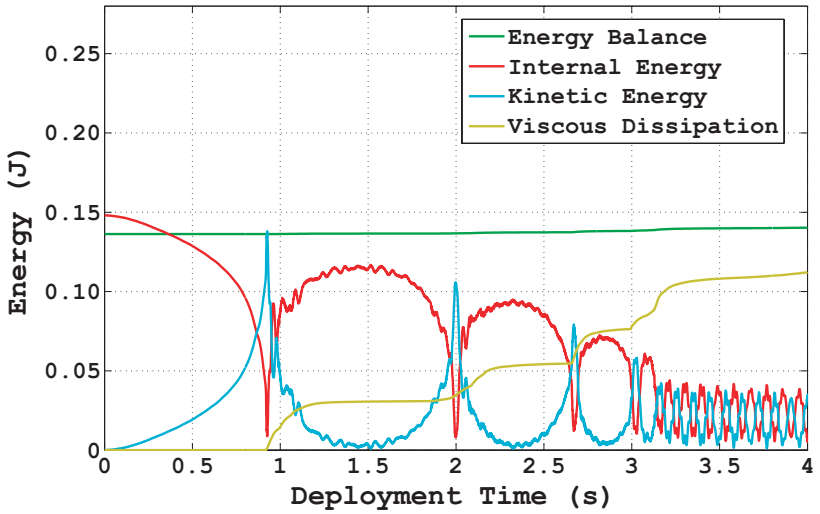

(b) Deployment simulation

Figure 7.10: Energy variation for dynamic deployment simulation with initial folding angle of 45°.

ing moments near failure will also be overestimated by 40%. To correct for this in an approximate way both bending and twisting strengths are multiplied by a factor of 1.67 when analyzing the stress resultants from the simulations. Hence, the increased bending and twisting strengths are $F_4'' = F_5'' = 5.07$ Nmm/mm and $F_6'' = 1.53$ Nmm/mm.

The tensile and compressive responses are almost linear up to failure and hence no modifications of the corresponding strengths are made.

A complete failure analysis of a particular boom design consists of two parts. Firstly, the boom should be safely foldable to the required folding angle and, secondly, it needs to withstand the dynamic loads during deployment. Therefore, the failure analysis during deployment has to calculate the failure indices throughout the entire deployment simulation and then consider their maximum values.

The critical configuration of the particular tape-spring hinge design discussed so far is the fully folded configuration. Figure 7.11 shows contours of the three failure indices in the fully folded configuration of the particular tape-spring hinge. Note that all three indices are below 1 and hence the hinge can be safely folded to 180°. Also note that, because FI-3 is the largest of the three, this particular hinge design is more sensitive to interaction between in-plane and bending loads.

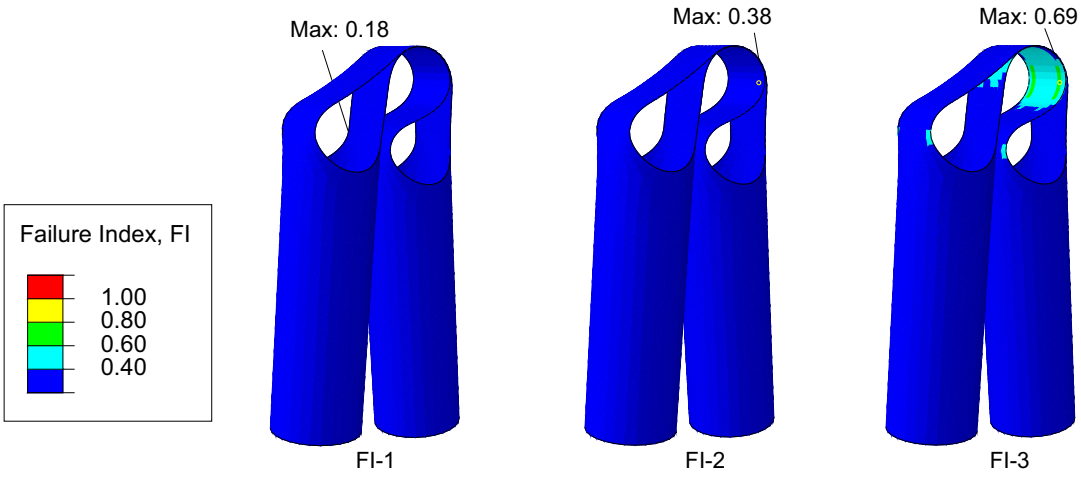

Figure 7.11: Failure indices at fully folded configuration.

Chapter 8

Simulation Results

This chapter presents a detailed study of the tape-spring hinge design considered in Chapter 7. The quasi-static folding and deployment behaviour is characterised in terms of the moment-rotation response of the tape-spring hinge. The dynamic deployment behaviour is characterised in terms of the angle-time response of the tape-spring hinge and it is shown that changes in the boundary conditions or even slight changes in the initial conditions lead to a different angle-time response for the considered hinge design.

8.1 Quasi-Static Simulation

The moment-rotation response of the tape-spring hinge described earlier can be studied through quasi-static simulations. Here the rotation angle is defined as the angle formed by the two centre lines of the tube regions on either side of the hinge.

The folding simulations techniques described in Section 7.3 had assumed that folding would begin by pinching the hinge; this was done because in practice the tape-spring hinge may break if it is folded without pinching first. However, to obtain a better understanding of the complete behaviour of the hinge, a complete simulation of the process of folding and deployment is carried out, but this time without initiating the folding process by pinching. The total simulation time was 6 s: 3 s to fold and 3 s to deploy. The simulation parameters were $\alpha = 0.8$, $\xi = 0$ and $c_v = 2 \times 10^{-5} \rho c_d$.

The energy histories have been plotted in Figure 8.1. The energy balance remained approximately constant throughout the simulation and hence the results

are accurate. Note that the internal energy profile is mostly symmetric but shows a spike during folding, at 0.32 s, that is not matched by a corresponding spike during deployment. In fact, during the initial stages of folding the strain energy increases at a considerably faster rate than it decreases during the corresponding stages of deployment. An important result is that the internal energy becomes approximately zero at the end of the deployment simulation, indicating that the unstressed, fully deployed configuration has been achieved. Note the kinetic energy spike at 0.32 s and the smaller spike at 5.76 s; they correspond to the hinge snapping during folding and snapping back, respectively. The viscous dissipation was, of course, zero throughout the entire simulation.

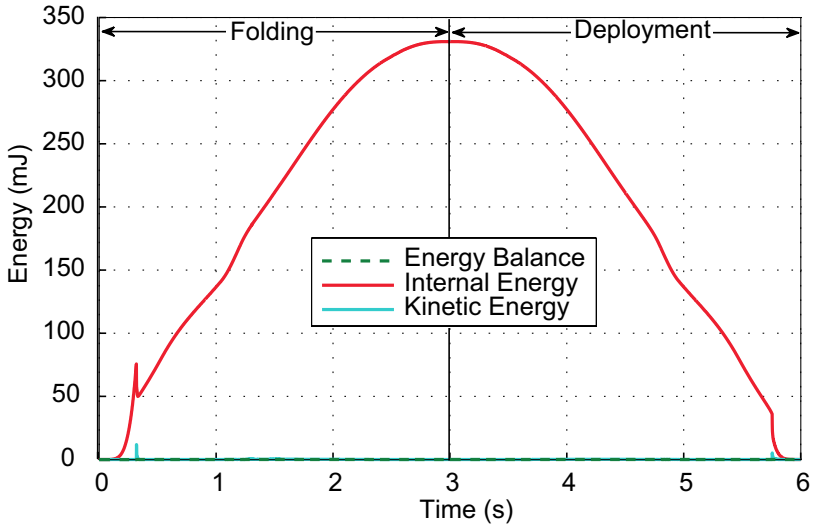

Figure 8.1: Energy histories for simulation of folding to $\theta_X^C = 170°$ without pinching and deployment.

Next, turning to the moment-rotation profile, shown in Figure 8.2, the most striking features are that the moment rises to a high peak of 4278 Nmm, snaps to about 67 Nmm and remains almost constant from an angle of approximately 20° all the way to the fully folded configuration. Note that there is a slight hump between 40° and 60°, associated with the snap back of the elastic fold at the centre of the outer tape-spring and an increase beyond 170° when a contact pressure develops between the two ends of the hinge. During deployment, the moment-rotation profile follows the folding profile down to 1.8°, then continues to rise gradually, with a final snap back to 2482 Nmm at 0.8°. It then joins the linear part of the folding response as the angle is further decreased.

This difference between the loading and unloading paths is characteristic of structures with an unstable post-buckling equilibrium path (Brush and Almroth, 1975; van der Heijden, 2009). It was already known that a single tape spring behaves in this way (Seffen and Pellegrino, 1999; Warren et al., 2005), but having established that the post-buckling behaviour of tape-spring hinges is also unstable is an interesting result with important implications.

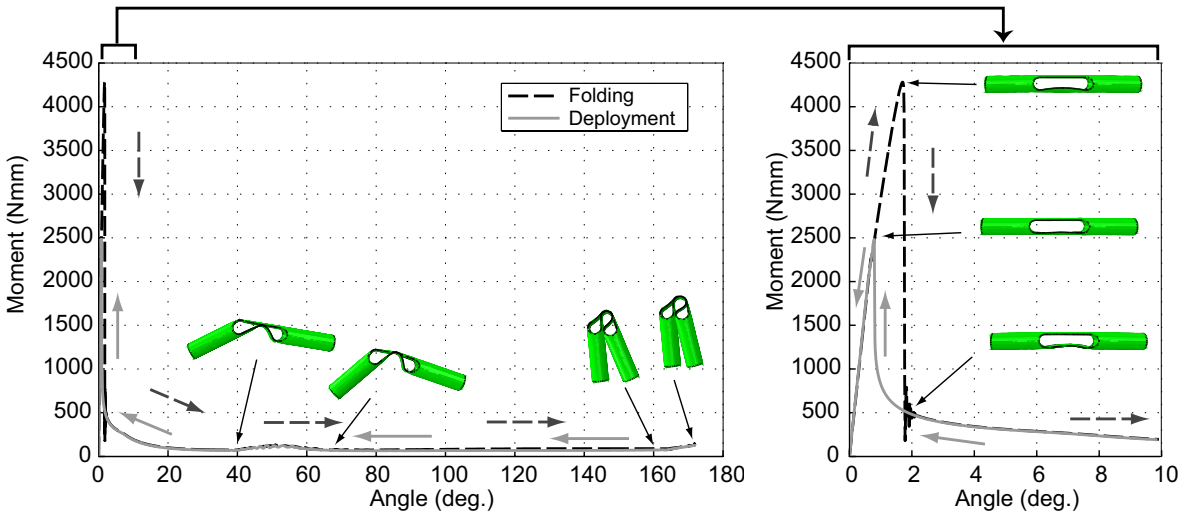

Figure 8.2: Moment-rotation profile for folding and deployment simulation (without pinching) up to θ_X^C=170°.

In practice this type of structure cannot be safely folded without pinching. A failure analysis shows that the hinge will fail during the folding peak as the failure indices FI-2 and FI-3 exceed 1, Figure 8.3a. This explains that when folding without pinching, the material near the circular part of the slots is subject to high bending moments.

The failure analysis also confirms that a safely folded hinge does not fail during the deployment snap, Figure 8.3b.

8.2 Dynamic Deployment Simulation

A plot of the angle-time response is useful to understand the dynamic deployment behaviour of a tape-spring hinge. This provides an understanding of the motion of the boom as well as whether it can safely latch.

A simulation carried out of the dynamic deployment of a 45° folded boom showed

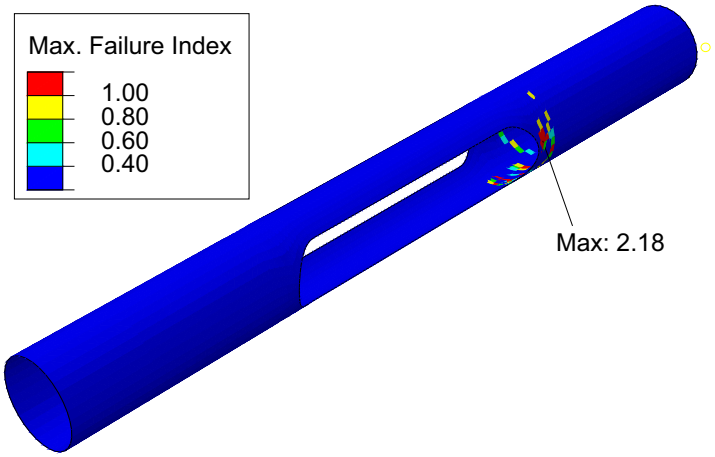

(a) During folding

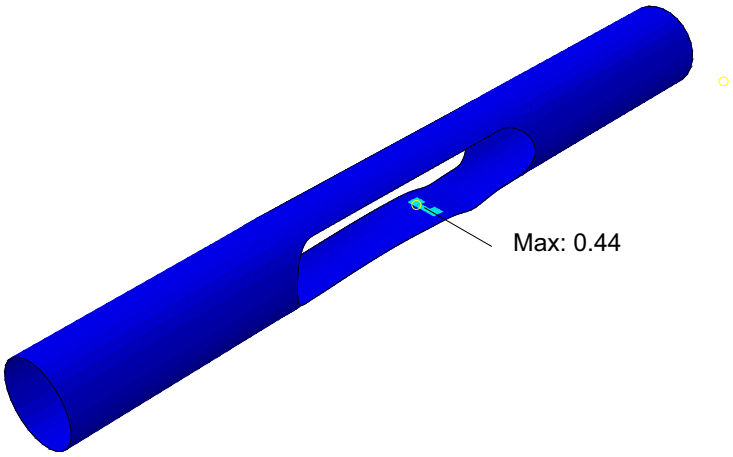

(b) During deployment

Figure 8.3: Failure analysis near folding and deployment load peaks.

that the deployment behaviour consists of three phases, Figure 8.4, as already observed experimentally by Yee (2006) (see Figure 2.13).

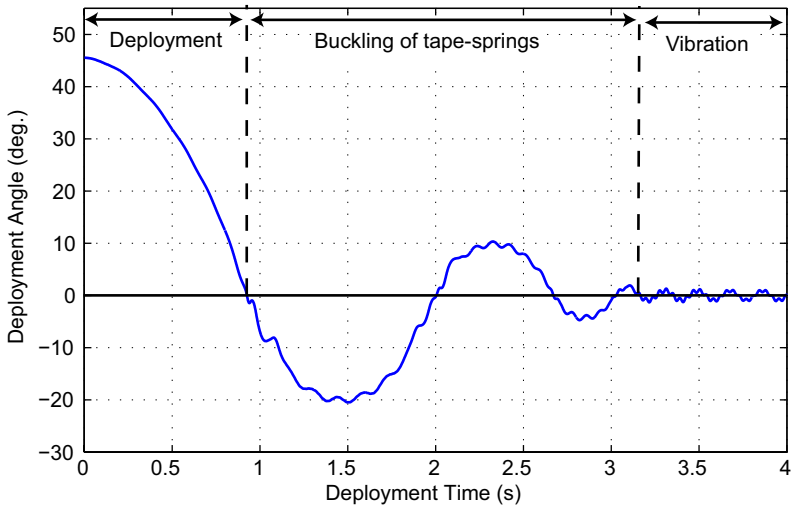

Figure 8.4: Angle-time response for boom initially folded 45°.

8.2.1 Sensitivity to Boundary Conditions

As the next step, the sensitivity of the angle-time response of a tape-spring hinge to the boundary conditions applied in the analysis was investigated. The main focus of the sensitivity study was to use the infinite elements available in Abaqus/Explicit to model a soft boundary condition. Abaqus provides first- and second-order infinite elements that are based on the work of Lysmer and Kuhlemeyer (1969) for dynamic response. The elements are used in conjunction with standard finite elements, which model the area around the region of interest, with the infinite elements modeling the far-field region. During a dynamic analysis infinite element acts as a dashpot which provides a distributed damping on the boundary (Abaqus, 2010).

The infinite elements considered here cannot be directly connected to the shell elements used to model the structure. Hence, the fixed end of the boom was connected to a single layer of elastic solid elements through the "shell to solid" coupling feature. Then the elastic solid elements were attached to the infinite elements. Four different boundary conditions were studied, Figure 8.5, and all these simulations were carried out with $\xi = 0.10$, $c_v = 0$ and $\alpha = 0.80$.

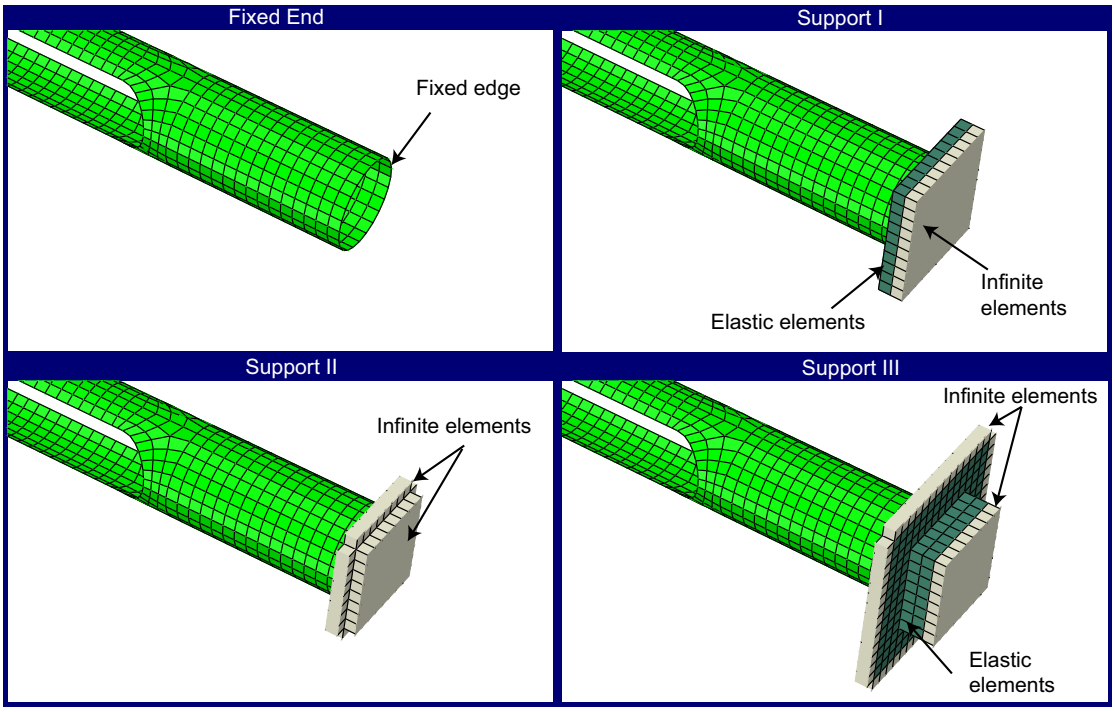

Figure 8.5: Different boundary conditions with infinite elements.

It should be noted that the use of infinite elements allows a rigid body rotation of the entire structure. Hence the angle-time response was obtained with respect to the root of the boom. Note that there is a significant change in angle-time response, Figure 8.6, depending on which type of support is used in the analysis.

8.2.2 Effect of Changes in Initial Conditions

Figure 8.7a compares the angle-time variation for two deployment simulations started after a single folding simulation of a 90° fold. In the first case the folding restraints were released during the balancing step and in the second case they were relaxed at the end of balancing step. This introduces a slight change in the kinetic energy at the beginning of the deployment phase, which was 0.08 mJ and 0.02 mJ for condition I and II, respectively. This small change in initial conditions leads to a rather large change in the overshoot angle during the phase of buckling of the tape-springs. In fact, the reason for this difference is due to a change in position of the localised fold in the tape-spring hinge, Figure 8.7b.

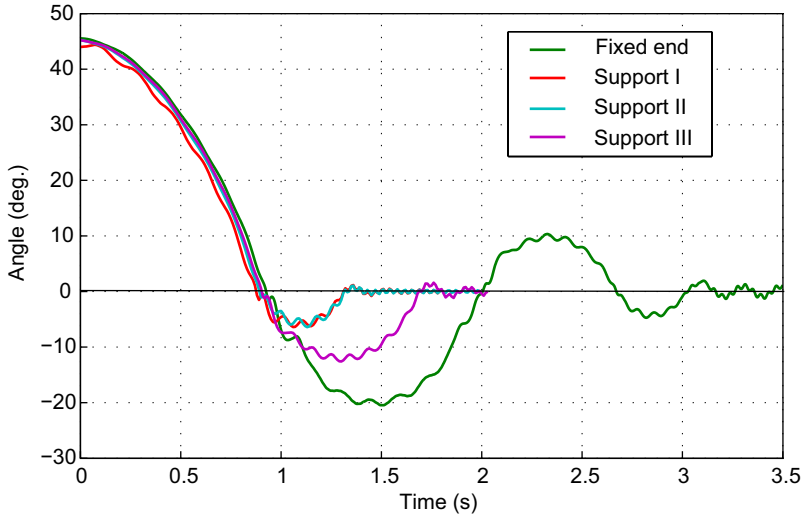

Figure 8.6: Angle-time response for boundary conditions shown in Figure 8.5.

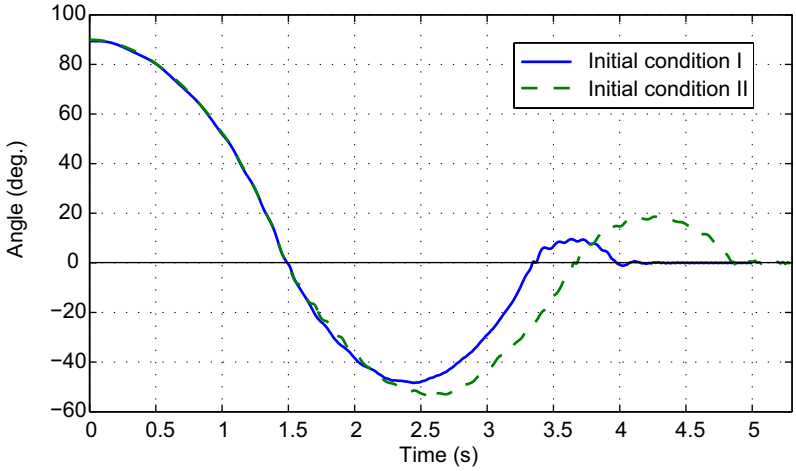

(a) Angle-time variation

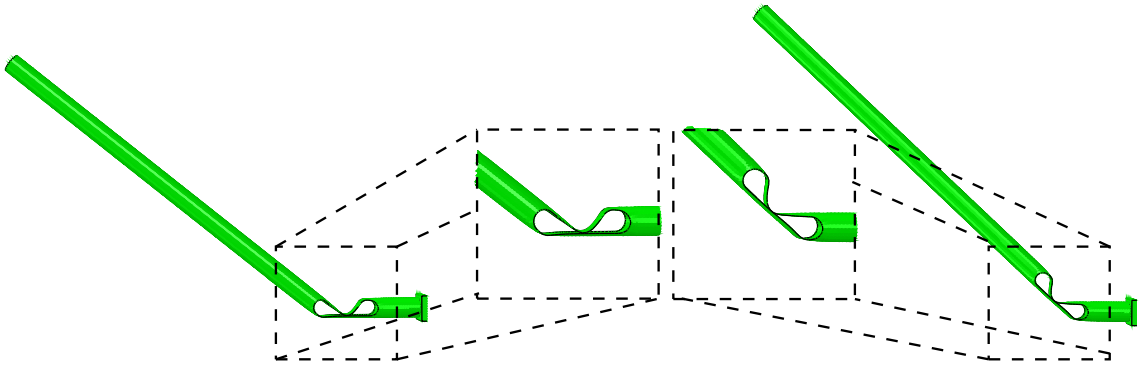

Initial condition I Initial condition II

(b) Deformed configuration at maximum overshoot

Figure 8.7: Deployment dynamic simulations with slightly different releasing conditions.

Chapter 9

Design of Tape-Spring Hinges and Tubular Booms

This chapter describes the procedure to design multiple-hinge booms. The first part of the chapter focuses on the geometric optimisation of a single tape-spring hinge that can be folded to 180° with minimum material removal. The second part of the chapter describes the design of a 1 m long two-hinge boom that can be folded around a spacecraft and will self-deploy without any overshoot.

9.1 Optimisation of Hinge Geometry

Chapter 8 showed that in the hinge design considered so far, and shown in Figure 8.7, the fold region in each tape spring could be freely moved along the length of the tape-spring, suggesting that the length of the tape springs could possibly be shortened. Since there would be definite advantages in a more compact hinge design where a smaller amount of material is removed and so the slots are shorter and/or narrower, the basic configuration shown in Figure 9.1 is chosen and the effect of varying three parameters; the slot length, L, the slot width, SW, and the diameter of the end circles, D, is explored. These three parameters define the dimensions of a solid that extrudes the slot from a cylindrical tube (preliminary versions of this work were presented in Mallikarachchi and Pellegrino (2009b) and Mallikarachchi and Pellegrino (2010)).

Initial values for the three parameters, $L = 60$ mm, $SW = 10$ mm and $D = 15$ mm, were chosen based on the Astro Aerospace FFT, which however is made from dif-

ferent materials. The target here is to obtain a tape-spring hinge that can be safely folded 180°, and which requires only a minimum amount of material to be removed from the initial tube.

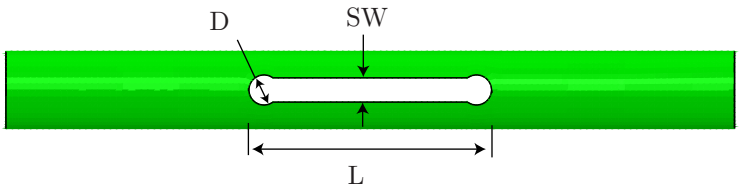

Figure 9.1: General hinge geometry chosen for optimisation study.

9.1.1 Sensitivity to Mesh Refinement

When looking at the strain distributions obtained from a simulation it is important to check that the finite element mesh is sufficiently fine. Therefore this particular hinge was modeled with four different meshes, described below.

- Mesh I : approximate element length of 3 mm, Figure 9.2a (2464 nodes and 2380 elements).
- Mesh II : approximate element length of 2 mm, Figure 9.2b (4898 nodes and 4780 elements).
- Mesh III : approximate element length of 2 mm with smaller elements near the end circles of the slots, Figure 9.2c (5456 nodes and 5304 elements).
- Mesh IV : approximate element length of 1 mm, Figure 9.2d (19758 nodes and 18036 elements).

Table 9.1 shows the maximum mid-surface strains ε_x, ε_y and ε_{xy} and the maximum curvatures κ_x, κ_y and κ_{xy} in the fully folded configuration, for each mesh. Here the subscripts x and y refer to the fibre directions defined in Figure 7.1. The analysis time listed in the last column of the table is for a 2.4 GHz Intel Core2 Quad CPU Q6600 processor machine. It should be noted that in the simulations the command **Fixed Mass Scaling, dt=1e-06, type=below min* (Abaqus, 2010) was used to artificially scale up the mass of small elements, to increase the critical time increment to 1 μs, Equation 7.1. Mesh type III is chosen for further studies, because it provides sufficient accuracy at a low computational cost.

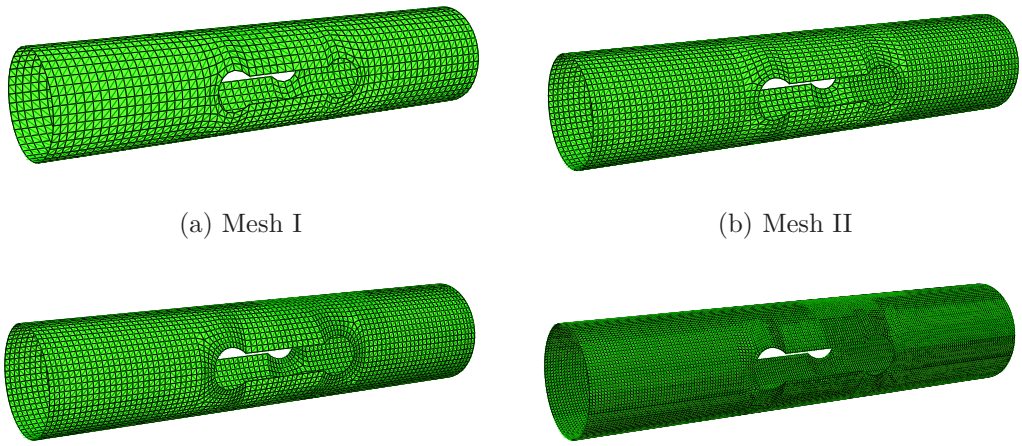

(a) Mesh I

(b) Mesh II

(c) Mesh III

(d) Mesh IV

Figure 9.2: Mesh refinement study ($SW = 10$ mm, $D = 15$ mm and $L = 60$ mm).

Mesh	ε_x (%)	ε_y (%)	ε_{xy} (%)	κ_x (1/mm)	κ_y (1/mm)	κ_{xy} (1/mm)	Analysis Time (h:min)
I	1.33	1.25	-1.78	0.159	0.154	-0.110	2:56
II	0.44	0.48	0.50	0.163	0.163	-0.109	5:36
III	0.51	0.45	0.51	0.186	0.186	-0.116	6:08
IV	0.47	0.48	0.59	0.189	0.185	-0.114	19:40

Table 9.1: Maximum mid-surface strains and curvatures for different mesh sizes.

9.1.2 End Conditions

The ability of these more compact tape-spring hinges to survive the deformation imposed by the folding process highly depends on the ovalisation of the end cross-sections. Figure 9.3 shows significant differences in the mid-plane strain contours of a hinge folded to 180°, depending on the end conditions provided in the analysis. Note that the mid-plain strains cannot exceed 1.5% for T300 fibres. Thus the focus here is to use a hinge design where the end sections are allowed to deform.

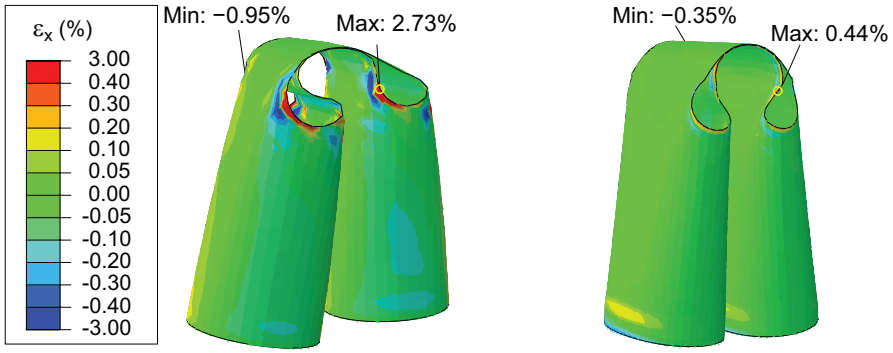

(a) Restrained cross-sections (b) Free to deform

Figure 9.3: Distribution of ε_x in the fully folded configuration with different boundary conditions ($SW = 10$ mm, $D = 15$ mm and $L = 60$ mm).

9.1.3 Sensitivity to Slot Length

The sensitivity to L is first examined near $L = 60$ mm by exploring the range 45 mm to 90 mm at 5 mm intervals while maintaining $SW = 10$ mm and $D = 15$ mm. Figures 9.4a-9.4d show the failure indices contours for a few selected cases. Only FI-3 is shown for clarity. Note that the most critical region is always near the slot edges. Table 9.2 presents the maximum values of all three failure indices obtained for each case. Note that in all cases FI-1 remains less than 50%. Thus the failure is bending and in-plane-bending dominated.

9.1.4 Sensitivity to Slot Width and End Circle Diameter

The next attempt was to investigate the sensitivity to SW and D to obtain a safe geometry. Based on the results of Section 9.1.3 $L = 60$ mm and $L = 90$ mm were selected for further investigation.

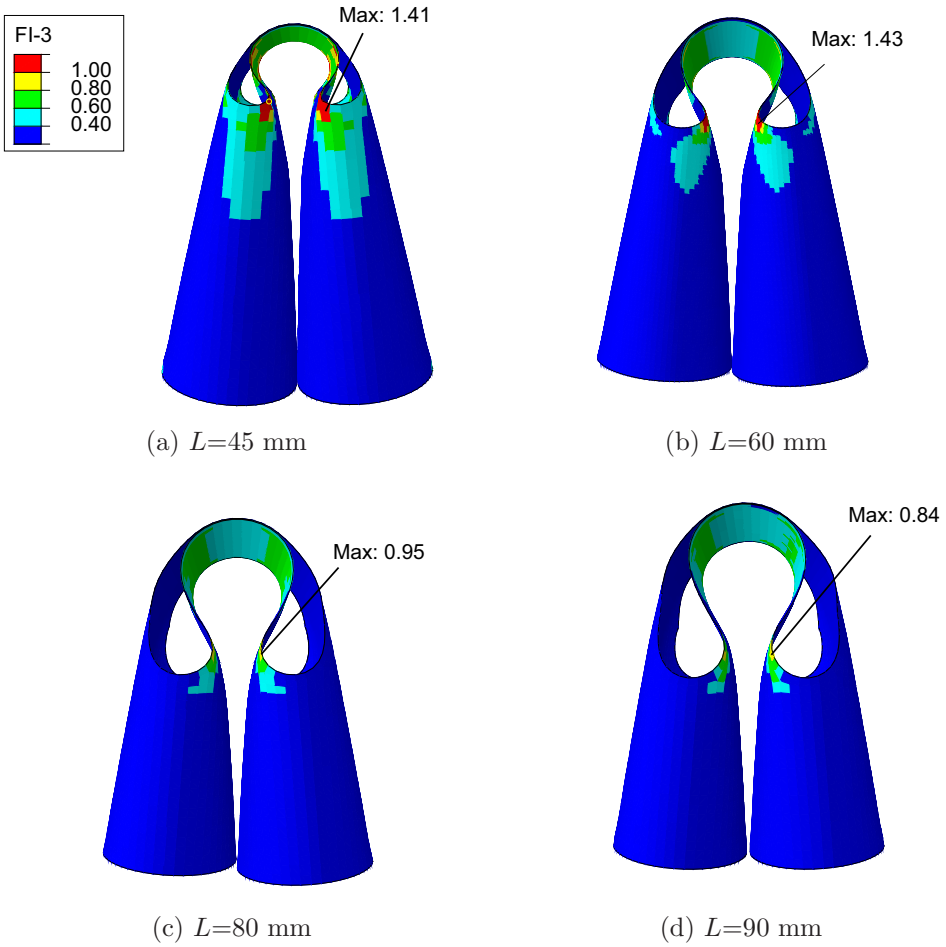

(a) L=45 mm (b) L=60 mm

(c) L=80 mm (d) L=90 mm

Figure 9.4: Distribution of FI-3 in fully folded configuration with varying L (SW = 10 mm and D = 15 mm).

Design			FI-1	FI-2	FI-3
L (mm)	SW (mm)	D (mm)			
45	10	15	0.48	2.19	1.41
50	10	15	0.19	2.06	1.38
55	10	15	0.17	1.60	1.25
60	10	15	0.19	1.81	1.43
65	10	15	0.20	1.20	1.16
75	10	15	0.28	0.98	1.00
80	10	15	0.31	0.82	0.95
85	10	15	0.32	0.65	0.84
90	10	15	0.32	0.59	0.84

Table 9.2: Failure Indices for different designs with varying L.

9.1.4.1 Sensitivity of designs with $L = 60$ mm

First D was set to 15 mm and SW was varied from 8 mm to 12 mm in steps of 2 mm. Table 9.3 presents the corresponding failure indices. Note that in all three cases FI-2 and FI-3 exceed the failure limits.

SW (mm)	FI-1	FI-2	FI-3
8	0.15	1.45	1.19
10	0.19	1.81	1.43
12	0.17	1.38	1.17

Table 9.3: Failure indices for varying SW ($D = 15$ mm and $L = 60$ mm).

The sensitivity to D was studied by varying D from 13 mm to 17 mm while keeping SW fixed to 10 mm, Table 9.4. Similar to previous cases, both FI-2 and FI-3 still exceed the failure limits. It is thus concluded that varying SW or D does not improve the design with $L = 60$ mm and so a different value of L needs to be considered.

D (mm)	FI-1	FI-2	FI-3
13	0.22	1.50	1.23
15	0.19	1.81	1.43
17	0.17	1.38	1.15

Table 9.4: Failure indices for varying D ($SW = 10$ mm and $L = 60$ mm).

9.1.4.2 Sensitivity of designs with $L = 90$ mm

Section 9.1.3 has shown that the design with $L = 90$ mm, $SW = 10$ mm and $D = 15$ mm can be folded safely. To obtain a design with a better safety margin, the sensitivity to SW and D was investigated by varying SW from 8 mm to 12 mm while maintaining the ratio SW/D at either 1/2, 2/3 or 1. Table 9.5 presents the three failure indices obtained for each design. There is no significant improvement and so it is concluded that the design with $SW = D = 12$ mm provides the lowest margin. However in practice it is difficult to manufacture a perfect transition between the straight and circular parts of the slots. Thus considering the minimum slot size design with $SW = 8$ mm and $D = 15$ mm is selected.

Design				FI-1	FI-2	FI-3
L (mm)	SW (mm)	D (mm)	$\approx SW/D$			
90	8	15	1/2	0.23	0.60	0.85
90	10	10	1	0.47	0.50	0.84
90	10	15	2/3	0.32	0.59	0.84
90	12	12	1	0.22	0.42	0.72
90	12	18	2/3	0.23	0.64	0.87
90	12	24	1/2	0.12	0.65	0.83

Table 9.5: Failure indices for varying SW and D ($L = 90$ mm).

9.1.5 Further Analysis of Optimised Design

Figure 9.5 shows the moment-rotation behaviour of this particular tape-spring hinge design. This relationship was obtained by rotating the hinge from the fully folded configuration to its initial, unstressed configuration while applying pure bending constraints. In order to obtain a less noisy response, the viscous pressure load over the external surface of the whole tube hinge was increased by a factor of 5, by setting $c_v = 10{\times}10^{-5}\rho c_d$, after carrying out a sensitivity study similar to that presented in Section 7.3.1. Note that now vibration is seen only near the highest peak which is actually a dynamic event.

The hinge changes its configuration from symmetric to asymmetric at an angle of 157°. This sudden change occurs with a local peak moment of 190 Nmm at an angle 155°. Then it follows a fairly smooth curve, varying from 150 Nmm to 112 Nmm. From 70° the top tape-spring starts becoming straight and this leads to a rise in the moment. A secondary peak of 463 Nmm at 27° corresponds to latching of the top tape-spring. Finally the complete hinge latches at an angle of 19° with a peak of 672 Nmm and then achieves its unstressed configuration.

The tape-spring hinge considered in Chapter 8 had slot parameters $SW = D = 30$ mm and $L = 140$ mm. The main concerns with that design were its low torsional stiffness and the fact that the the folds could move along the individual tape springs and so the hinge folded asymmetrically.

The new design has much wider and shorter tape-springs which increases the torsional stiffness by six times, the axial stiffness by a factor of two and the bending stiffness by one third, Table 9.6. Note that all these values are given for a 220 mm long tape-spring hinge. In the fully folded configuration, the new tape-spring hinge stores almost two and a half times more strain energy than the old hinge which

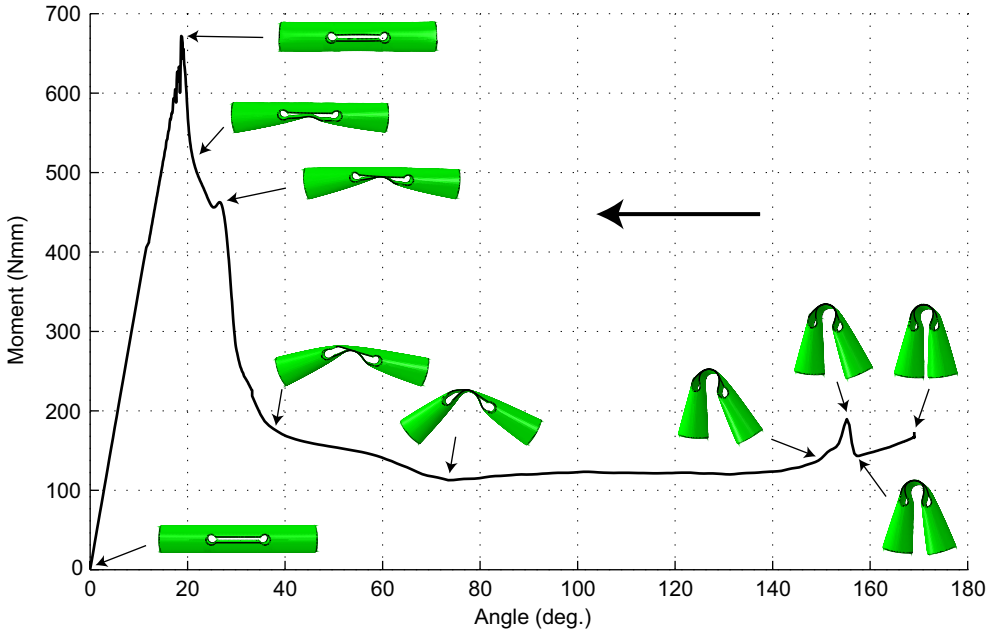

Figure 9.5: Deployment moment-rotation relation for improved design.

would be an advantage for deploying large structures. Also the new design has a much higher peak moment during deployment and it can be expected that the locking moment, i.e. the moment that needs to be applied to start folding the hinge, will also be much higher.

Design	L (mm)	Tape-spring width (mm)	Axial stiffness (N/mm)	Bending stiffness (Nmm/°)	Torsional stiffness (Nmm/°)	Stored energy (mJ)	Peak moment (Nmm)
Previous	140	25.5	562	3305	97	306	320
Improved	90	56	1081	4330	576	742	672

Table 9.6: Comparison of previous and optimised tape-spring designs.

Note that the peak moment of 320 Nmm for the old design is much lower than the value obtained in Section 8.1 because here the end cross-sections were not constrained. Figure 9.6 compares the moment-rotation relationships of the old and new designs, both obtained with $c_v = 10 \times 10^{-5}\ \rho c_d$. The old design has a steady state moment of around 65 Nmm with a single peak of 320 Nmm at an angle of 9°. As described earlier the new hinge has a steady state moment of around 130 Nmm with

two peaks of 463 Nmm and 672 Nmm at angles of 27° and 19°, corresponding to the latching of each tape-spring. Note that near the origin the two designs appear to have the same slope, which would indicate that they have the same bending stiffness. However the stiffness values presented in Table 9.6 were obtained with slightly different boundary conditions, more representative of the connections in an actual application.

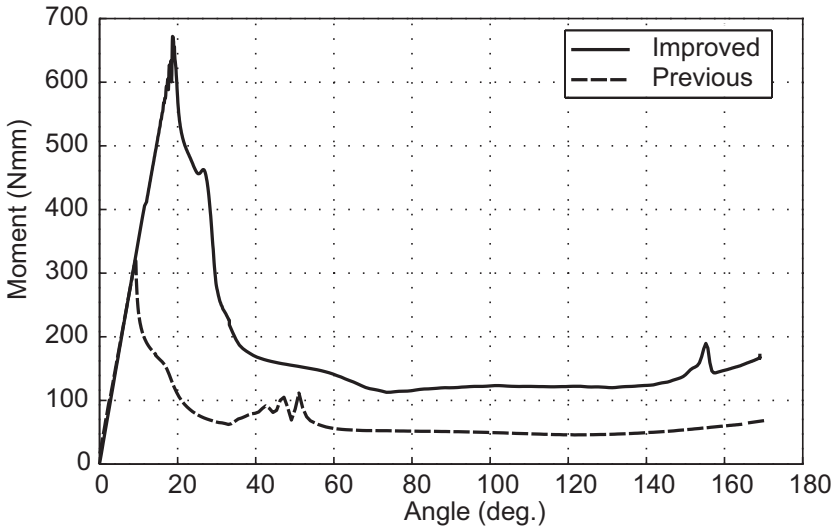

Figure 9.6: Comparison of moment-rotation variation for previous and optimised tape-spring designs.

9.2 Design of Tubular Booms

A deployment scheme that requires a 1 m long monolithic boom with two tape-spring hinges, to be folded around a small spacecraft, as shown Figure 9.7, is considered. The boom is rigidly connected to the spacecraft and expected to self-deploy upon release. It is also required to fully latch straight away, without overshooting, as soon as it becomes fully deployed to avoid any interference with the spacecraft itself or other equipment attached to it. The spacecraft was assumed to have a prismatic shape with cross-sectional dimensions of 400 mm by 360 mm and the centres of the two hinges were placed at distances of 200 mm and 600 mm from the root end of the boom. The distance between the root and the first hinge was chosen such as to allow the boom cross-section to deform near the hinge.

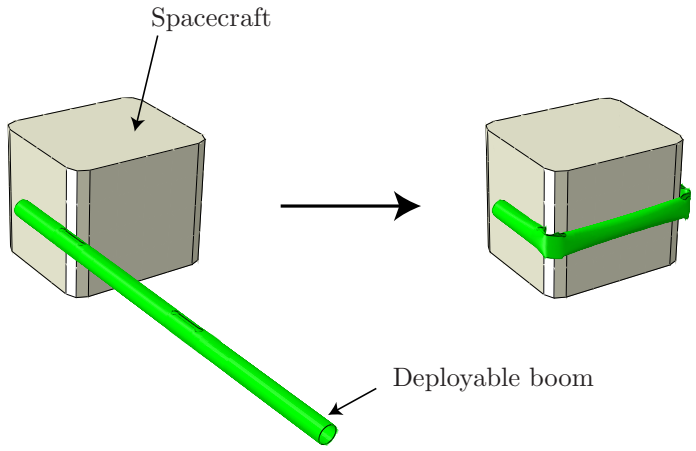

Figure 9.7: Deployable boom mounted on small spacecraft.

It would not be practical to analyse in full the folding and deployment behaviour of many booms with different hinge designs. Instead, three hinge designs were selected from Section 9.1 as indicated in Table 9.7. It should be noted that in the hinge designs considered in Section 9.1 the hinge cross-sections were left unconstrained and so were allowed to ovalise. The attachment of the boom to the spacecraft will present this deformation to some extent.

In the next sections we will present our detailed analyses of a boom based on the first hinge design, in Sections 9.2.1-9.2.2, and then compare key results for all three designs in Section 9.2.3 to finally choose a design to be taken forward.

Design	Slot parameters		
	L (mm)	SW (mm)	D (mm)
I	90	10	15
II	85	10	15
III	90	8	15

Table 9.7: Slot parameters for three hinge designs considered for boom design.

9.2.1 Dynamic Deployment Behaviour

Figure 9.8 shows snapshots from the dynamic deployment of the boom with hinges based on design I. Note that the hinge closer to the free end latches first while the rest of the boom remains almost stationary; then the root hinge starts deploying.

Figure 9.9 shows the angle-time responses for the two hinges. Also note that both hinge angles are defined with respect to the axis of the boom at the root and hence the two angles approximately coincide after the second hinge has deployed.

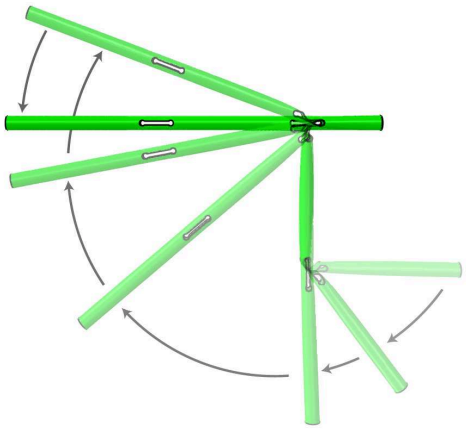

Figure 9.8: Snapshots during deployment (design I).

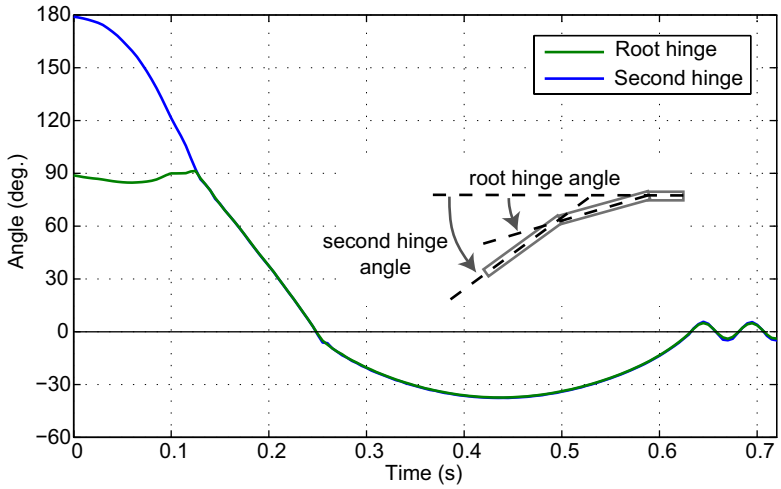

Figure 9.9: Angle-time response (design I).

In this particular hinge design the root hinge is unable to resist the angular momentum of the boom at the point of latching, hence the boom overshoots the fully deployed configuration. This behaviour should be avoided because the boom could become damaged, or could interfere with the spacecraft.

9.2.2 Failure Analysis

Figure 9.10 shows contours of the three failure indices for design I in the fully folded configuration of the boom. The top set of pictures represents the root hinge and the bottom set represents the second hinge. Note that the root hinge is subjected to higher loads than the other hinge. This is not surprising, because the fixed connection at the root of the boom restricts deformation of the boom cross-section whereas the second hinge is less constrained. Also note that the largest failure index is FI-3, which indicates that this boom design is governed by the interaction between axial and bending loads.

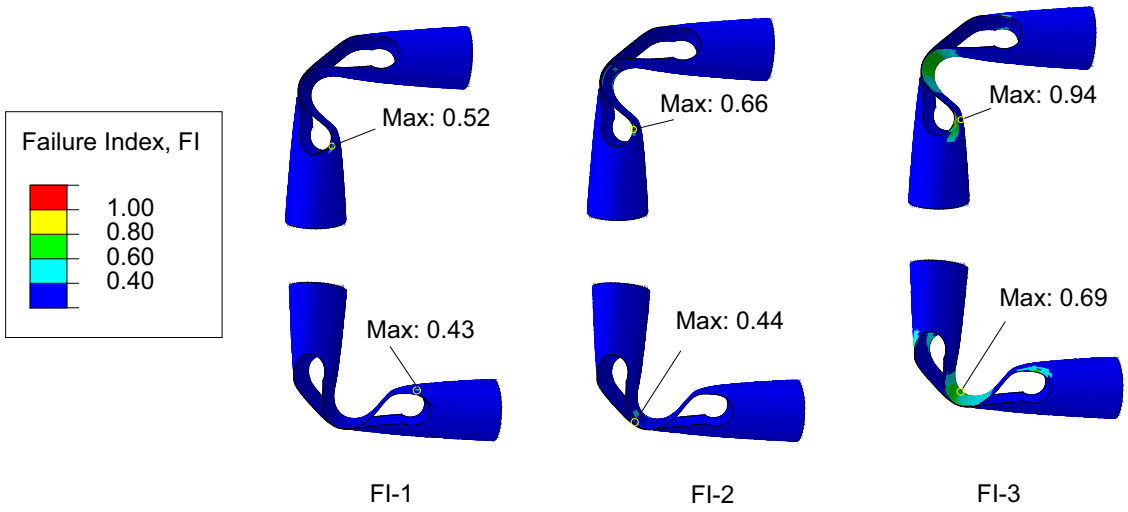

Figure 9.10: Failure indices for root hinge (top) and second hinge (bottom) in fully folded configuration, for hinge design I.

The failure analysis during deployment has to calculate the failure indices throughout the entire deployment simulation and then consider their maximum values. Hence, the stress-resultants were recorded at intervals of 0.005 s for the entire deployment simulation and the three failure indices were calculated. The present hinge design reaches its most critical conditions during the snapping of the second hinge, with FI-3 going from 1.13 to 1.15 during this snap, see Figure 9.11. Once the second hinge has latched FI-3 begins to decrease, see the image on the right in Figure 9.11.

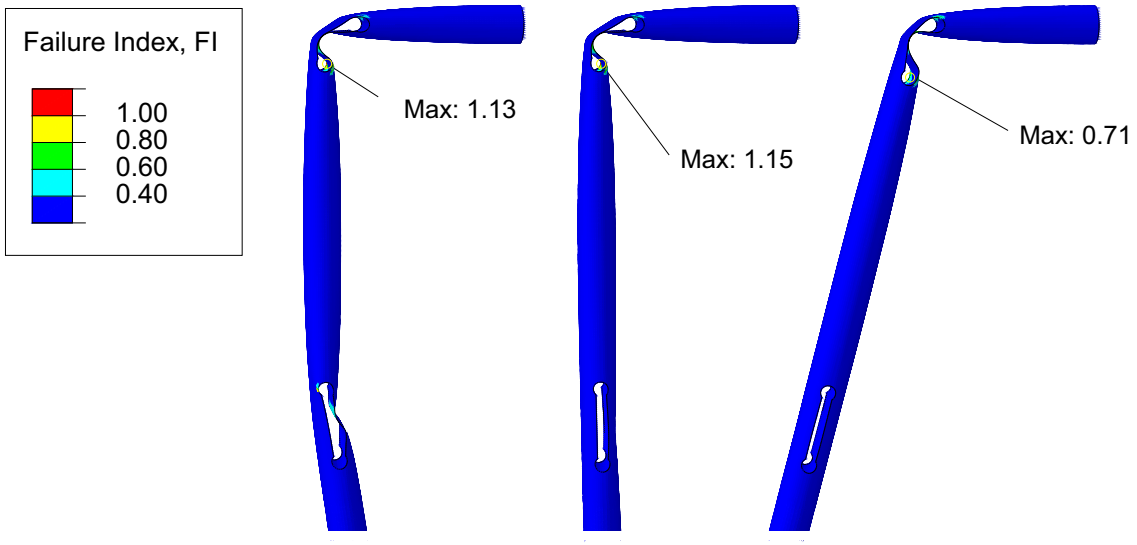

Figure 9.11: Maximum failure index at three stages of deployment, for boom based on hinge design I.

9.2.3 Selection of Tape-Spring Hinge Design

Table 9.8 lists the maximum failure indices, obtained for each of the three designs, both in the fully folded configuration and during deployment; the critical failure index is always FI-3, hence the dominant loading condition is the interaction between axial and bending loads. Note that the values during deployment are largest for all three designs, the corresponding locations of these maximum failure index are shown in Figure 9.12.

Design	Fully folded	During deployment
I	0.94	1.15
II	0.81	1.05
III	0.92	0.95

Table 9.8: Values of maximum failure index (FI-3) for three hinge designs.

Figure 9.13 compares the hinge angle-time responses of the three boom designs. Note that design I overshoots the fully deployed configuration, whereas both design II and design III latch straight away. Considering the results of the failure analysis and also the hinge angle-time response, design III was selected as the final design of the boom.

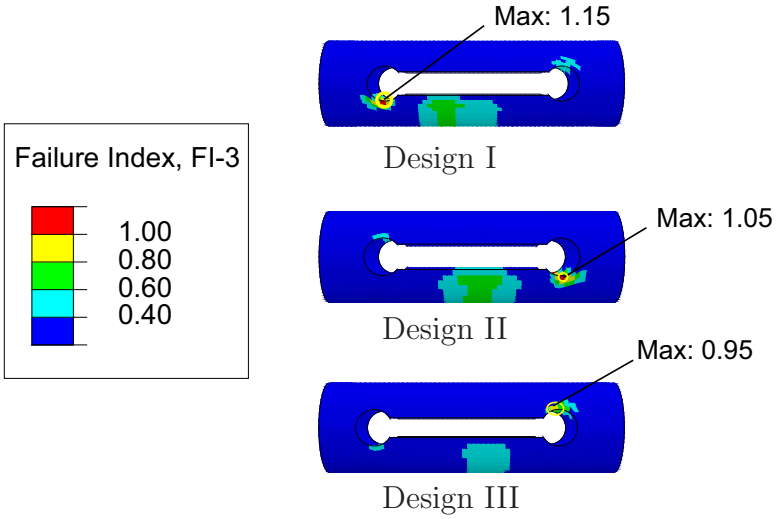

Figure 9.12: Location of maximum failure indices during deployment corresponding to Table 9.8, plotted on undeformed configuration.

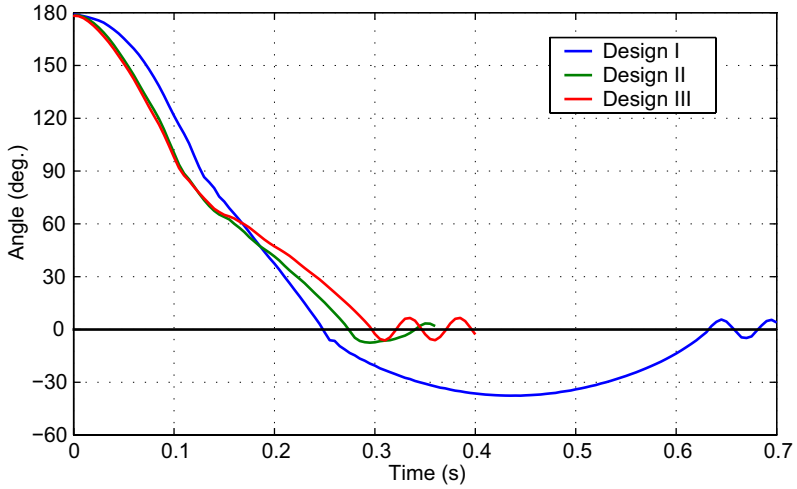

Figure 9.13: Comparison of hinge angle-time responses of the second hinge.

Chapter 10

Experimental Validation

This chapter presents a series of experimental validations of the simulation techniques developed in this research. A verification to failure analysis was performed by constructing a failure critical design and a failure safe design of a tape-spring hinge. Both were folded to the designed angle and the presence of any damage was investigated. The moment-rotation response obtained in Section 8.1 is compared against quasi-static deployment experimental results. The dynamic deployment behaviour of a single tape-spring hinge design is examined by experiments carried out with a gravity compensation system. Furthermore, the sensitivity to boundary conditions was examined by considering two different clamping conditions of the root of the boom. Finally the dynamic deployment behaviour of the two-hinge boom design selected in Section 9.2 is verified with a similar deployment experiment.

10.1 Validation of Failure Analysis

The failure criterion presented in Chapter 6 has been developed using the experimental results obtained from coupon tests. The accuracy of using this locus at the structural level is examined here.

Two hinge designs were selected from Chapter 9, one design is failure critical and the other is failure safe when folded to 180°. The failure critical design has slot dimensions of $L = 60$ mm, $SW = 10$ mm and $D = 15$ mm whereas the failure safe design has $L = 90$ mm, $SW = 8$ mm and $D = 15$ mm.

Figure 10.1a shows the maximum failure indices of the hinge in the fully folded configuration, but plotted on the undeformed configuration, for the failure critical

design. Note that the maximum failure index exceeds 1 in the regions highlighted in red. The same regions were seen to have become damaged during the experiment, Figure 10.1b.

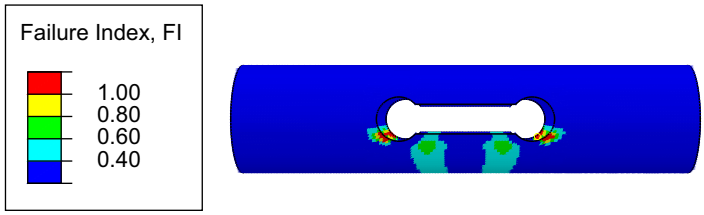

(a) Maximum failure indices plotted on undeformed configuration

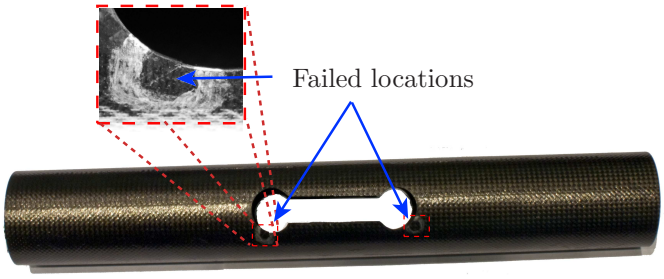

(b) Experiment

Figure 10.1: Failure analysis of failure critical design ($L = 60$ mm, $SW = 10$ mm and $D = 15$ mm).

Next the failure safe design is examined. Figure 10.2a shows the maximum failure indices contours corresponding to the fully folded configuration for this case. Note that the failure indices do not exceed 1, and hence the hinge can be safely folded to 180°, according to our simulation models. As predicted physical model could be safely folded. Figures 10.2b and 10.2c compare the fully folded configurations obtained from simulation and experiment, respectively.

In conclusion, the failure locus used in this research, which was constructed using uniaxial strengths obtained from coupon testing and then verified for combined loading conditions applied on different set of coupons, has now been further verified at the structural level. This result provides confidence in the failure predictability of the simulation techniques developed in this research.

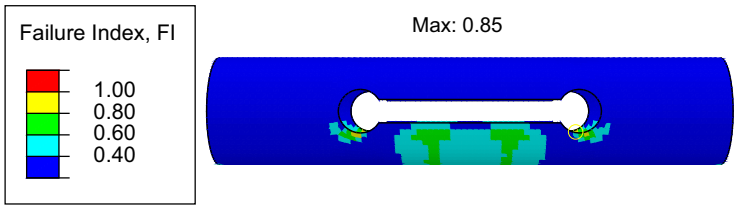

(a) Maximum failure indices plotted on undeformed configuration

(b) Fully folded configuration (simulation)

(c) Fully folded configuration (experiment)

Figure 10.2: Failure analysis and comparison of fully folded configuration of failure safe design ($L = 90$ mm, $SW = 8$ mm and $D = 15$ mm).

10.2 Quasi-Static Deployment

A verification of the moment-rotation response of the initial hinge design presented in Section 8.1 was carried out by means of a quasi-static deployment experiment. This tape-spring hinge has slot parameters of $L = 140$ mm and $SW = D = 30$ mm which gives a design with two 140 mm long, 25 mm wide tape-springs.

10.2.1 Test Procedure

Folding of this tape-spring hinge is best initiated by pinching it in the middle, to avoid high bending moments that may damage the hinge. Once the height of the central region has been approximately halved the ends of the tape-spring hinge can be rotated in opposite directions.

Deployment tests were carried out by attaching a pair of tube holders to the apparatus previously used by Seffen and Pellegrino (1999) to study the behaviour of tape springs. This apparatus consists of two small gear boxes with a reduction ratio of 80, one attached to a rigid base and the other mounted on a linear bearing, supporting hollow strain-gauged shafts. The base rotation of the shafts is measured with a resolution of 0.045° and to an accuracy of ±0.4° (due to backlash). The ends of the tape-spring hinge are attached to the shafts, which behave as load cells with a linear response up to 1.10 Nm and an accuracy of ±2 Nmm.

Before starting the test, the strain gauge readings were set to zero in the deployed, i.e. unstressed configuration shown in Figure 10.3. Then, the tape-spring hinge was pinched in the middle and folded by rotating the ends by equal amounts. During the test the ends were rotated back in small steps while keeping the end moments roughly equal. This was done by rotating the moving gear box by the desired amount and then rotating the fixed gear box to equalise the end moments.

At the end of the test the moment-rotation profile was obtained by plotting the folding angle, ψ, defined as the difference between the end rotations and the corresponding moment at each step (Mallikarachchi and Pellegrino, 2011b).

10.2.2 Comparison

Figure 10.4 shows a comparison between the deformed configurations of the tape-spring hinge that were observed during deployment in the test rig, with snapshots from the finite element simulation. This qualitative comparison shows very good

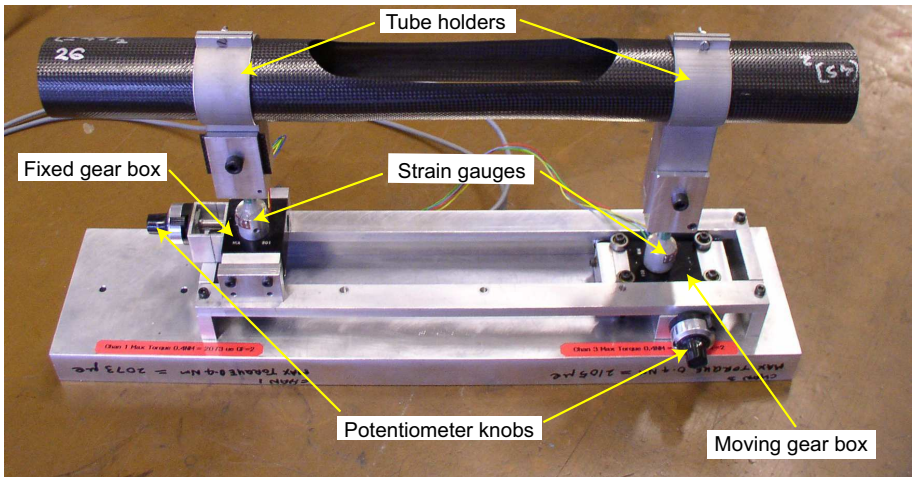

Figure 10.3: Quasi-static deployment test rig.

agreement in both the position of the regions of localised deformation and the overall geometric configurations of the tape-spring hinge.

Figure 10.5 shows a comparison between the deployment moment-rotation profile measured experimentally with the simulated response. Unlike the moment-rotation profile in Figure 8.2, the particular simulation results shown here were obtained from a model that included two 5 mm long Aluminium rods, to model the torsional stiffness of the holders. The torsional constant of the rod cross-section was set equal to 12 mm^4, to match the angle of snap back observed in the experiment, i.e. 2.3°.

It can be seen that the bending moment is approximately constant until the final snap back, apart from a small hump caused by the loss of contact between the internal and external tape springs, in the fold region. Note that the particular tape-spring hinge design that was tested had a unique equilibrium configuration when the deployment moment is zero.

Overall, the simulation has fully captured the experimentally observed behaviour. However, the measured steady-state deployment moment had an average value of 80 Nmm whereas our simulation gave around 67 Nmm. Also the peak in the hump in the experiment was at $\approx 40°$ with a maximum moment of 104 Nmm, whereas in the simulation it was at $\approx 54°$ with a maximum of 117 Nmm. Also, the measured peak moment at snap back was 660 Nmm whereas it was significantly higher, 1078 Nmm, in the simulation.

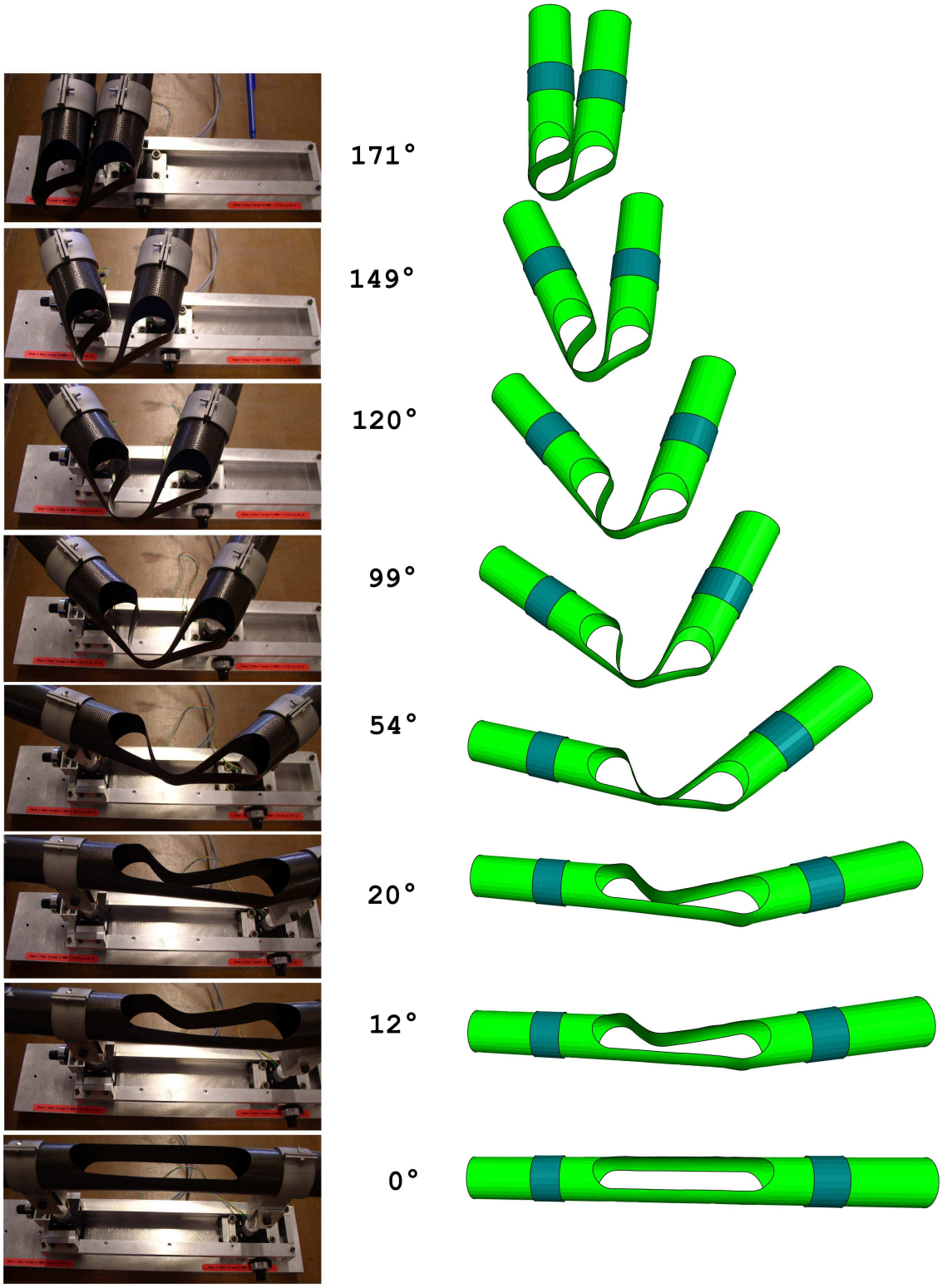

Figure 10.4: Comparison of hinge configurations during quasi-static deployment.

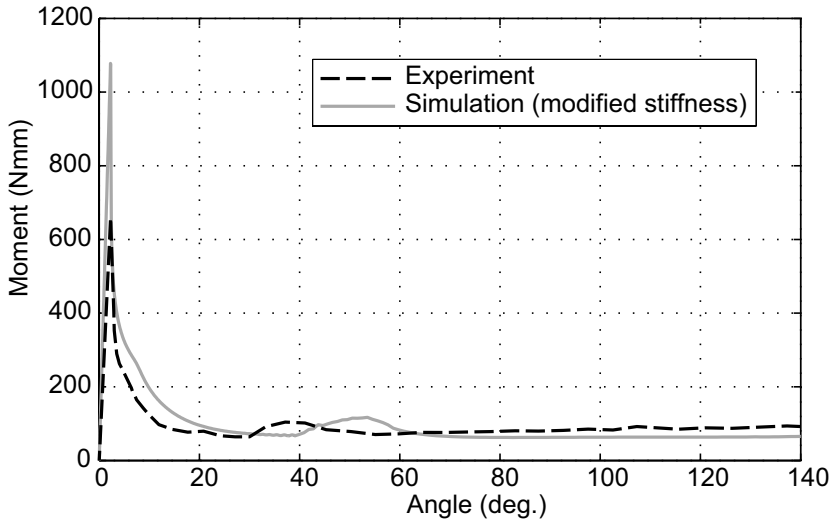

Figure 10.5: Comparison of moment-rotation profiles during deployment.

10.3 Dynamic Deployment of Tape-Spring Hinge

The dynamic deployment behaviour of the same tape-spring hinge design considered in Section 10.2 is investigated here.

10.3.1 Experimental Setup

The hinge was connected to an aluminium-alloy tube with an outer diameter of 38 mm and thickness of 0.9 mm. The connection was made by inserting the aluminium-alloy tube into the tape-spring hinge to provide a 25 mm overlap which was wrapped with electrical insulation tape and tightened with a Jubilee clip. The complete structure was 1025 mm long including the 1000 mm long boom and an additional length of 25 mm to provide a connection at the root of the boom, Figure 10.6.

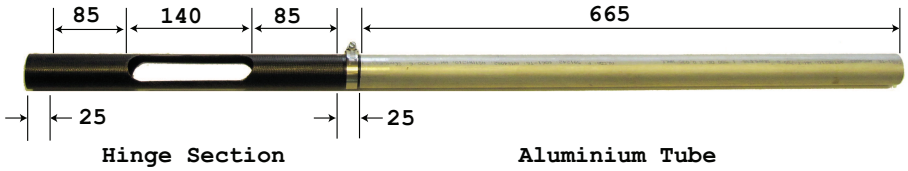

Figure 10.6: Boom with single tape-spring hinge (units: mm).

Deployment tests were carried out on a rig that provided a single-point offload through a string attached to the outer surface of a tube, at a point directly above the centre of gravity of the aluminium-alloy tube. The other end of the string was run through a pulley located at a height of 4650 mm, directly above the centre of the tape-spring hinge. This constraint allowed the boom to only move in a horizontal plane. Figure 10.7 shows the experimental setup.

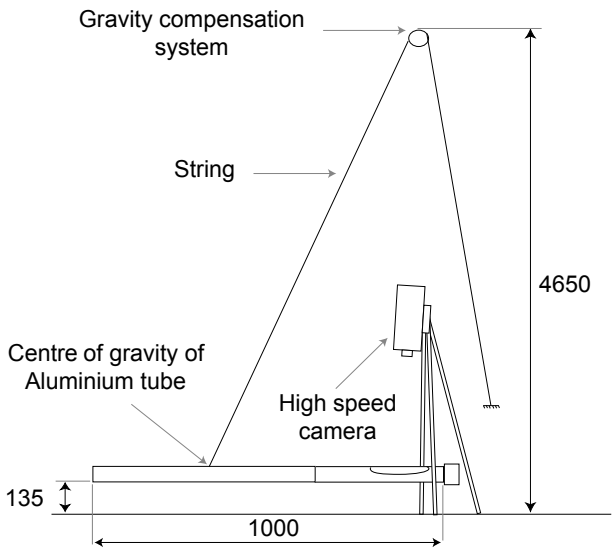

Figure 10.7: Experimental setup for dynamic deployment of single-hinge (units: mm).

Two different clamping conditions were used to investigate the sensitivity of the deployment to the boundary conditions. First the root end of the boom was slid onto a 37.8 mm diameter 25 mm long solid aluminium-alloy cylindrical fitting wrapped with thread sealing tape. A 6 mm thick sheet of rubber was wrapped around the tube and clamped with a Jubilee clip tightened with a torque of 1.13 Nm, Figure 10.8a. The cylindrical fitting was attached to a massive steel structure which provided a fixed end condition for the boom.

The second method was to slide the root end of the boom onto a similar aluminium-alloy fitting but then covered with a heat shrinkable sleeve heated to fit onto the tube. Then two Jubilee clips were tightened with a torque of 1.13 Nm and aluminium-alloy fitting was attached on to a 1 m by 1 m granite table, Figure 10.8b.

The deployment of the boom was recorded with a Phantom V12.1 high speed camera held directly above the folding part of the boom; its field of view included the folding part of the boom, up to the Jubilee clip. A second video camera was used

(a) Clamp condition I

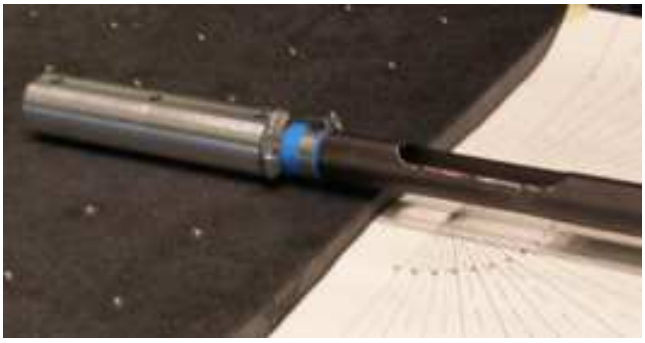

(b) Clamp condition II

Figure 10.8: Clamp conditions for dynamic deployment of single hinge.

to get an overall view of the deployment. A sheet of white paper with black lines at 5° angles provided a horizontal background from which the deployment angle could be measured.

First the boom was folded 45° and then released while recording the deployment with the high speed camera at a rate of 300 frames per second.

The same procedure was repeated after replacing the composite tube hinge with a second one, nominally identical to the first. Similar tests were carried out on both hinges after they were folded 90°. The experiment with the folding angle of 45° was done only with clamp condition I, but in the case of the 90° folding the tests were repeated with both clamping conditions.

Figure 10.9 shows a series of images obtained from the experiment with the folding angle of 45°. The deployment history of the boom was derived by measuring the deployment angle from one frame out of every 25 frames (0.0083 s) using a specially written Matlab program that computes the angle between two lines drawn manually. Each picture was loaded to the background and the two lines were aligned with the boom and the 0° line on the white background sheet.

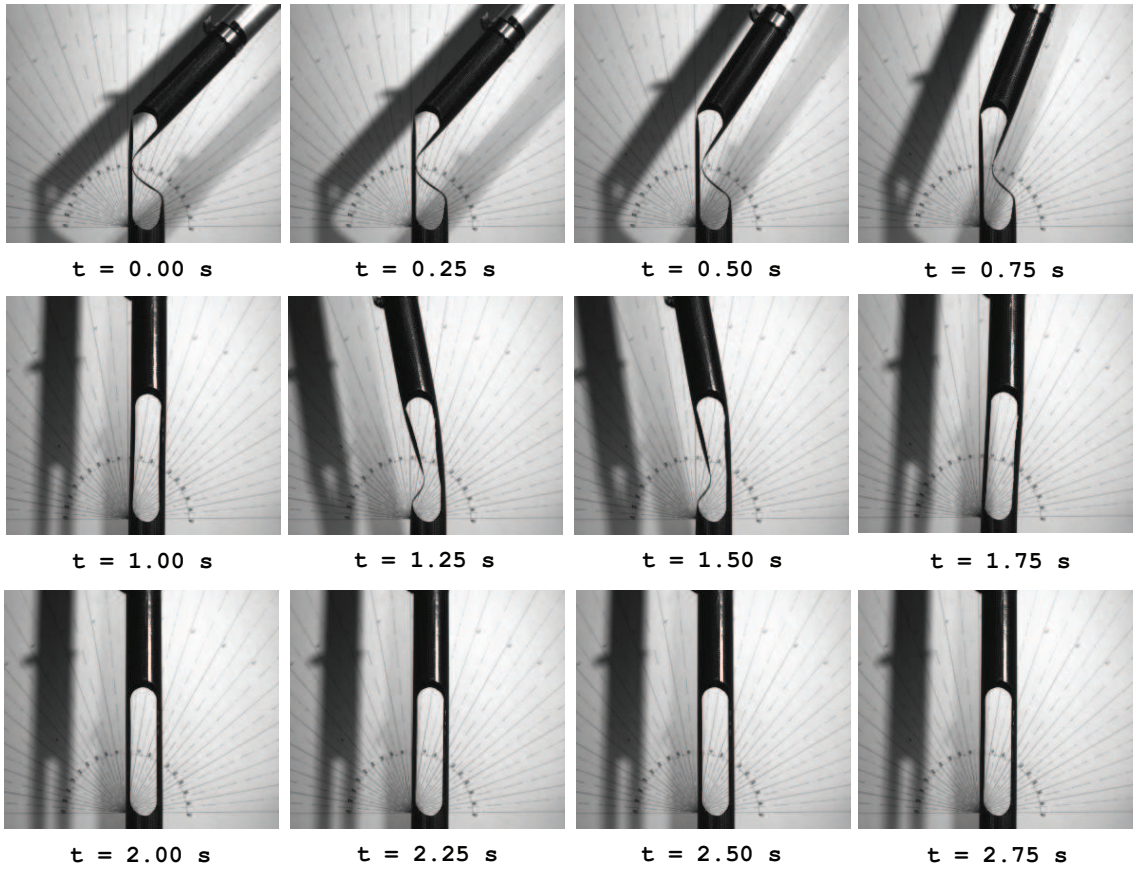

Figure 10.9: Photos taken during deployment of boom folded 45 °.

Note that the hinge takes about 1 s to achieve its fully deployed configuration, but it is subjected to back buckling due to excessive kinetic energy. Finally it vibrates about the fully deployed configuration.

The experimental results from the tape-spring hinge initially folded to 90° gave two different angle-time responses for the phase of buckling of the tape-springs, Figure 10.10. In both experiments the initial deployment took 1.48 s, then the tape springs back buckled. In the test with clamping condition I, the boom underwent maximum overshoots of -45°, +11° and -4° over a period of 2.95 s before entering the final vibration phase. In the other case, the boom overshot only twice with maximum angles of -29° and +4° over a period of 1.94 s. The final vibration phase was similar for the two cases.

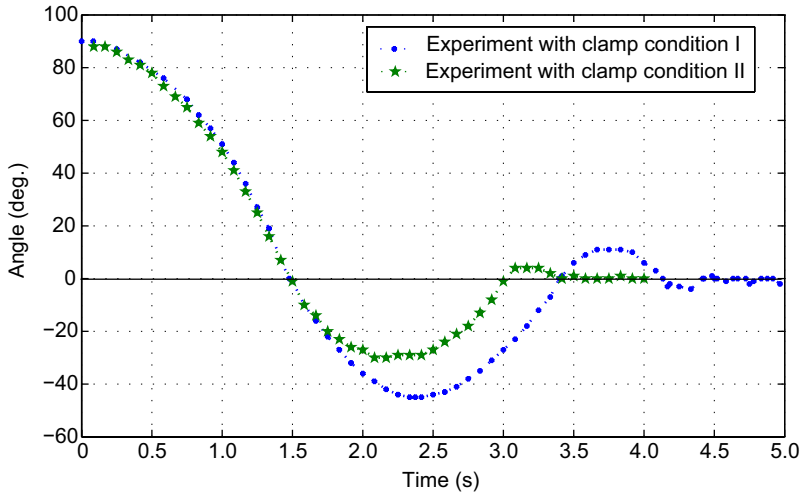

Figure 10.10: Angle-time relationship for tape-spring hinge folded 90°.

It should be noted that, although helpful in describing the deployment behaviour, the deployment angle does not fully identify the configuration of the boom. For example, the deployment angle may be zero with the boom not in the fully deployed configuration, as shown in Figure 10.11. Therefore it is important to investigate the localised behaviour of the hinge. A detailed comparison of hinge configurations in the two cases is presented in the next section.

(a) Fully deployed configuration

(b) Hinge sheared to the right

(c) Hinge sheared to the left

Figure 10.11: Different configurations of hinge with a zero deployment angle.

10.3.2 Comparison

Figure 10.12 compares the measured angle-time response with the predictions from a simulation with parameters $\xi = 0.1$ and $c_v = 0$. Note that there is excellent agreement between experiment and simulation during the initial deployment phase. For example, for the boom folded 45° the simulation showed a monotonic decrease in deployment angle from 45° to 0° over a period of 0.93 s; in the experiment it took 0.96 s.

The second phase of the dynamic process shows some very interesting behaviour. The experimental angle-time relationship for the boom folded 45°, Figure 10.12, shows that this boom rotated 17° beyond the fully deployed configuration and became fully latched the second time it reached the fully deployed configuration. The simulation predicts that the boom should go through the fully deployed configuration 4 times before becoming fully latched. Also note that simulation gives a noisy response; this is because use of only ξ is not sufficient to suppress high frequency oscillations. This oscillation at the snapping of the boom forces the hinge to buckle and hence overshoot 4 times.

The simulation for the 90° folded boom presented in Section 8.2 used the parameters $\xi = 0.1$ and $c_v = 2{\times}10^{-5} \times \rho c_d$ to suppress these high frequency oscillations. Figure 10.13 compares the experimental results with the two different clamping conditions to simulations with slight changes in initial conditions. Note that experiment I and simulation I correspond to a high overshoot angle and experiment II and simulation II to a low overshoot angle. All four responses show a deployment phase of 1.48 s. In experiment I the boom overshot three times, with maximum overshoot

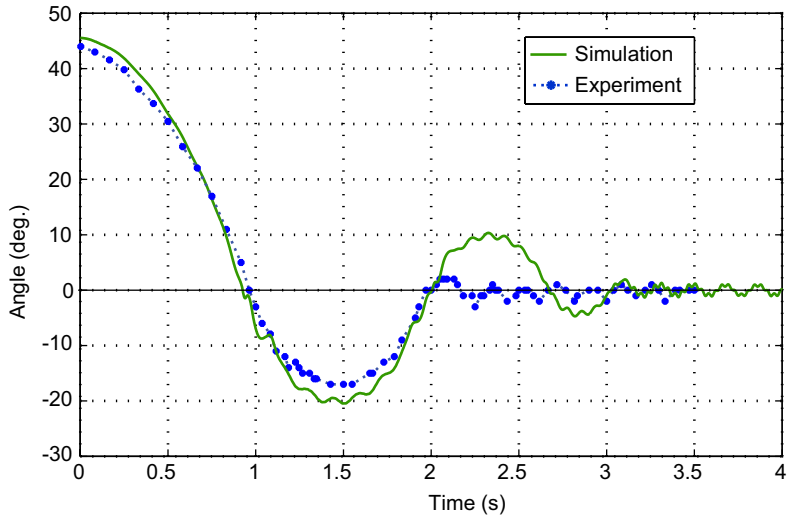

Figure 10.12: Comparison of experiment and simulation results for tape-spring hinge folded 45°.

angles of -45°, +11° and -4° whereas for the simulation the values are -46°, +19.6° and -4°. In the case of experiment II, the boom overshot only twice, with maximum overshoot angles of -30° and +4°. This time, simulation II predicts maximum overshoot angles of -33° and +5°. The final vibration phase is fairly well matched for all four cases.

As explained in Figure 10.11 a comparison of overall angles does not fully describe the behaviour of these structures as the same overall angle may correspond to different localised folds. Figure 10.14 compares the localised deformations of the tape-spring hinge by means of snapshots taken from experiment I and simulation I. Note that the localised deformations are fairly well matched up to 2.25 s. Differences afterwards are mainly due to the simulation predicting a higher overshoot angle and so delaying the response.

Figure 10.15 compares snapshots from experiment II and simulation II. Note that the localised deformations are fairly well matched throughout.

The sensitivity of these results indicates that the particular hinge design used in the deployment presented in this section is rather unpredictable.

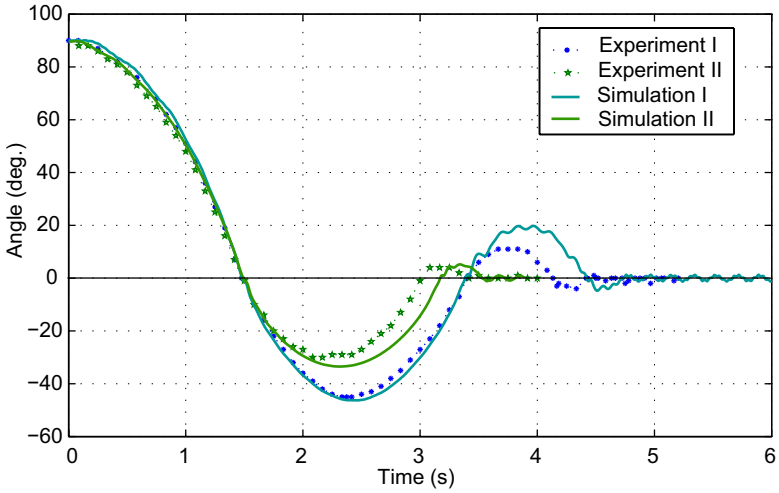

Figure 10.13: Angle-time comparison for tape-spring hinge folded 90°.

10.4 Dynamic Deployment of Two-Hinge Boom

The dynamic deployment behaviour of multiple hinge booms were studied in order validate results presented in Section 9.2. A boom based on Design III which has two tape-spring hinges with slot parameters, $L = 90$ mm, $SW = 8$ mm and $D = 15$ mm was built and tested to verify the accuracy of the simulation results and the failure analysis on which this design had been based.

10.4.1 Experimental Setup

A 38 mm diameter, 1.05 m long and 0.22 mm thick boom was made from two-ply plain weave fabric laid at 45° to the axis of the boom. An additional 50 mm section of the boom was used for the root connection and slots were placed as shown in Figure 10.16.

The root end of the boom was slid onto a solid aluminium-alloy support with a 37.8 mm diameter and 50 mm long cylindrical fitting. The overlap region was wrapped with electrical insulation tape and then clamped with a Jubilee clip tightened with a torque of 1.13 Nm. The aluminium-alloy support was bolted to a 1 m by 1 m granite table.

This boom is able to self-deploy while carrying its own self weight however, to minimise the gravitational effects, a single-point off-load was provided through a

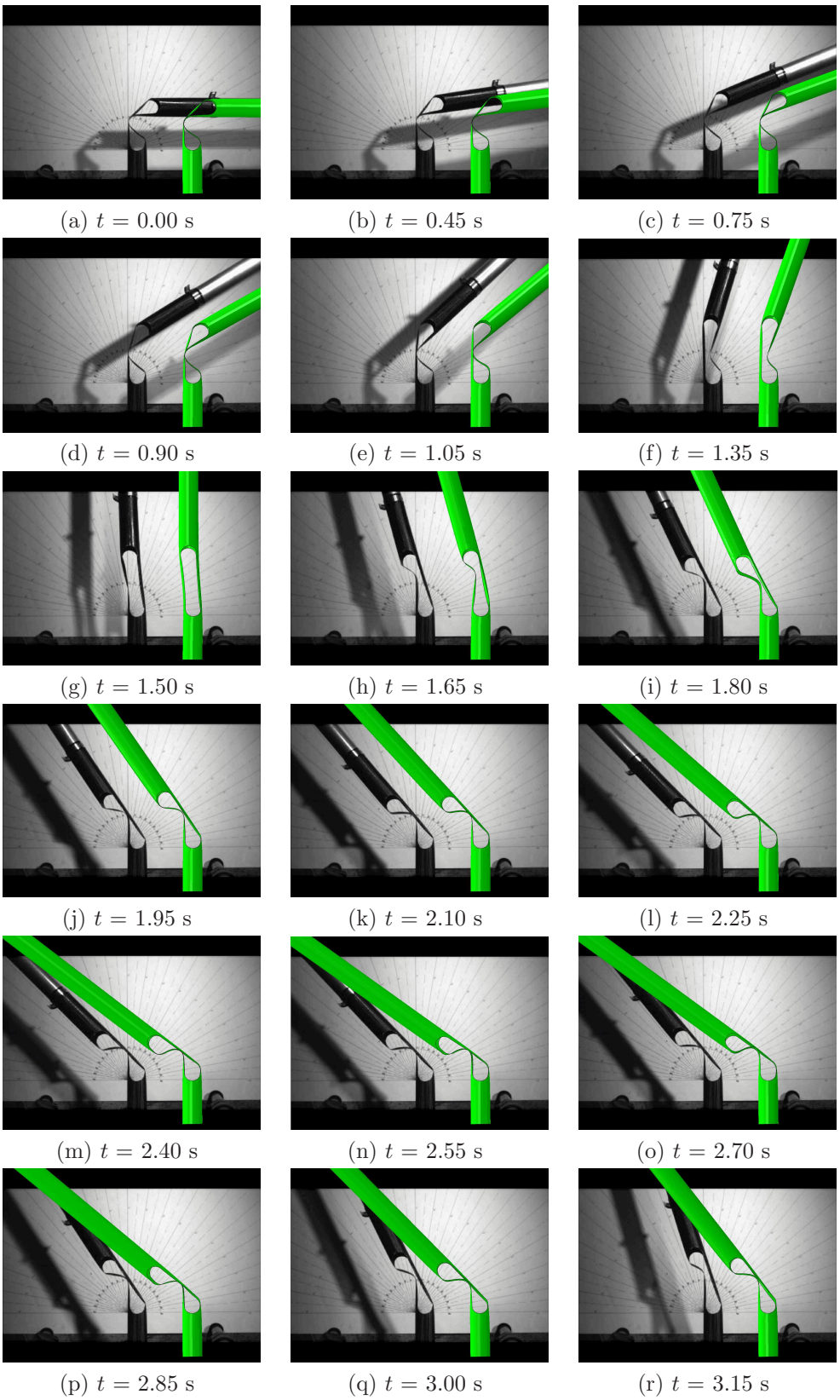

(a) $t = 0.00$ s (b) $t = 0.45$ s (c) $t = 0.75$ s

(d) $t = 0.90$ s (e) $t = 1.05$ s (f) $t = 1.35$ s

(g) $t = 1.50$ s (h) $t = 1.65$ s (i) $t = 1.80$ s

(j) $t = 1.95$ s (k) $t = 2.10$ s (l) $t = 2.25$ s

(m) $t = 2.40$ s (n) $t = 2.55$ s (o) $t = 2.70$ s

(p) $t = 2.85$ s (q) $t = 3.00$ s (r) $t = 3.15$ s

Figure 10.14: Comparison of snapshots from experiment I and simulation I.

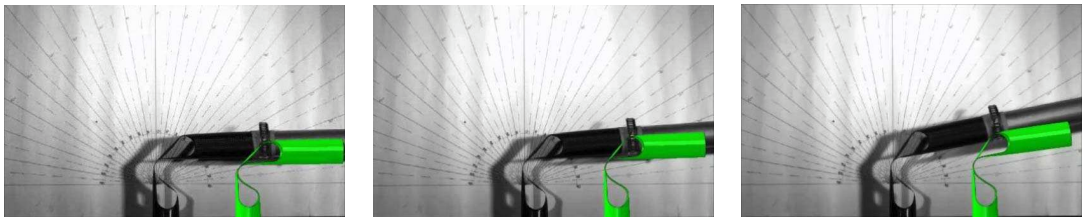

(a) $t = 0.00$ s (b) $t = 0.13$ s (c) $t = 0.46$ s

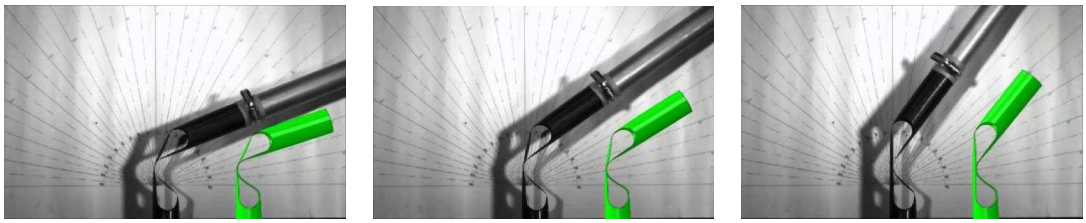

(d) $t = 0.75$ s (e) $t = 0.98$ s (f) $t = 1.20$ s

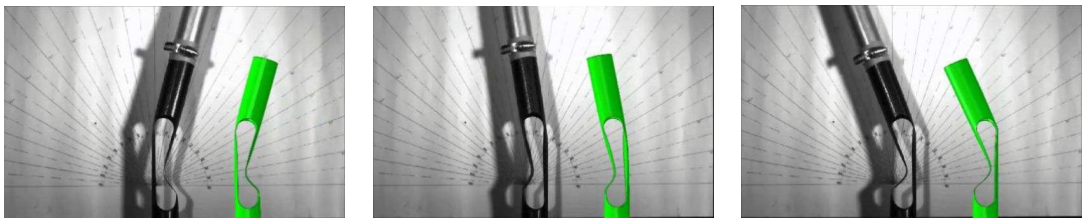

(g) $t = 1.40$ s (h) $t = 1.65$ s (i) $t = 1.87$ s

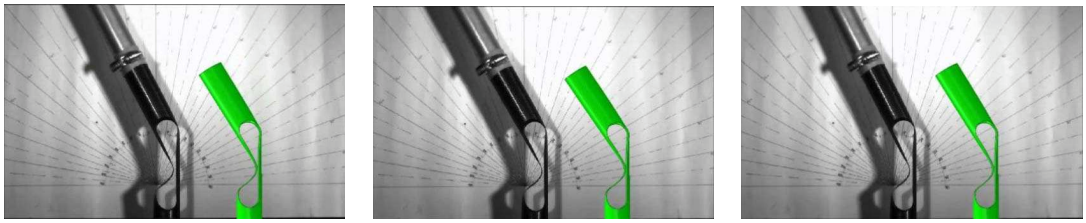

(j) $t = 2.06$ s (k) $t = 2.18$ s (l) $t = 2.70$ s

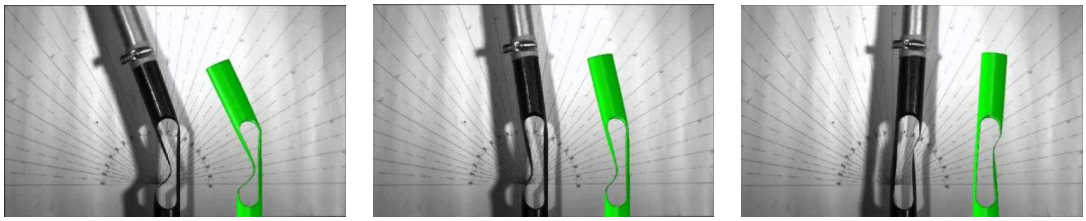

(m) $t = 2.94$ s (n) $t = 3.15$ s (o) $t = 3.38$ s

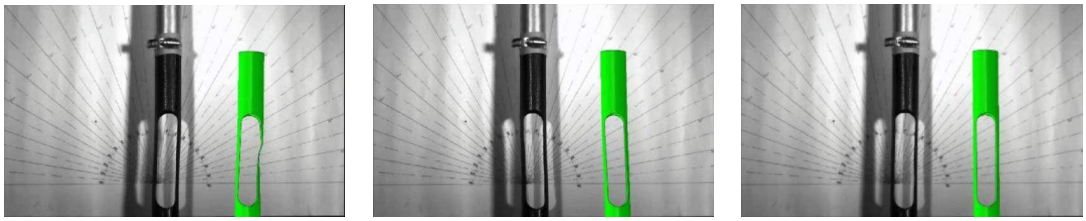

(p) $t = 3.64$ s (q) $t = 3.93$ s (r) $t = 4.13$ s

Figure 10.15: Comparison of snapshots from experiment II and simulation II.

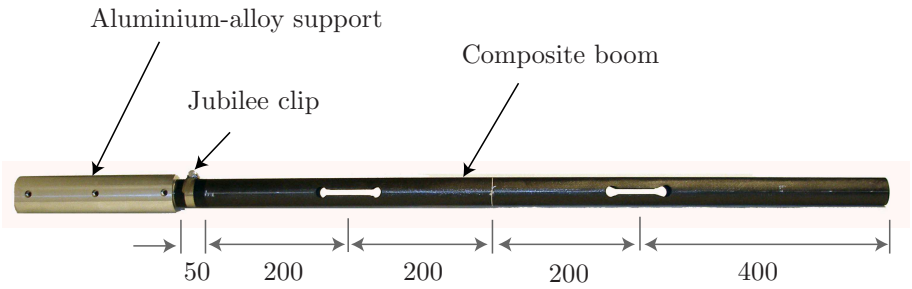

Figure 10.16: Two-hinge boom (units:mm).

string attached to the outer surface of the boom at a distance of 400 mm from the root. The other end of the string was run through a pulley located at a height of 4.65 m directly above the root hinge.

A 400 mm long, 360 mm wide, and 310 mm tall wood box was placed next to the boom to simulate the spacecraft. A Phantom V12.1 high speed camera was held directly above the root hinge with a wide angle lens to capture the detailed behaviour. A Casio EX-FH20 high speed camera was placed at a height of about 4.8 m above the boom to capture the overall deformation. Figure 10.17 shows a schematic of the complete experimental setup.

Great care was needed to fold the boom, specially the root hinge because the chosen design was known to have a very small margin against failure in the folded configuration. First the root hinge was pinched and folded to 90° and then the same procedure was followed to fold the second hinge, Figure 10.18. The fully folded boom was held horizontal by hand, in the tip region, and was released while recording the deployment with the two high speed cameras, at rates of 1000 and 420 frames per second, respectively.

Snapshots of deployment were extracted from the videos recorded by the two high speed cameras and the hinge angles were measured using the same technique described in Section 10.3.1 (Mallikarachchi and Pellegrino, 2011a).

10.4.2 Comparison

It had been predicted by the finite element simulation that this boom should achieve its fully deployed configuration straight away, without any overshoot. Both simulation and experiment showed that the boom comes to its fully deployed configuration in about 0.3 s, becomes fully latched, and then oscillates around the deployed con-

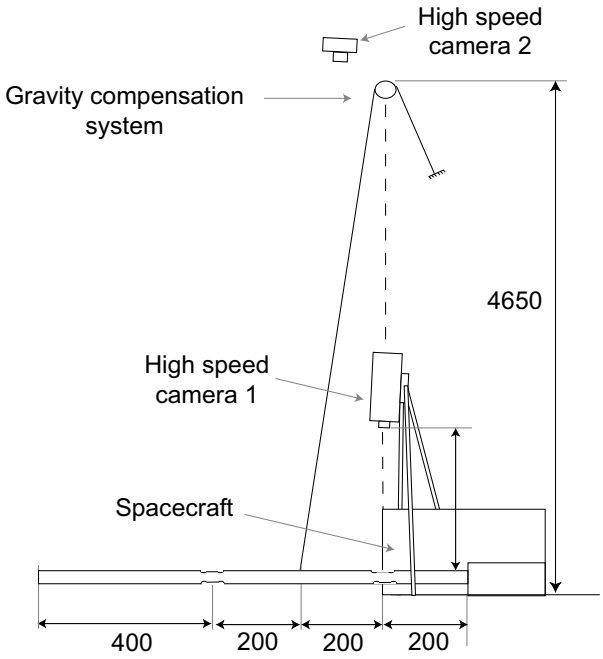

Figure 10.17: Experimental setup for two-hinge boom (units: mm)

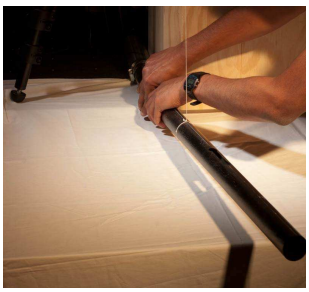

(a) Pinching root hinge

(b) Folding

(c) Fully folded configuration

Figure 10.18: Setting up two-hinge boom deployment experiment.

figuration. The experiments also confirmed that the root hinge remains practically folded until the second hinge is completely deployed. Figure 10.19 shows snapshots of the complete boom deployment, obtained from the second high speed camera.

Figure 10.20 compares the angle-time response of the root hinge. Note that the hinge remains almost fully folded for about 0.1 s. The second hinge deploys within this period and then remains latched throughout the rest of the experiment. The experimental and simulated angle-time responses show excellent agreement apart from a small initial difference, probably due to the hand release technique in the experiment. In the experiment the boom comes to its fully deployed state at 0.288 s whereas in the simulation it takes 0.297 s. The final vibration portion of the response is also well predicted.

Figure 10.19 compares the localised deformation of the root hinge. Note that the simulated response shows that after 0.105 s the two tape-spring hinges should swap their fold locations whereas in the experiment this change did not happen. It is known that this type of hinge has an unstable symmetric hinge configuration and hence is forced to take an unsymmetric configuration. When the second hinge latches a dynamic wave travels through the boom and in the simulation this flips the root hinge configuration, however this did not happen in the experiment. The energy difference between these two alternative configurations may possibly be rather small. However, due to compact hinge geometry this switching does not affect the overall path of the tip of the boom which was a concern with the design presented in Section 10.3.

(a) t =0.000 s (b) $t = 0.055$ s (c) $t = 0.074$ s

(d) $t = 0.083$ s (e) $t = 0.102$ s (f) $t = 0.112$ s

(g) $t = 0.121$ s (h) $t = 0.140$ s (i) $t = 0.198$ s

(j) $t = 0.226$ s (k) $t = 0.276$ s (l) $t = 0.287$ s

(m) $t = 0.300$ s (n) $t = 0.324$ s

Figure 10.19: Snapshots of two-hinge boom during deployment experiment.

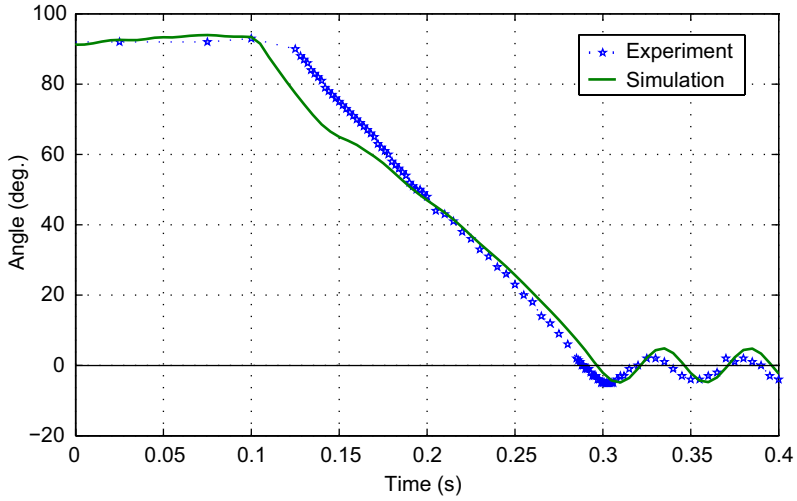

Figure 10.20: Comparison of root hinge angle-time variation.

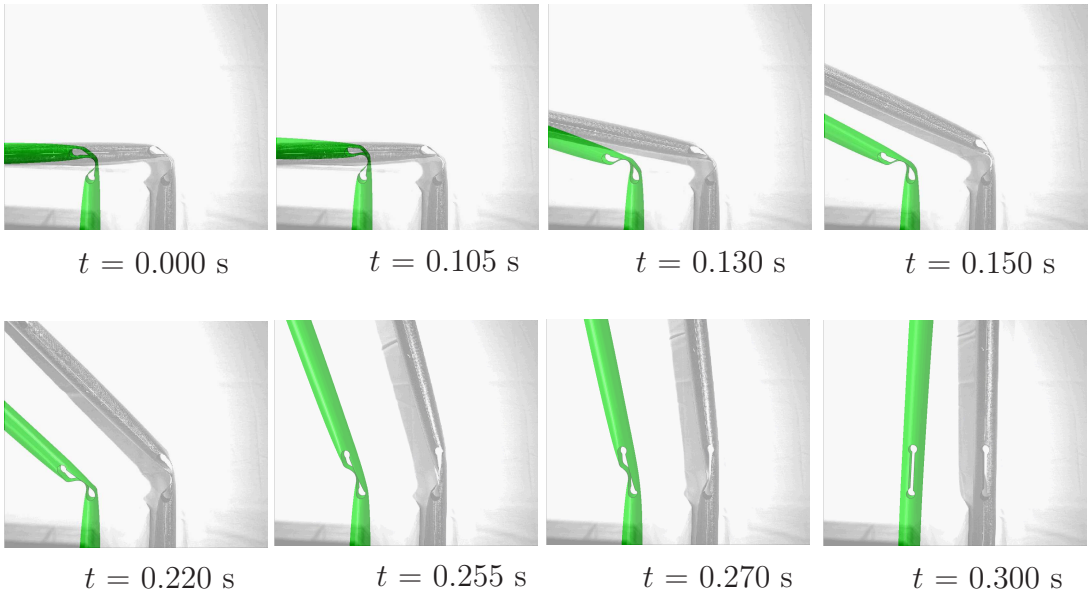

Figure 10.21: Comparison of local deformation of root hinge of two-hinge boom.

Chapter 11

Conclusions and Future Work

This dissertation has presented novel design tools for lightweight composite booms with multiple tape-spring hinges and has also established a design methodology for these structures. The whole process of folding and deployment of tape-spring hinges under both quasi-static and dynamic loading has been captured in detail through finite element simulations, starting from a micro-mechanical model of the laminate based on the measured geometry and elastic properties of the woven tows. Geometric optimisation of the hinge design has been carried out through a parametric study using a stress-resultant based failure criterion. Finally an example of designing 1 m long self-deployable boom that can be stowed by folding it around a small spacecraft has been presented.

The main objectives of research presented in this dissertation were (i) to predict the stiffness properties of thin laminates made of plain weave carbon fibre reinforced composites, (ii) to develop a six-dimensional failure criterion based on force- and moment-resultants, (iii) to capture the detailed structural behaviour of tape-spring hinges under both quasi-static and dynamic loading conditions, (iv) to investigate the sensitivity of the dynamic latching behaviour to the method of connection of tape-spring hinge booms at the root, (v) to perform geometric optimisation of tape-spring hinges and (vi) to establish a design methodology for tubular booms with multiple tape-spring hinges. The main achievements are summarised here and recommendations for future work are presented.

11.1 Important Findings and Discussion

Micro-Mechanical Modelling

Thin laminates made from woven tows of fibres are not modelled accurately by classical laminate theory, (Soykasap, 2006). Hence, the two-ply laminate studied in this dissertation was modelled as a linear-elastic thin Kirchhoff plate whose properties are defined by a homogenisation technique.

The micro-mechanical models proposed in this study use a simple description of the geometry of the reinforcement. The tow cross-sectional area, thickness and waviness were measured from a series of micrographs and the fibre volume fraction was calculated from the dry weight of the fabric, the resin film weight and the density of fibres and resin. The fibre and resin properties provided on the manufacturer's data sheets were used to estimate the homogenised tow properties. The properties of the tows were defined by the engineering constants E_1, E_2, ν_{12}, G_{12} and G_{23}. The first four constants were defined based on the rule of mixtures and the Halpin-Tsai equations. The fifth constant was computed by solving a quadratic equation proposed by Quek et al. (2003).

Average values for the tow cross-section and wave profile were obtained by studying four different cross-sectional and weave profiles that matched average area and weave length obtained from micrographs.

The stiffness of two-ply plain weave composites was described by the ABD matrix obtained from a homogenised plate model. This matrix was derived from a unit cell consisting of triangular prism elements using periodic boundary conditions. A specific procedure has been set up for deriving the homogenised material properties of two-ply plain weave laminates, based on a repeating unit cell approach.

The homogenised properties that were determined by this method were verified with a series of carefully designed experiments, which measured the tensile stiffness, Poisson's ratio and bending stiffness for both 0/90 and ± 45 fibre orientations.

An important factor in modelling a multi layer fabric composite is the relative positioning of each layer. Following Soykasap (2006) two extreme ply arrangements, fibres in-phase and fibres out-of-phase were considered. The results showed that there is a significant variation in bending stiffness for 0/90 laminates, Table 5.2. However, the hinges considered in this research were made with two-ply ± 45 laminates due to their resistance to crack initiation near the transition region between

the circular and rectangular part of the slot. The effect of two ply arrangements is rather small for ±45 laminates.

An attempt was made to use homogenisation in reverse to predict material failure. Three common failure criteria, maximum strain, maximum stress and Tsai-Wu were used to predict failure. Laminate failure strains and curvatures obtained from tension, compression, shear and bending failure tests performed on test coupons were used for validation. It was shown that although the micro-mechanical model is effective in predicting initial stiffness its failure predictions are often rather poor.

Failure Criterion

A six-dimensional failure locus for two-ply plain weave laminates was developed in terms of force and moment resultants. The failure coefficients were estimated with five uniaxial tests, and five more combined loading configurations were used for validation of the failure locus. It was shown that the quadratic failure envelope by Karkkainen and Sankar (2007) is only valid for in-plane loading conditions and hence additional limits were developed for bending and in-plane and bending interaction.

A new experimental procedure was introduced to investigate the behaviour under combined bending and in-plane loading by testing initially curved specimens. It was assumed that an initially curved specimen that is flattened and then pulled to failure behaves similarly to bending a flat specimen that is subjected to tensile loads on the micro-level. It was also assumed the moment required to flatten a curved specimen remains constant when the specimen is being pulled. These assumptions may not be valid for specimens with initial curvatures close to the bending failure curvatures, however the tests considered here had comparatively low values, i.e. the failure curvature of the laminate was about 0.17 mm^{-1} whereas the maximum initial curvature used was 0.052 mm^{-1}.

The platen folding setup used for flexural failure does not measure the transverse moment of a specimen subjected to longitudinal bending. Thus the transverse moment was estimated by multiplying the measured curvature values with the ABD matrix obtained from the micro-mechanical model. However, the micro-mechanical model developed in this research targets only the initial linear stiffness of the laminate. Therefore the bending stiffness was modified with a stiffness reduction factor which was estimated by comparing the measured longitudinal moment to the mo-

ment estimated using the ABD matrix. It was then assumed that the reduction in transverse stiffness is similar to that in the longitudinal direction. This stiffness reduction can be explained by laminate thickness being reduced due to the stretching of the tows having the effect of decreasing their waviness. However during failure analysis of tape-spring hinges no stiffness reduction was used since the simulations were based on the initial stiffness specified through the ABD matrix.

The experiments used to measure the shear and twisting strengths do not apply pure shear or twisting due to the effect of the boundary conditions. Therefore the proposed failure locus was used to estimate pure shear and twisting strengths and additional tests were performed for confirming the accuracy of their results. Two or three rail shear fixtures cannot be used with a thin two-ply laminate since it fails in buckling rather than in-plane shear. An option would be to use thin sandwich specimens similar to compression tests (Kueh, 2007).

The failure locus for biaxial bending was obtained by extending the biaxial failure curvature locus developed by Yee (2006) for a similar laminate. This locus confirmed that there is no interaction between the longitudinal and transverse bending moments in the case of pure bending failure. This could be due to the fact that the ratio D_{12}/D_{11} is quite small and hence the two moments have very little influence on each other. However in the case of in-plane loading, even though the ratio A_{12}/A_{11} is small the neutral axes are subjected to stretching and hence in-plane longitudinal and transverse loading affect each other.

Failure by delamination was not considered in developing this failure criterion. It is possible that the two-ply laminate may be subject to delamination, however this was not visible in any of the coupon tests or in any of the tape-spring hinges that were tested.

Simulation of Tape-Spring Hinges

The Abaqus/Explicit finite element solver, which advances the kinematic state of each degree of freedom by direct integration of its equations of motion, was used for simulating tape-spring hinges. Checks to obtain a stable solution and a detailed description of the simulation parameters were presented.

A detailed study of quasi-static folding and deployment of a tape-spring hinge made from a two-ply plain-weave laminate of carbon fibre reinforced plastic was presented. The first stage of this simulation generated the fully folded, strained

configuration of the hinge; this was done by pinching the hinge in the middle to reduce the peak moment required to fold the hinge and then rotating the two ends. The second stage in the simulation was to gradually decrease the relative rotation between the ends until it became zero. A physical model of a particular version of this hinge was constructed and its moment-rotation profile during quasi-static deployment was measured, starting from the fully folded configuration. The simulation of this process has captured both the steady-state moment part of the deployment, during which a localised fold can be seen in each of the tape springs that make up the hinge, as well as the snap back to the straight configuration.

As an alternative to the simulation of the actual folding process, a simulation of a complete folding and deployment cycle without pinching the hinge was carried out. This approach provided an estimate of the maximum moment that could be carried by the hinge during operation. This alternative simulation has shown that for this particular hinge design the deployment moment peak is about half the folding moment peak, a situation typical of deployable structures based on thin shells. The compliance of the testing rig further decreases the deployment moment. From an operational standpoint, the high peak moment for folding indicates that when the hinge is latched it is locked in a highly stable configuration and hence a high pointing accuracy can be expected.

The comparison in Section 10.2 between the measured and predicted moment-rotation relationships during quasi-static deployment of the tape-spring hinge has shown that, although there is good qualitative agreement, there are three main areas of quantitative discrepancy, as follows. The largest discrepancy was in the magnitude of the snap-back moment, overestimated by 63%; also the rotation angle at the hump peak — corresponding to the point of separation of the tape springs — was overestimated by 35% and the deployment moment average was underestimated by 16%. These errors are significantly larger than those obtained when testing the validity of the material model, in Section 8.1, but it should be noted that the focus of Section 8.1 had been on the small-strain behaviour of the material and time-dependent behaviour was not investigated.

It is believed that the main reasons for these discrepancies are the viscoelastic behaviour of the composite material, particularly associated with the matrix, tow misalignment, and deadband effects in the testing machine combined with the inability to measure instantaneous response. The first topic is not well-understood at present as it has only recently started to be addressed in deployable structures (Kwok

and Pellegrino, 2011). The two other issues could be addressed by a more precise manufacturing technique and by the use of a testing rig designed to capture peak values during snapback. Use of the initial stiffness matrix is not an issue here as the peak moment occurs almost at the fully deployed configuration, i.e. the curvatures are almost zero.

The dynamic deployment behaviour of tape-spring hinges was studied by folding a boom with a selected tape-spring hinge design to a specific angle and then suddenly releasing it. The simulations were able to capture both the behaviour of the localised folds and the overall motion of the boom quite accurately. The motion of the boom can be divided into three phases, as follows:

1. deployment phase;
2. incomplete latching and large rotation phase;
3. vibration phase.

Note that Soykasap (2009) and Yee (2006) had observed a similar behaviour in their experimental work on a boom with a three-tape-spring hinge.

It was shown that the symmetric configuration of a tape-spring hinge may be unstable and in this case the fold flips towards one side depending on the particular loading and boundary conditions. The particular hinge design considered had long and narrow tape springs which allowed the fold to travel along the length of the hinge. This provides two different deformation paths which makes the hinge unpredictable.

These predictions were verified with a series of dynamic deployment experiments with a single-point gravity off-load system. The simulations were able to capture the detailed behaviour observed in the experiments. They showed that the deployment phase and vibration phase can be easily predicted but incomplete latching and the large rotation phase is quite sensitive to details of the boundary conditions. Also the second phase is the most critical of the three: if the boom overshoots the fully deployed configuration and hence can interfere with the spacecraft itself or other equipment attached to it.

Design of Tubular Booms

A geometric optimisation study was carried out with a series of parametric studies to improve hinge geometry. The slot geometry was parameterised in terms of slot

length, width and end circle diameter. Failure indices were calculated for the fully folded configuration to confirm that a specific design is safe against failure. An optimisation study was carried out for a hinge that could be folded 180° without breaking, with minimum removal of material from the original tube.

A new design with slot parameters, $L = 90$ mm, $SW = 8$ mm and $D = 15$ mm was obtained, which provides a six times increase in torsional stiffness, twice the axial stiffness, a one third increase in bending stiffness and almost two and a half times the stored energy of the original design. The shorter tape-springs provide better control over the position of the folded region in the hinge and hence the kinematics of deployment are likely to be better constrained.

One of the significant findings of this research is that shorter hinges are obtained if one allows the end cross-sections to deform freely. This means that it is important to understand how the hinge is going to be connected to the spacecraft and to any object that are attached to the tip of the hinge.

These optimised hinges were then considered as candidates for a 1 m long self deployable boom that could be folded around a spacecraft. The hinge design included a failure analysis during both stowage and dynamic deployment. This study has shown that the most critical stages are the fully folded configuration and during deployment the point at which the second hinge latches, affecting the load on the root hinge. High tension and compression loads at the root hinge occur also when the root hinge latches, but it was found that hinges with two tape springs are usually strong enough to withstand this load.

The most critical portion of a hinge is near the transition region between the straight and curved parts of the slot, as shown in Figure 9.12. These regions are subjected to both high bending and some stretching in the mid-plane and hence their strength is governed by an interaction between in-plane and bending. Therefore special care should be given to these regions during the fabrication process.

Overall a 1 m long deployable boom with two tape-spring hinges that can be wrapped around a spacecraft and successfully deployed without any overshoot has being designed and validated. It can be concluded that the simulation techniques developed in this research can be used to design deployable booms with multiple hinges and optimised boom geometry to meet any specific mission requirements.

11.2 Open Issues and Suggested Further Work

Several areas that require further investigation have been identified during this research and are listed below.

Material

- Extend micro-mechanical model to capture the stiffness reduction by redefining for geometrically non-linear behaviour simulation.
- Conduct a thorough investigation of the effect of fibre alignment and arrangement on bending stiffness of two-ply 0/90 laminates.
- Consider alternate laminate designs for tape-spring hinges. A two-ply ± 45 laminate was chosen in this research due to its resistance to crack initiation and propagation near circular parts of slots making tape-spring hinges. However, 0/90 orientation provides the highest bending stiffness and it was observed that 0/90, ± 45 which is an unsymmetric laminate may provide the best compromise between these two laminates. Use of different weave styles and the number of plies should be considered.
- Extend failure criterion to unsymmetric laminates.
- Investigate thermal and viscoelastic effects in the material.

Tape-Spring Hinges

- Improve the quasi-static bending rig to capture high and instantaneous peak moments.
- Investigate the possibility of using experimental methods like digital image correlation to measure stress and strain distribution in tape-spring hinges to compare with simulated values.
- Design a gravity off-load system to test composite booms with several hinges.
- Couple the micro-mechanical finite element model to the tape-spring hinge model to simulate the reduction in bending stiffness.

- Investigate the behaviour of tape-spring hinges made with more than two tape springs.
- Consider the possibility of using hinges with unsymmetric or tapered tape springs to resist back buckling.
- Consider using different hinge designs at the root and elsewhere in the boom to improve the overall deployment behaviour.
- Develop effective connection methods that allow boom cross-sections to ovalise which will reduce the stresses in the tape-spring hinges.

References

Abaqus. *Explicit Version 6.9*. Dassault Systèmes Simulia Crop., Providence, Rhode Island, 2010. 5, 90, 110, 115

D.F. Adams, L.A. Carlsson, and R.B. Pipes. *Experimental Characterization of Advanced Composite Materials*. Third edition, 2003. 44, 50

D.S. Adams and M. Mobrem. Lenticular jointed antenna deployment anomaly and resolution onboard the mars express spacecraft. *Journal of Spacecraft and Rockets*, 46(2):403–410, 2009. 1, 4

Anonymous. Hughes graphite antennas installed on msat-2 craft. Space News, 1994. 1

Autocad. *R15.6*. Autodesk Inc., San Rafael, California, 2002. 38

T. Belytschko, W.K. Liu, and B. Moran. *Nonlinear Finite Elements for Continua and Structures*. 2000. 91, 93

J. Block, M. Straubel, and M. Wiedemann. Ultralight deployable booms for solar sails and other large gossamer structures in space. *Acta Astronautica*, 68(7-8): 984–992, 2011. 3, 14

C. Boesch, C. Pereira, R. John, T. Schmidt, K. Seifart, H. Sparr, J.M. Lautier, and T. Pyttel. Ultra light self-motorized mechanism for deployment of light weight space craft appendages. In *Proceedings of 39th Aerospace Mechanisms Symposium*, Newport, NASA Marshall Space Flight Center, 7-9 May 2008. x, 3, 11, 12

D.O. Brush and B.O. Almroth. *Buckling of Bars, Plates and Shells*. 1975. 108

C.R. Calladine. On the derivation of yield conditions for shells. *J. Appl. Mech.*, 39 (3):852–853, 1972. 82

C.R. Calladine. Love centenary lecture: The theory of thin shell structures. *Proc. Inst. Mech. Eng.*, 202(42):1–9, 1988. 9

F.R. Chiappetta, C.L. Frame, and K.L. Johnson. Hinge element and deployable structures including hinge element. USA Patent 5239793, August 1993. x, 11, 12

T. Chou. *Microstructural Design of Fibre Compoistes*. First edition, 1992. 28

B.N. Cox and G. Flanagan. Handbook of analytical methods for textile composites. Contractor report 4750, National Aeronautics and Space Administration, Hampton, Virginia, 1997. 19, 20

B.N. Cox, W.C. Carter, and N.A. Fleck. A binary model of textile composites: I - formulation. *Acta Metallurgica et Materialia*, 42(10):3463–3479, 1994. 21, 28

ASTM Standard D3039/D3039M-2008. *Standard Test Method for Tensile Properties of Polymer Matrix Composite Materials*. American Society for Testing and Materials, West Conshohocken, Pennsylvania, 2008. 39, 46

ASTM Standard D3518/D3518M-1994. *Standard Test Method for In-Plane Shear Response of Polymer Matrix Composite Materials by Tensile Test of a $\pm 45^\circ$ Laminate*. American Society for Testing and Materials, West Conshohocken, Pennsylvania, 2007. 40

ASTM Standard D6856-2003. *Standard Guide for Testing Fabric-Reinforced "Textile" Composite Materials*. American Society for Testing and Materials, West Conshohocken, Pennsylvania, 2008. 39, 44

ASTM Standard D790M-1986. *Standard Test Method for Flexural Properties of Unreinforced and Reinforced Plastics and Electrical Insulating Materials*. American Society for Testing and Materials, West Conshohocken, Pennsylvania, 1986. 42

M.I. Daniel and O. Ishai. *Engineering Mechanics of Composite Materials*. Second edition, 2006. 21, 26, 59, 60

L.S. Datashvili, H. Baier, and L. Rocha-Schmidt. Multi-scale analysis of structures made of triaxially woven fabric composites with stiff and flexible matrix materials. In *Proceedings of 52nd AIAA/ASME/ASCE/AHS/ASC Structures, Structural Dynamics and Materials Conference*, Denver, Colorado, 4-7 April 2011. 24

A. Endruweit and A.C. Long. A model for the in-plane permeability of triaxially braided reinforcements. *Composites Part A: Applied Science and Manufacturing*, 42(2):165–172, 2011. 24

H. Fang and M. Lou. Tape-spring reinforcements for inflatable structural tubes. NASA Technical Brief NPO-20615, National Aeronautics and Space Administration, 1999. 12

N.A. Fleck and I. Sridhar. End compression of sandwich columns. *Composites: Part A*, 33(3):353–359, 2005. 39, 40, 48

M. Geradin and D. Rixen. *Mechanical Vibrations: Theory and Application to Structural Dynamics*. 1994. 91

R.F. Gibson. *Principles of Composite Material Mechanics*. Second edition, 2007. 21

Z. Hashin and A. Rotem. A fatigue failure criterion for fibre reinforced materials. *Journal of Composite Materials*, 7:448–464, 1973. 27

Hexcel. *Technical Data Sheet HexPly913*. Hexcel Composites. 36, 70

M.J. Hinton, A.S. Kaddour, and P.D. Soden. *Failure Criteria in Fibre-Reinforced-Polymer Composites, The World-Wide Failure Exercise*. First edition, 2004. 28

P.G. Hodge Jr. The rigid-plastic analysis of symmetrically loaded cylindrical shells. *J. Appl. Mech.*, 21:336–442, 1954. 82

T. Ishikawa and T.W. Chou. Elastic behavior of woven hybrid composites. *Journal of Composite Materials*, 16(1):2–19, 1982. 21

T. Ishikawa and T.W. Chou. One-dimensional micromechanical analysis of woven fabric composites. *AIAA Journal*, 21(12):1714–1721, 1983a. 21

T. Ishikawa and T.W. Chou. In-plane thermal expansion and thermal bending coefficients of fabric composites. *Journal of Composite Materials*, 17(2):92–104, 1983b. x, 21, 22

W.G. Jiang, S.R. Hallett, and M.R. Wisnom. Development of domain superposition technique for the modelling of woven fabric composites. In *1st ECCOMAS Thematic Conference on Mechanical Response of Composites*, Oporto, Portugal, 12-14 September 2007. 24

R.M. Jones. *Mechanics of Compostie Materials*. First edition, 1999. 21

J. Jorgensen, E. Louis, J. Hinkle, and M. Silver. Dynamics of an elastically deployable solar array: ground test model validation. In *Proceedings of 46th AIAA/ASME/ASCE/AHS/ASC Structures, Structural Dynamics and Materials Conference*, Austin, Texas, 18-21 April 2005. 2

M. Karahan, Lomov S.V., A.E. Bogdanovich, D Mungalov, and I. Verpoest. Internal geometry evaluation of non-crimp 3d orthogonal woven carbon fabric composite. *Composites Part A*, 41(9):1301–1311, 2010. 24

R.L. Karkkainen and B.V. Sankar. A direct micromechanical approach toward the development of quadratic stress gradient failure criteria for textile composites. *Journal of Composite Materials*, 41(16):1917–1937, 2007. 28, 73, 151

R.L. Karkkainen, B.V. Sankar, and J.T. Tzeng. A direct micromechanics method for analysis of failure initiation of plain weave textile composites. *Composites Part A: Applied Science and Manufacturing*, 66(1):137–150, 2006. 23, 25, 66

P.N. Keller, M.S. Lake, W. Francis, R. Barrett, J. Wintergerst, J. Harvey, E. Ruhl, J. Winter, M.R. Scherbarth, and Murphey T.W. Development of a deployable boom for microsatellites using elastic memory composite material. In *Proceedings of 45th AIAA/ASME/ASCE/AHS/ASC Structures, Structural Dynamics, and Materials Conference*, Palm Springs, California, 19-22 April 2004. 12

A.B.H. Kueh. *Thermo-Mechanical Properties of Triaxial Weave Fabric Composites*. PhD thesis, Department of Engineering, University of Cambridge, 2007. 40, 88, 152

A.B.H. Kueh and S. Pellegrino. Abd matrix of single-ply triaxial weave fabric composites. In *Proceedings of 48th AIAA/ASME/ASCE/AHS/ASC Structures, Structural Dynamics, and Materials Conference*, Honolulu, Hawaii, 23-26 April 2007. 24, 25, 28, 66

K. Kwok and S. Pellegrino. Viscoelastic effects in tape springs. In *Proceedings of 52nd AIAA/ASME/ASCE/AHS/ASC Structures, Structural Dynamics and Materials Conference*, Denver, Colorado, 4-7 April 2011. 153

S.A. Lane, T.W. Murphey, and M. Zatman. Overview of the innovative space-based radar antenna technology program. *Journal of Spacecraft and Rockets*, 48(1): 135–145, 2011. 3

J. Lysmer and R.L. Kuhlemeyer. Fininte dynamic model for infinite media. *Journal of the Engineering Mechanics Division Proceedings of the American Society of Civil Engineers*, 95(4):859–878, 1969. 110

H.M.Y.C. Mallikarachchi and S. Pellegrino. Simulation of quasi-static folding and deployment of ultra- thin composite structures. In *Proceedings of 49th AIAA/ASME/ASCE/AHS/ASC Structures, Structural Dynamics, and Materials Conference*, Schaumburg, Illinois, 07-10 April 2008. 62

H.M.Y.C. Mallikarachchi and S. Pellegrino. Deployment dynamics of composite booms with integral slotted hinges. In *Proceedings of 50th AIAA/ASME/ASCE/AHS/ASC Structures, Structural Dynamics, and Materials Conference*, Palm Springs, California, 4-7 May 2009a. 101

H.M.Y.C. Mallikarachchi and S. Pellegrino. Folding and deployment of ultra-thin composite structures. In *Proceedings of International Scientific Conference on Advanced Lightweight Structures and Reflector Antennas, Institute of Constructions, Special Systems and Engineering Maintenance of the Georgian Technical University*, pages 48–57, Tbilisi, Georgia, 14-16 October 2009b. 114

H.M.Y.C. Mallikarachchi and S. Pellegrino. Optimized designs of composite booms with integral tape-spring hinges. In *Proceedings of 51st AIAA/ASME/ASCE/AHS/ASC Structures, Structural Dynamics, and Materials Conference*, Orlando, Florida, 12-15 April 2010. 114

H.M.Y.C. Mallikarachchi and S. Pellegrino. Design and validation of thin-walled composite deployable booms with tape-spring hinges. In *Proceedings of 52nd AIAA/ASME/ASCE/AHS/ASC Structures, Structural Dynamics, and Materials Conference*, Denver, Colorado, 4-7 April 2011a. 144

H.M.Y.C. Mallikarachchi and S. Pellegrino. Quasi-static folding and deployment of ultrathin composite tape-spring hinges. *Journal of Spacecraft and Rockets*, 48(1): 187–198, 2011b. 131

P.M. Manne and S.W. Tsai. Design optimization of composites plates: Part i - design criteria for strength, stiffness, and manufacturing complexity of composite laminates. *Journal of Composite Materials*, 332(6):544–570, 1998. 73

E.H. Mansfield. Large-deflexion torsion and flexure of initially curved strips. *Proceedings of the Royal Society of London. Series A, Mathematical and Physical Sciences*, 334(1598):279–298, 1973. 9

G. Marks. Flattenable foldable boom hinge. USA Patent 6343442, February 2002. 15, 16

G.W. Marks, M.T. Reilly, and R.L. Huff. The lightweight deployable antenna for the marsis experiment on the mars express spacecraft. In *Proceedings of the 36th Aerospace Mechanisms Symposium*, Glenn Research Center, Cleveland, Ohio, 14-17 May 2002. 15

J. E. Masters and M. A. Portanova. Standard test methods for textile composites. Contractor report 4751, National Aeronautics and Space Administration, Hampton, Virginia, 1996. 39

M.A. McGlockton, B.N. Cox, and R.M. McMeeking. A binary model of textile composites: 3. high failure strain and work of fracture in 3d weaves. *Journal of the Mechanics and Physics of Solids*, 51(8):1573–1600, 2003. 23

M. Mobrem and D.S. Adams. Deployment analysis of lenticular jointed antennas onboard the mars express spacecraft. *Journal of Spacecraft and Rockets*, 46(2): 394–402, 2009. 4, 16

N.K. Naik and V.K. Ganesh. Prediction of on-axes elastic properties of plain weave fabric composites. *Composites Science and Technology*, 45(2):135–152, 1992. 23

N.K. Naik and V.K. Ganesh. An analytical method for plain weave fabric composites. *Composites*, 26(4):281–289, 1995. 23

S.T. Pinho, L. Iannucci, and P. Robinson. Physically based failure models and criteria for laminated fibre-reinforced composites with emphasis on fibre kinking. part ii: Fe implementation. *Composites Part A-Applied Science and Manufacturing*, 37(5):766–777, 2006. 70

S.C. Quek, A. Waas, K.W. Shahwan, and V. Agaram. Analysis of 2d triaxial flat braided textile composites. *International Journal of Mechanical Sciences*, 45(7): 1077–1096, 2003. 60, 150

S.C. Quek, A. Waas, K.W. Shahwan, and V. Agaram. Compressive response and failure of braided textile composites: Part 2 - computations. *International Journal of Non-linear Mechanics*, 39(4):649–663, 2004. 28

F.P.J. Rimrott and G. Fritsche. Fundamentals of stem mechanics. In S. Pellegrino and S.D. Guest, editors, *IUTAM-IASS Symposium on Deployable Structures: Theory and Applications (Cambridge, UK, 6-9 September 1998)*, pages 321–333, Dordrecht, The Netherlands, 2000. Kluwer Academic Publishers. 13

C.P. Rubin. Deployable boom. USA Patent 3434254, March 1969. 13

G. Sanford, A. Biskner, and T.W. Murphey. Large strain behavior of thin unidirectional composite flexures. In *Proceedings of 51st AIAA/ASME/ASCE/AHS/ASC Structures, Structural Dynamics, and Materials Conference*, Orlando, Florida, 12-15 April 2010. 42, 53

A. Sawczuk and P.G. Hodge Jr. Comparison of yield conditions for circular cylindrical shells. *Journal of the Franklin Institute*, 269(5):362–374, 1960. 82

K.A. Seffen. On the behavior of folded tape-springs. *Journal of Applied Mechanics-Transactions of the ASME*, 68(3):369–375, 2001. 12

K.A. Seffen and S. Pellegrino. Deployment dynamics of tape springs. *Proceedings of the Royal Society of London Series A*, 455(1983):1003–1048, 1999. 9, 10, 90, 108, 131

P. Seizt. Spar resolving spat over antenna work. Space News, 29 August - 4 September 1994. 1

C. Sickinger, L. Herbeck, T. Strohelin, and J. Torrez-Torres. Lightweight deployable booms: Design, manufacture, verification, and smart materials application. In *Proceedings of 55th International Astronautical Congress, IAF/IAA/IISL*, Vancouver, Canada, 04-08 October 2004. 3

M. J. Silver, J.D. Hinkle, and L.D. Peterson. Contolled displacement snap-trough of tape springs: Modelling and experiment. In *Proceedings of 46th*

AIAA/ASME/ASCE/AHS/ASC Structures, Structural Dynamics, and Materials Conference, Austin, Texas, 18-21 April 2005. 17

M.J. Silver and P. Warren. Dynamic modeling of the folding of multi-shell flexible composites. In *Proceedings of 51st AIAA/ASME/ASCE/AHS/ASC Structures, Structural Dynamics, and Materials Conference*, Orlando, Florida, 12-15 April 2010. 12

M.J. Silver, J.D. Hinkle, and L.D. Peterson. Modeling of snap-back bending response of doubly slit cylindrical shells. In *Proceedings of 45th AIAA/ASME/ASCE/AHS/ASC Structures, Structural Dynamics, and Materials Conference*, Palm Springs, California, 19-22 April 2004. 17

0. Soykasap, A. Watt, and S. Pellegrino. New deployable reflector concept. In *Proceedings of 45th AIAA/ASME/ASCE/AHS/ASC Structures, Structural Dynamics and Materials Conference*, Palm Springs, California, 19-22 April 2004. 2, 3, 14, 15

O. Soykasap. Micromechanical models for bending behaviour of woven composites. *Journal of Spacecraft and Rockets*, 43(5):1093–1100, 2006. 5, 21, 53, 59, 63, 150

O. Soykasap. Deployment analysis of a self-deployable composite boom. *Composite Structures*, 89(3):374–381, 2009. 4, 17, 154

O. Soykasap, S. Pellegrino, P. Howard, and M. Notter. Folding large antenna tape spring. *Journal of Spacecraft and Rockets*, 45(3):560–567, 2008. 2, 3, 14

W. Szyszkowski, K. Fielden, and D.W. Johnson. Self-locking satellite boom with flexure-mode joints. *Applied Mechanics Reviews*, 50(11S):225–231, 1997. 9

X. Tang and J.D. Whitcomb. General techniques for exploiting periodicity and symmetries in micromechanics analysis of textile composites. *Journal of Composite Materials*, 37(13):1167–1189, 2003. 23

Torayca. *Technical Data Sheet No. CFA-001, T300 Data Sheet*. Toray Industries, Inc. 36, 69

S.W. Tsai and H.T. Hahn. *Introduction to Composite Materials*. First edition, 1980. 21

S.W. Tsai and E.M. Wu. A general theory of strength for anisotropic materials. *Journal of Composite Materials*, 5(1):58–80, 1971. 26, 74

A.M.A. van der Heijden. *Koiter's Elastic Stability of Solids and Structures*. 2009. 108

W.W. Vyvyan. Self-actuating, self-locking hinge. USA Patent 3386128, June 1968. x, 9, 11

P.A. Warren. Foldable member. USA Patent 6,374,565 B1, 2002. 1, 15

P.A. Warren, B.J. Dobson, J.D. Hinkle, and M. Silver. Experimental characterization of lightweight strain energy deployment hinges. In *Proceedings of 46th AIAA/ASME/ASCE/AHS/ASC Structures, Structural Dynamics and Materials Conference*, Austin, Texas, 18-21 April 2005. 12, 108

A.M. Watt. *Deployable Structures with Self-Locking Hinges*. PhD thesis, Department of Engineering, University of Cambridge, 2003. 9, 13

J. Whitcomb and K. Srirengan. Effect of various approximations on predicted progressive failure in plain weave composites. *Composite Structures*, 34(1):13–20, 1996. 28, 63

J.D. Whitcomb, C.D. Chapman, and X. Tang. Derivation of boundary conditions for micromechanics analyses of plain and satin weave composites. *Journal of Composite Materials*, 34(9):724–747, 2000. 23

J. Xu, B.N. Cox, M.A. McGlockton, and W.C. Carter. A binary model of textile composites 2. the elastic regime. *Acta Metallurgica Et Materialia*, 43(9):3511–3524, 1995. 23

Q.D. Yang, K.L. Rugg, B.N. Cox, and D.B. Marshall. Evaluation of macroscopic and local strains in a three-dimensional woven c/sic composite. *Journal of the American Ceramic Society*, 88(3):719–725, 2005. 69

J.C.H. Yee. *Thin CFRP Composite Deployable Structures*. PhD thesis, Department of Engineering, University of Cambridge, 2006. 17, 18, 37, 40, 45, 77, 80, 88, 110, 152, 154

J.C.H. Yee and S. Pellegrino. Composite tube hinges. *Journal of Aerospace Engineering*, 18(4):224–231, 2005a. 4, 9, 90

J.C.H. Yee and S. Pellegrino. Folding of woven composite structures. *Composites Part A-Applied Science and Manufacturing*, 36(2):273–278, 2005b. 5

Appendix A

Abaqus Input Files

A.1 Quasi-Static Folding Tape-Spring Hinge

```
*HEADING
** Job name: Static-Folding Model name: Exp-Tape-Spring-Hinge
*Preprint, echo=NO, model=NO, history=NO, contact=NO
** ======================================
** Parts
** ======================================
*PART, name=Hinge
*NODE
... ... ...
*ELEMENT, type=S4, elset = eleHinge
... ... ...
**-------------------------------------
**  Defining ABD stiffness matrix and orientation
**-------------------------------------
*ORIENTATION, name=Ori-1, system=CYLINDRICAL
 0.,  0., 0., 0., 0., 1.
 1, 0.
** Material properties from micro-mechanical model **
*SHELL GENERAL SECTION, elset=eleHinge, density=3.18E-10, orientation=Ori1
7714,6380,7714,0,0,5962,0,0
0,23.6,0,0,0,17.9,23.6,0
0,0,0,0,16.7
**
*END PART
... ... ...
```

```
... ... ...
** ======================================
** Assembly
** ======================================
*ASSEMBLY, name=Assembly
**
*INSTANCE, name=Hinge-1, part=Hinge
... ... ...
*END INSTANCE
... ... ...
... ... ...
**--------------------------------------
** String-plate connection
**--------------------------------------
*ELEMENT, type=CONN3D2
1, String.2, Punch-Bot.2
2, Punch-Top.2, String.1
*CONNECTOR SECTION, elset=setWires
Weld,
...
**--------------------------------------
** Defining node and element sets
**--------------------------------------
*NSET, nset=setString, instance=String
 1, 2
*ELSET, elset=setString, instance=String
 1,
... ... ...
... ... ...
**--------------------------------------
** Surface definitions
**--------------------------------------
*ELSET, elset=surfHinge, internal, instance=Hinge-1, generate
    1,  2412,     1
*SURFACE, type=ELEMENT, name=surfHinge
 surfHinge,
... ... ...
... ... ...
**--------------------------------------
** Constraint: Equation for pure bending
**--------------------------------------
*EQUATION
3
```

```
Ref-Fixed, 4,  1.
Ref-Free,  4, -1.
Ref-Dummy, 4, -1.
**
*END ASSEMBLY
** =====================================
** Amplitude definitions
**-------------------------------------
*AMPLITUDE, name=ampPinching, time=TOTAL TIME, definition=SMOOTH STEP
0., 0., 0.2, 1.
... ...
... ...
**-------------------------------------
** Materials
**-------------------------------------
*MATERIAL, name=Aluminium
*Density
 2.7e-09,
*Elastic
70000., 0.35
... ... ...
... ... ...
**-------------------------------------
** Interaction properties
**-------------------------------------
*SURFACE INTERACTION, name=Fric-less
*Friction
0.,
**-------------------------------------
** Predefined fields
**-------------------------------------
*INITIAL CONDITIONS, type=TEMPERATURE
setString, 0.
** =====================================
** Step
** =====================================
*STEP, name=Folding1-Pinching
*DYNAMIC, Explicit, scale factor=0.8
, 0.2
*Bulk Viscosity
0.0, 0.
** Mass Scaling: Semi-Automatic Whole Model
*FIXED MASS SCALING, Type=Below Min, dt=1e-6
```

```
**--------------------------------------
** Boundary conditions: folding
**--------------------------------------
*BOUNDARY, amplitude=ampFolding
Ref-Dummy, 1, 3
Ref-Dummy, 4, 4, 3.
Ref-Dummy, 5, 6
... ... ...
... ... ...
**--------------------------------------
** Loads: Viscous pressure
**--------------------------------------
*DSLOAD, amplitude=ampViscous
surfHinge, vp, 146.28e-8
**--------------------------------------
** Thermal contraction of the string
**--------------------------------------
*TEMPERATURE, amplitude=ampPinching
setString, -100.
**--------------------------------------
** Interaction: General-Contact
**--------------------------------------
*CONTACT, op=NEW
*Contact Inclusions, ALL EXTERIOR
*Contact Exclusions
String.Surf-String, Surf-all-except-string
*Contact property assignment
 ,  , Fric-less
**--------------------------------------
** Output requests
**--------------------------------------
*RESTART, write, number interval=1, time marks=NO
*OUTPUT, field, time interval=0.01
*Node Output
A, U, V
*Element Output, directions=YES
SE, SF
*Contact Output
CSTRESS,
... ... ...
... ... ...
*OUTPUT, history, filter=ANTIALIASING, time interval=0.01
*Energy Output, elset=All-except-hinge
```

```
ALLAE, ALLFD, ALLIE, ALLKE, ALLSE, ALLVD, ALLWK, ETOTAL
... ... ...
... ... ...
END STEP
** ======================================
... ... ...
```

A.2 Dynamic Deployment Tape-Spring Hinge

```
*HEADING
** Job name: Dynamic_deployment Model name: Exp-Tape-Spring-Hinge
*Preprint, echo=NO, model=NO, history=NO, contact=NO
** ======================================
... ... ...
... ... ...
... ... ...
** ======================================
** Step3
** ======================================
*STEP, name=Dyanamic_deployment
*DYNAMIC, Explicit, scale factor=0.8
, 1.0
*Bulk Viscosity
0.1, 0.
** Mass Scaling
*FIXED MASS SCALING, factor=1.
**--------------------------------------
** Boundary conditions: fixed end
**--------------------------------------
*BOUNDARY, op=NEW
Fixed_end, 1, 6
**--------------------------------------
** Loads: Viscous pressure
**--------------------------------------
*DSLOAD, op=NEW, amplitude=ampViscous
surfTape, vp, 146.28e-9
**
**--------------------------------------
** Interaction: General-Contact
**--------------------------------------
*CONTACT, op=NEW
*Contact Inclusions, ALL EXTERIOR
```

```
*Contact property assignment
 ,  , Fric-less
**--------------------------------------
** Output requests
**--------------------------------------
*RESTART, write, number interval=1, time marks=NO
*OUTPUT, field, time interval=0.001
*Node Output
A, U, V
*Element Output, directions=YES
SE, SF
*Contact Output
CSTRESS,
... ... ...
... ... ...
*OUTPUT, history, filter=ANTIALIASING, time interval=0.001
*Energy Output, elset=All-except-hinge
ALLAE, ALLFD, ALLIE, ALLKE, ALLSE, ALLVD, ALLWK, ETOTAL
... ... ...
... ... ...
END STEP
** ======================================
... ... ...
```

A.3 Micro-Mechanical Model

```
*HEADING
** Job name: Mid-plane strainX Model name: Unitcell_1
*Preprint, echo=NO, model=NO, history=NO, contact=NO
** ======================================
*NODE, nset=Ref_P
100001, 0, 0, 0
100002, 6.660000e-002, 0, 0
... ...
... ...
... ...
*NODE, nset=dum_StrainMX
160001,0,0,0
160002,0,0,0
... ...
... ...
**--------------------------------------
```

```
**              Orientation
**--------------------------------------
*ORIENTATION, name=Ori_PR
    0., 1., 0., 1., 0., 0.
1, 0.
*ORIENTATION, name=Ori_QS
    1., 0., 0., 0., 1., 0.
1, 0.
** Tows
*SOLID SECTION, elset=Tow_PR1_Bot, orientation=Ori_PR, Material=T300-1K/913
1.,
... ...
... ...
** Matrix
*SOLID SECTION, elset=Matrix1, orientation=Ori_PR, Material=Hexcel-913
1.,
... ...
... ...
**--------------------------------------
** Multi-point constraints
**--------------------------------------
*MPC
Tie,1641,21
*MPC
Tie,2061,441
... ...
... ...
**--------------------------------------
** Connector elements - rigid beams
**--------------------------------------
*ELEMENT, type=CONN3D2, Elset=ConBeams4
500017,8157,4898
500018,4898,100002
500019,100002,3281
... ...
... ...
*CONNECTOR SECTION, elset=ConBeams4
Beam
**--------------------------------------
** Periodic boundary conditions
**--------------------------------------
*EQUATION
3
```

```
100001, 1, -1.
100041, 1,  1.
150001, 1, -2.664
*EQUATION
3
100001, 2, -1.
100041, 2,  1.
150001, 2, -2.664
*EQUATION
3
100001, 3, -1.
100041, 3,  1.
150001, 3,  0.
*EQUATION
3
100001, 4, -1.
100041, 4,  1.
150001, 4,  2.664
*EQUATION
3
100001, 5, -1.
100041, 5,  1.
150001, 5, -2.664
*EQUATION
3
100001, 6, -1.
100041, 6,  1.
150001, 6,  0.
... ...
... ...
**--------------------------------------
** Material properties
**--------------------------------------
**
*MATERIAL, name=T300-1K/913
*Elastic, type=ENGINEERING CONSTANTS
174450., 13220., 13220., 0.2536, 0.2536,  0.454,  4113.,  4113.
4546.,
*Material, name=Hexcel-913
*Elastic
3390., 0.41
** ======================================
** Step
```

```
** ======================================
*STEP, name=Step-1, nlgeom=NO
*STATIC
1., 1., 1e-05, 1.
**--------------------------------------
** Boundary conditions
**--------------------------------------
** Name: Strains solid periodic x-direction
*BOUNDARY
dum_StrainMX, 1, 1, 1.
dum_StrainMX, 2, 6
** Name: Strains solid periodic y-direction
*BOUNDARY
dum_StrainMY, 1, 6
**--------------------------------------
**Output request
**--------------------------------------
*RESTART, write, frequency=0
**
*OUTPUT, field, variable=PRESELECT
*Element Output, Elset=eleTow
EVOL,
*Element Output, Elset=eleMatrix
EVOL,
**
*OUTPUT, history, variable=PRESELECT
*NODE PRINT, Nset=dum_StrainMX, Summary=No, freq=1
RF
*NODE PRINT, Nset=dum_StrainMY, Summary=No, freq=1
RF
*NODE PRINT, Nset=Ref_P, Summary=No, freq=1
U
*NODE PRINT, Nset=Ref_Q, Summary=No, freq=1
U
*NODE PRINT, Nset=Ref_R, Summary=No, freq=1
U
*NODE PRINT, Nset=Ref_S, Summary=No, freq=1
U
*END STEP
** ======================================
```

Appendix B

ABD Matrices

Beam Model

$[0/90]_2$ fibre in-phase

$$\begin{Bmatrix} N_x \\ N_y \\ N_{xy} \\ -- \\ M_x \\ M_y \\ M_{xy} \end{Bmatrix} = \left(\begin{array}{ccc|ccc} 9102 & 2877 & 0 & 0 & 0 & 0 \\ 2877 & 9102 & 0 & 0 & 0 & 0 \\ 0 & 0 & 112 & 0 & 0 & 0 \\ \hline 0 & 0 & 0 & 45.4 & 0 & 0 \\ 0 & 0 & 0 & 0 & 45.4 & 0 \\ 0 & 0 & 0 & 0 & 0 & 0.6 \end{array}\right) \begin{Bmatrix} \epsilon_x \\ \epsilon_y \\ \epsilon_{xy} \\ -- \\ \kappa_x \\ \kappa_y \\ \kappa_{xy} \end{Bmatrix} \tag{B.1}$$

$[0/90]_2$ fibre out-of-phase

$$\begin{Bmatrix} N_x \\ N_y \\ N_{xy} \\ -- \\ M_x \\ M_y \\ M_{xy} \end{Bmatrix} = \left(\begin{array}{ccc|ccc} 11995 & 0 & 0 & 0 & 0 & 0 \\ 0 & 11995 & 0 & 0 & 0 & 0 \\ 0 & 0 & 114 & 0 & 0 & 0 \\ \hline 0 & 0 & 0 & 34.4 & 10.7 & 0 \\ 0 & 0 & 0 & 10.7 & 34.4 & 0 \\ 0 & 0 & 0 & 0 & 0 & 0.95 \end{array}\right) \begin{Bmatrix} \epsilon_x \\ \epsilon_y \\ \epsilon_{xy} \\ -- \\ \kappa_x \\ \kappa_y \\ \kappa_{xy} \end{Bmatrix} \tag{B.2}$$

$[\pm\ 45]_2$ fibre in-phase

$$\begin{Bmatrix} N_x \\ N_y \\ N_{xy} \\ -- \\ M_x \\ M_y \\ M_{xy} \end{Bmatrix} = \left(\begin{array}{ccc|ccc} 6102 & 5878 & 0 & 0 & 0 & 0 \\ 5878 & 6102 & 0 & 0 & 0 & 0 \\ 0 & 0 & 3113 & 0 & 0 & 0 \\ \hline 0 & 0 & 0 & 23.3 & 22.1 & 0 \\ 0 & 0 & 0 & 22.1 & 23.3 & 0 \\ 0 & 0 & 0 & 0 & 0 & 22.7 \end{array}\right) \begin{Bmatrix} \epsilon_x \\ \epsilon_y \\ \epsilon_{xy} \\ -- \\ \kappa_x \\ \kappa_y \\ \kappa_{xy} \end{Bmatrix} \tag{B.3}$$

$[\pm\ 45]_2$ fibre out-of-phase)

$$\begin{Bmatrix} N_x \\ N_y \\ N_{xy} \\ -- \\ M_x \\ M_y \\ M_{xy} \end{Bmatrix} = \left(\begin{array}{ccc|ccc} 6110 & 5883 & 0 & 0 & 0 & 0 \\ 5883 & 6110 & 0 & 0 & 0 & 0 \\ 0 & 0 & 5996 & 0 & 0 & 0 \\ \hline 0 & 0 & 0 & 23.5 & 21.6 & 0 \\ 0 & 0 & 0 & 21.6 & 23.5 & 0 \\ 0 & 0 & 0 & 0 & 0 & 11.9 \end{array}\right) \begin{Bmatrix} \epsilon_x \\ \epsilon_y \\ \epsilon_{xy} \\ -- \\ \kappa_x \\ \kappa_y \\ \kappa_{xy} \end{Bmatrix} \tag{B.4}$$

Solid Model (rectangular cross-section)

$[0/90]_2$ fibre in-phase

$$\begin{Bmatrix} N_x \\ N_y \\ N_{xy} \\ -- \\ M_x \\ M_y \\ M_{xy} \end{Bmatrix} = \left(\begin{array}{ccc|ccc} 8639 & 1814 & 0 & 0 & 0 & 0 \\ 1814 & 8639 & 0 & 0 & 0 & 0 \\ 0 & 0 & 359 & 0 & 0 & 0 \\ \hline 0 & 0 & 0 & 43 & 9 & 0 \\ 0 & 0 & 0 & 9 & 43 & 0 \\ 0 & 0 & 0 & 0 & 0 & 2.5 \end{array}\right) \begin{Bmatrix} \epsilon_x \\ \epsilon_y \\ \epsilon_{xy} \\ -- \\ \kappa_x \\ \kappa_y \\ \kappa_{xy} \end{Bmatrix} \tag{B.5}$$

$[0/90]_2$ fibre out-of-phase

$$\begin{Bmatrix} N_x \\ N_y \\ N_{xy} \\ -- \\ M_x \\ M_y \\ M_{xy} \end{Bmatrix} = \left(\begin{array}{ccc|ccc} 11147 & 270 & 0 & 0 & 0 & 0 \\ 270 & 11147 & 0 & 0 & 0 & 0 \\ 0 & 0 & 356 & 0 & 0 & 0 \\ \hline 0 & 0 & 0 & 33.0 & 8.0 & 0 \\ 0 & 0 & 0 & 8.0 & 33.0 & 0 \\ 0 & 0 & 0 & 0 & 0 & 3.0 \end{array}\right) \begin{Bmatrix} \epsilon_x \\ \epsilon_y \\ \epsilon_{xy} \\ -- \\ \kappa_x \\ \kappa_y \\ \kappa_{xy} \end{Bmatrix} \tag{B.6}$$

$[\pm 45]_2$ fibre in-phase

$$\begin{Bmatrix} N_x \\ N_y \\ N_{xy} \\ -- \\ M_x \\ M_y \\ M_{xy} \end{Bmatrix} = \left(\begin{array}{ccc|ccc} 5585 & 4868 & 0 & 0 & 0 & 0 \\ 4868 & 5585 & 0 & 0 & 0 & 0 \\ 0 & 0 & 3413 & 0 & 0 & 0 \\ \hline 0 & 0 & 0 & 24.4 & 19.4 & 0 \\ 0 & 0 & 0 & 19.4 & 24.4 & 0 \\ 0 & 0 & 0 & 0 & 0 & 21.1 \end{array}\right) \begin{Bmatrix} \epsilon_x \\ \epsilon_y \\ \epsilon_{xy} \\ -- \\ \kappa_x \\ \kappa_y \\ \kappa_{xy} \end{Bmatrix} \tag{B.7}$$

$[\pm\ 45]_2$ fibre out-of-phase

$$\begin{Bmatrix} N_x \\ N_y \\ N_{xy} \\ -- \\ M_x \\ M_y \\ M_{xy} \end{Bmatrix} = \left(\begin{array}{ccc|ccc} 6065 & 5352 & 0 & 0 & 0 & 0 \\ 5352 & 6065 & 0 & 0 & 0 & 0 \\ 0 & 0 & 5439 & 0 & 0 & 0 \\ \hline 0 & 0 & 0 & 23 & 18 & 0 \\ 0 & 0 & 0 & 18 & 23 & 0 \\ 0 & 0 & 0 & 0 & 0 & 12.3 \end{array}\right) \begin{Bmatrix} \epsilon_x \\ \epsilon_y \\ \epsilon_{xy} \\ -- \\ \kappa_x \\ \kappa_y \\ \kappa_{xy} \end{Bmatrix} \tag{B.8}$$

Solid Model (sine wave cross-section)

$[0/90]_2$ fibre in-phase

$$\begin{Bmatrix} N_x \\ N_y \\ N_{xy} \\ -- \\ M_x \\ M_y \\ M_{xy} \end{Bmatrix} = \left(\begin{array}{ccc|ccc} 11712 & 984 & 0 & 0 & 0 & 0 \\ 984 & 11712 & 0 & 0 & 0 & 0 \\ 0 & 0 & 563 & 0 & 0 & 0 \\ \hline 0 & 0 & 0 & 45.0 & 1.7 & 0 \\ 0 & 0 & 0 & 1.7 & 45.0 & 0 \\ 0 & 0 & 0 & 0 & 0 & 2.4 \end{array}\right) \begin{Bmatrix} \epsilon_x \\ \epsilon_y \\ \epsilon_{xy} \\ -- \\ \kappa_x \\ \kappa_y \\ \kappa_{xy} \end{Bmatrix} \tag{B.9}$$

$[0/90]_2$ fibre out-of-phase

$$\begin{Bmatrix} N_x \\ N_y \\ N_{xy} \\ -- \\ M_x \\ M_y \\ M_{xy} \end{Bmatrix} = \left(\begin{array}{ccc|ccc} 12133 & 544 & 0 & 0 & 0 & 0 \\ 544 & 12133 & 0 & 0 & 0 & 0 \\ 0 & 0 & 569 & 0 & 0 & 0 \\ \hline 0 & 0 & 0 & 41.5 & 5.5 & 0 \\ 0 & 0 & 0 & 5.5 & 41.5 & 0 \\ 0 & 0 & 0 & 0 & 0 & 2.4 \end{array}\right) \begin{Bmatrix} \epsilon_x \\ \epsilon_y \\ \epsilon_{xy} \\ -- \\ \kappa_x \\ \kappa_y \\ \kappa_{xy} \end{Bmatrix} \tag{B.10}$$

$[\pm 45]_2$ fibre in-phase

$$\left\{\begin{array}{c} N_x \\ N_y \\ N_{xy} \\ -- \\ M_x \\ M_y \\ M_{xy} \end{array}\right\} = \left(\begin{array}{ccc|ccc} 6917 & 5779 & 0 & 0 & 0 & 0 \\ 5779 & 6917 & 0 & 0 & 0 & 0 \\ 0 & 0 & 5364 & 0 & 0 & 0 \\ \hline\hline 0 & 0 & 0 & 25.7 & 21.0 & 0 \\ 0 & 0 & 0 & 21.0 & 25.7 & 0 \\ 0 & 0 & 0 & 0 & 0 & 21.6 \end{array}\right) \left\{\begin{array}{c} \epsilon_x \\ \epsilon_y \\ \epsilon_{xy} \\ -- \\ \kappa_x \\ \kappa_y \\ \kappa_{xy} \end{array}\right\} \tag{B.11}$$

$[\pm 45]_2$ fibre out-of-phase

$$\left\{\begin{array}{c} N_x \\ N_y \\ N_{xy} \\ -- \\ M_x \\ M_y \\ M_{xy} \end{array}\right\} = \left(\begin{array}{ccc|ccc} 6907 & 5770 & 0 & 0 & 0 & 0 \\ 5770 & 6907 & 0 & 0 & 0 & 0 \\ 0 & 0 & 5794 & 0 & 0 & 0 \\ \hline\hline 0 & 0 & 0 & 25.9 & 21.1 & 0 \\ 0 & 0 & 0 & 21.1 & 25.9 & 0 \\ 0 & 0 & 0 & 0 & 0 & 18.0 \end{array}\right) \left\{\begin{array}{c} \epsilon_x \\ \epsilon_y \\ \epsilon_{xy} \\ -- \\ \kappa_x \\ \kappa_y \\ \kappa_{xy} \end{array}\right\} \tag{B.12}$$

Solid Model (square root of sine wave cross-section)

$[0/90]_2$ fibre in-phase

$$\left\{\begin{array}{c} N_x \\ N_y \\ N_{xy} \\ -- \\ M_x \\ M_y \\ M_{xy} \end{array}\right\} = \left(\begin{array}{ccc|ccc} 12999 & 1104 & 0 & 0 & 0 & 0 \\ 1104 & 12999 & 0 & 0 & 0 & 0 \\ 0 & 0 & 653 & 0 & 0 & 0 \\ \hline\hline 0 & 0 & 0 & 47.5 & 1.8 & 0 \\ 0 & 0 & 0 & 1.8 & 47.5 & 0 \\ 0 & 0 & 0 & 0 & 0 & 2.6 \end{array}\right) \left\{\begin{array}{c} \epsilon_x \\ \epsilon_y \\ \epsilon_{xy} \\ -- \\ \kappa_x \\ \kappa_y \\ \kappa_{xy} \end{array}\right\} \tag{B.13}$$

$[\pm 45]_2$ fibre in-phase

$$\left\{\begin{array}{c} N_x \\ N_y \\ N_{xy} \\ -- \\ M_x \\ M_y \\ M_{xy} \end{array}\right\} = \left(\begin{array}{ccc|ccc} 7704 & 6399 & 0 & 0 & 0 & 0 \\ 6399 & 7704 & 0 & 0 & 0 & 0 \\ 0 & 0 & 5947 & 0 & 0 & 0 \\ \hline\hline 0 & 0 & 0 & 27.2 & 22.0 & 0 \\ 0 & 0 & 0 & 22.0 & 27.2 & 0 \\ 0 & 0 & 0 & 0 & 0 & 22.9 \end{array}\right) \left\{\begin{array}{c} \epsilon_x \\ \epsilon_y \\ \epsilon_{xy} \\ -- \\ \kappa_x \\ \kappa_y \\ \kappa_{xy} \end{array}\right\} \tag{B.14}$$

Solid Model (fourth root of sine wave cross-section)

$[0/90]_2$ fibre in-phase

$$\begin{Bmatrix} N_x \\ N_y \\ N_{xy} \\ -- \\ M_x \\ M_y \\ M_{xy} \end{Bmatrix} = \left(\begin{array}{ccc|ccc} 13009 & 1085 & 0 & 0 & 0 & 0 \\ 1085 & 13009 & 0 & 0 & 0 & 0 \\ 0 & 0 & 667 & 0 & 0 & 0 \\ -- & -- & -- & -- & -- & -- \\ 0 & 0 & 0 & 41.3 & 1.5 & 0 \\ 0 & 0 & 0 & 1.5 & 41.3 & 0 \\ 0 & 0 & 0 & 0 & 0 & 2.3 \end{array}\right) \begin{Bmatrix} \epsilon_x \\ \epsilon_y \\ \epsilon_{xy} \\ -- \\ \kappa_x \\ \kappa_y \\ \kappa_{xy} \end{Bmatrix} \quad \text{(B.15)}$$

$[0/90]_2$ fibre out-of-phase

$$\begin{Bmatrix} N_x \\ N_y \\ N_{xy} \\ -- \\ M_x \\ M_y \\ M_{xy} \end{Bmatrix} = \left(\begin{array}{ccc|ccc} 13667 & 571 & 0 & 0 & 0 & 0 \\ 571 & 13667 & 0 & 0 & 0 & 0 \\ 0 & 0 & 667 & 0 & 0 & 0 \\ -- & -- & -- & -- & -- & -- \\ 0 & 0 & 0 & 36.8 & 3.5 & 0 \\ 0 & 0 & 0 & 3.5 & 36.8 & 0 \\ 0 & 0 & 0 & 0 & 0 & 2.3 \end{array}\right) \begin{Bmatrix} \epsilon_x \\ \epsilon_y \\ \epsilon_{xy} \\ -- \\ \kappa_x \\ \kappa_y \\ \kappa_{xy} \end{Bmatrix} \quad \text{(B.16)}$$

$[\pm 45]_2$ fibre in-phase

$$\begin{Bmatrix} N_x \\ N_y \\ N_{xy} \\ -- \\ M_x \\ M_y \\ M_{xy} \end{Bmatrix} = \left(\begin{array}{ccc|ccc} 7714 & 6380 & 0 & 0 & 0 & 0 \\ 6380 & 7714 & 0 & 0 & 0 & 0 \\ 0 & 0 & 5962 & 0 & 0 & 0 \\ -- & -- & -- & -- & -- & -- \\ 0 & 0 & 0 & 23.6 & 19.1 & 0 \\ 0 & 0 & 0 & 19.1 & 23.6 & 0 \\ 0 & 0 & 0 & 0 & 0 & 19.9 \end{array}\right) \begin{Bmatrix} \epsilon_x \\ \epsilon_y \\ \epsilon_{xy} \\ -- \\ \kappa_x \\ \kappa_y \\ \kappa_{xy} \end{Bmatrix} \quad \text{(B.17)}$$

$[\pm 45]_2$ fibre out-of-phase

$$\begin{Bmatrix} N_x \\ N_y \\ N_{xy} \\ -- \\ M_x \\ M_y \\ M_{xy} \end{Bmatrix} = \left(\begin{array}{ccc|ccc} 7786 & 6453 & 0 & 0 & 0 & 0 \\ 6453 & 7786 & 0 & 0 & 0 & 0 \\ 0 & 0 & 6548 & 0 & 0 & 0 \\ -- & -- & -- & -- & -- & -- \\ 0 & 0 & 0 & 22.4 & 17.9 & 0 \\ 0 & 0 & 0 & 17.9 & 22.4 & 0 \\ 0 & 0 & 0 & 0 & 0 & 16.7 \end{array}\right) \begin{Bmatrix} \epsilon_x \\ \epsilon_y \\ \epsilon_{xy} \\ -- \\ \kappa_x \\ \kappa_y \\ \kappa_{xy} \end{Bmatrix} \quad \text{(B.18)}$$